Optimization and Development of Sodium-based Electrolytes for Energy Storage Devices

A Dissertation Presented for the

Doctor of Philosophy

Degree

The University of Tennessee, Knoxville

Jameson Landon Tyler

May 2022

DEDICATION

I dedicate this work to my parents, Danielle Mears and Martin Tyler.

ACKNOWLEDGEMENTS

I want to acknowledge the love and support that my family has given me in no specific order: Danielle Mears, Martin Tyler, Edward Mears, Sharon Stephens, Vivian Dotson, Jimmy Dotson, Braylan Tyler, Pam Tyler, and the rest of my wonderful family. Through all the trials and hardships, all of you have always had faith in me in this journey. I would also like to acknowledge the friends who have become family over the course of these last five years and without them much of this wouldn't have been possible: Cody Cravens, Austin Powers, Bailey Lane, Brandon Cravens, Alex Otten, Katie Browning, Teerth Brahmbhatt, Claire Seitzinger, Robert Looney, Dustin Mettler, Katie Bennet, Spencer Flottman and so many more.

I would also like to acknowledge the teaching and guidance of colleagues who helped me struggle through the learning process of what it takes to become a scientist: Frank Delnick, Robert Sacci, Ethan Self, Gabriel Veith, Thomas Malkowski, Rebecca McAuliffe, Beth Armstrong, Thomas Zawodzinski, and Rose Ruther. Lastly, I would like to acknowledge the love and support of my significant other, Emma Jane Hopkins. She has helped me see through roadblocks of my work and of my life and I am so grateful to have her by my side. If not for all these people mentioned and more, this dissertation would have not been possible.

One special acknowledgement for my advisor who has given me the guidance and opportunity to work on so many different projects. Jagjit Nanda, thank you for your time and patience

ABSTRACT

Energy storage devices have undergone development for decades. Much of the research is focused on the improvement of energy density by developing existing electrodes and investigating novel electrode materials. This has led to the overall improvement of traditional lithium-ion batteries, but also the discovery of new energy storage devices such sodium-ion batteries, redox flow batteries, solid electrolyte-based batteries, and many more. As the field expands, fundamental research is necessary to fully ascertain the validity of these novel systems for long term success. One of the most important components to all electrochemical energy storage devices such as batteries and supercapacitors is the electrolyte that allows for the conduction of ions. An ideal electrolyte needs a high ionic conductivity, high chemical stability, low cost, and works well in the desired operating conditions of the device its housed in. Developing an electrolyte that has all these properties is rare, but through communitive research, many electrolyte systems have found uses in niche and broad applications.

My dissertation research is focused on developing electrolyte for sodium-based systems both batteries and supercapacitors. Though supercapacitors differ from batteries in many ways, the fundamental properties of the electrolyte are important for both applications. Thermal stability of the electrolyte has become a growing concern due to the varied working environments of electronic devices. The work I present studied additives for both high temperature stability and low temperature stability in non-faradaic

conditions to isolate the effects of temperature on the electrolytes during operation. The second scope of my work is studying nonaqueous redox flow batteries and optimizing their working conditions through electrolyte and system development. All this work was accomplished using a combination of electrochemical techniques and characterization techniques. The combination of these techniques has provided enough evidence to show effects of additives on the electrolyte system for thermal stability and for overall device improvement in the redox flow batteries. The work from this dissertation will progress the communal knowledge of the benefits and limitations of the electrolyte systems in my research.

TABLE OF CONTENTS

LIST OF TABLES

LIST OF FIGURES

INTRODUCTION: SODIUM-BASED ELECTROLYTES

Energy storage in the form of batteries has been accepted into almost all forms of modern life: vehicles, portable electric devices, on the electricity grid, and even in our ears. The most common is the lithium-ion battery at around ~60% of all batteries sold as of 2021[1]. The battery market is also seeing a steady growth both in total value, but also in the cost on world resources[2]. Common materials found in batteries are harvested in countries all around the world and some have become more precious as our demands for energy have increased. Alternatives to lithium-ion batteries (LIB) have become common place especially the work towards enabling sodium-ion batteries (SIB). Sodium is ten times more abundant on earth and more easily accessible than lithium. The issues with using sodium are basically a knowledge gap between science and industry and a nontrivial transition from LIBs to SIBs. Sodium ions are 30% larger than lithium ions and have a different interaction with all parts of the battery than its lithium analogue. Simply put, sodium-based electrodes and electrolytes operate much differently than their lithium analogues[3].

These differences have provided new opportunities for chemical and electrochemical investigation for sodium-based materials that were not originally possible in lithium-based materials. This has also made progress much slower than expected as well. Although most studies focus solely on electrode development to increase overall energy density within batteries, some also focus on the development of

sodium-based electrolytes[4]. Electrolytes in batteries act as the conductor of ions and determine many different reactions that effect the overall cycling performance of the battery: solid electrolyte interface (SEI) formation, thermal and voltage stability, side reactions, metal dissolution, etc[4]. Determining a suitable electrolyte is non-trivial as the electrolyte must be stable with all parts of the battery including the electrodes, separator material, cell casing, and current collectors. Some electrolytes have been known to fully decompose during cycling, dissolve current collectors, dissolve electrodes, and many other failure mechanisms[5,6]. Developing electrolytes for any energy storage device takes precise and deliberate measurements that isolate specific properties of the electrolyte.

This thesis focuses on two different frameworks for studying sodium ion electrolytes. The first is the use of chemical additives and cosolvents to improve the thermal stability of sodium-based electrolytes. The second is formatting an electrolyte to allow for the stable cycling of sodium metal anodes in nonaqueous redox flow batteries and exploring new membrane materials for sodium-based redox flow batteries. Each thrust requires its own explanation and will be thoroughly explained in order in the following sections. Each approach uses a combination of electrochemical and characterization techniques to fully explore the fundamental mechanisms of the electrolyte systems.

1.1 How does energy storage work?

Secondary batteries are a class of energy storage that have reversible faradaic redox reactions used to store electricity. A basic construction of battery is a cell casing, current collectors that allow for fast electron conductivity, a separator to block each electrode from physically contacting, the electrodes classified by anode or cathode depending on the relative potentials of their oxidation reaction, and the electrolyte that allows for the conduction of ions through the cell. A representation of a sodium ion battery is shown in Figure 1. The faradaic redox reactions in the electrodes are typically three distinct reaction processes caused by an applied current resulting in the intercalation or storage of sodium between the layers of the electrode material, alloying reactions typical in silicon electrodes where sodium alloys with the electrode material, or conversion reactions where the material changes the structure of the redox active compound[2].

These faradaic redox reactions that are caused by an applied current and described by Equation 1.

Equation 1: $$\boldsymbol{Q = \int_0^t i dt = n N_j F}$$

Equation 1 is Faraday's law of electrolysis where charge, Q, is equal to the amount of faradaic current, i, applied over time, t, which is also equal the product of the number of electrons transferred during the process, n, number of moles of a given species, N_j, and Faraday's constant, F.

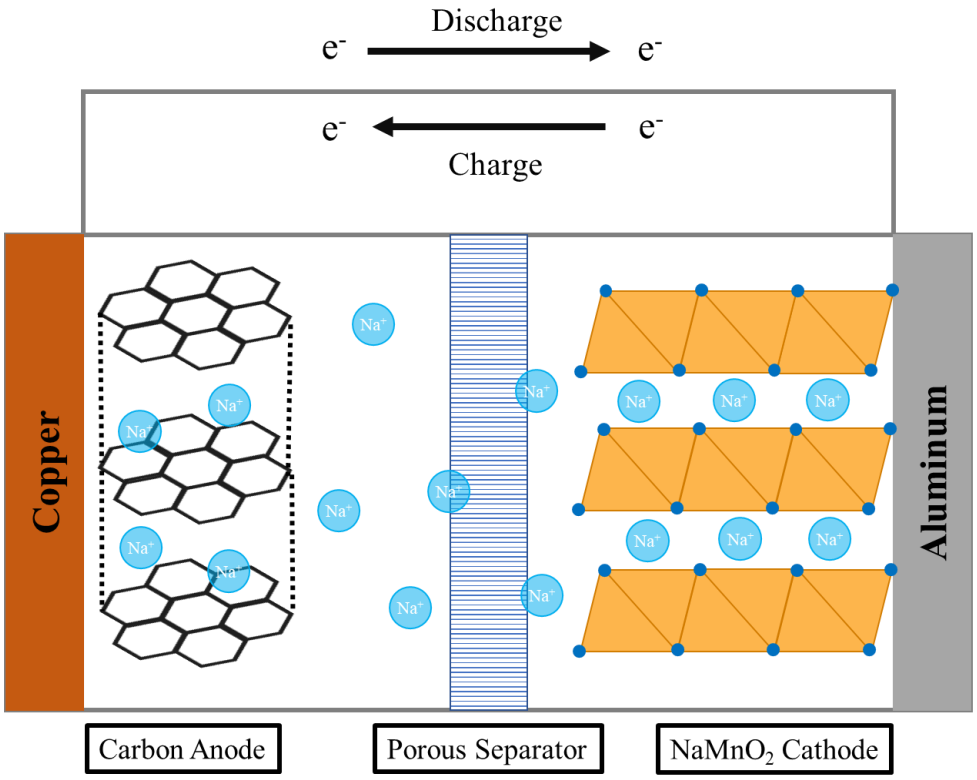

Figure 1: A schematic of a typical sodium ion battery. The battery contains a carbon anode coated on copper foil and sodium manganese oxide cathode coated on aluminum foil.

The storage of the ions caused by an applied current can be reversed allowing for the reversible storage of electricity. The kinetics of these redox reactions are described in the Butler-Volmer equation shown in Equation 2.

Equation 2: $$\boldsymbol{i = FAk_0\left[[R]_0 exp\left(\frac{(1-\alpha)F(E-E^{0\prime})}{RT}\right) - [O]_0 exp\left(-\frac{\alpha F(E-E^{0\prime})}{RT}\right)\right]}$$

The Butler-Volmer equation equates the net electrolyte current, *i*, with an expression of the product of Faraday's constant, *F*, the electrode surface area, *A*, the standard electrochemical rate constant, k_0, the species that is to be reduced, *O*¸ its reduced form, *R*, the universal gas constant, *R*, the temperature of the system, *T*¸ the transfer coefficient, α, and the overpotential $(E-E_0)$. The Nernst equation is shown in Equation 3 and relates the OCV with the concentration of the ratio of oxidized and reduced species.

Equation 3: $$\boldsymbol{E = E_0 + \frac{RT}{nF} ln\left(\frac{C_{ox}}{C_{red}} * \frac{\gamma_{ox}}{\gamma_{red}}\right)}$$

The Nernst equation equates the potential difference, *E*, to the sum of standard redox potential for a give species, E_0, the universal gas constant, *R*, the temperature, *T*, the number of equivalent electrons of the redox reaction, *n*, Faraday's constant, *F*, the concentration of oxidized and reduced species, $C_{ox,red}$, and the activity coefficient of the reduced and oxidized species, $\gamma_{ox,red}$. The Nernst equation can be used to predict the concentration ratio as a function of measured potential of a given cell and vice versa. Some additional variables may be necessary to give the most accurate prediction such as the concentration of other species necessary for the redox reaction to occur.

The amount of energy stored in the battery is related to Eq 1 and is further modified in Equation 4 for battery capacity as function or mass or area:

Equation 4: $$\boldsymbol{Q_b = m_b c_b \; or \; Q_b = A_b c_b}$$

The equation relates the amount of energy stored as a function of time or charge, *Q*, to the mass of the redox active material, m_b, or area of the active material on the electrode, A_b, by the specific energy capacity of the material that is determined by the faradaic redox reaction, c_b.

These faradaic redox reactions are not the only form of energy storage as non-faradaic energy storage is possible with the use of electric double layer capacitors (EDLCs). In EDLCs, the energy is stored on the surface of the electrode. The storage is possible due to the formation of an electric double layer that forms when a current or voltage is applied to an electrochemical device. This double layer has been described by various scientists. Helmholtz described the layer The amount of energy stored in terms of Farads is determined by a product of an applied current, *I*, and the ratio between the change in time, ΔT, and the change in voltage during that time frame ΔV as shown in Equation 5:

Equation 5: $$\boldsymbol{C = I * \frac{\Delta T}{\Delta V}}$$

Capacitance can then be equated to a specific gravimetric capacitance or areal capacitance as shown in Equation 6:

Equation 6: $$C_A = J_A * \frac{\Delta T}{\Delta V} \; or \; C_m = J_m * \frac{\Delta T}{\Delta V}$$

Equation 6 modifies Eq. 5 by applying a current density, J_A (A/cm^2), or a gravimetric current, J_m (A/g), and results in either an areal capacitance, C_A (F/cm^2), or specific capacitance, C_m (F/g).

In an EDLC with two electrodes, the total capacitance is equated to the capacitance of each electrode as is shown in Equation 7:

Equation 7: $$C_{total} = \frac{C_1 C_2}{C_1 + C_2}$$

The total capacitance, c_{total}, is a ratio between the product of the capacitance of each capacitor, c_1, c_2, over the sum of the capacitance of the same capacitors.

As mentioned before, electrolytes act as a conductor for ions in electrochemical energy storage devices. Liquid electrolytes are a combination of solvents and salts. Most classes of liquid electrolytes are either aqueous or nonaqueous depending on solvent selection. Though aqueous electrolytes have been studied for decades, most modern SIBs are based around organic electrolytes[7–9]. Organic electrolytes typically have large operating voltage windows (>3V), access to alkali metals such as sodium, and other benefits such as thermal and chemical stability[10,11].

1.2 Intrinsic properties of electrolytes

As mentioned, electrolytes have an important role in the viability of batteries. Electrolytes allow for the movement of ions from one electrode to another. The rate at which ions can diffuse through the electrolyte when a potential or current is applied is

called ionic conductivity. In organic electrolytes, a typical and value is around 10 mS/cm, but this number fluctuates depending on what kind of liquid electrolyte referred to[12,13]. Ionic conductivity shares a distinct relationship with polarizability of the dielectric in solution or dielectric constant and the resistance to change shape of a solution or viscosity. Typically, decreases in viscosity lead to increases in ionic conductivity[14]. Some studies have shown additives that improve ionic conductivity by lowering the viscosity of the solution or by coordination of solvent molecules through intermolecular interactions between the solvent and additive[15]. Predicting changes in ionic conductivity has proven to be difficult. Measuring conductivity as a function of temperature, electrolyte composition, concentration of salt, and various other conditions of electrolyte is relatively straightforward and is covered later in the text.

Though ionic conductivity is an important focus, other intrinsic properties of electrolytes have been improved using additives. Flammability of organic solvents is a well understood issue and some additives have been used as flame retardants or to inhibit thermal runaway caused by chemical reactions[16]. Wettability, thermal stability, cost, and safety have all been improved using additives and cosolvents over the last decade[4,17–20], but each property typically requires a unique solution based on the solvent, salts, and the electrochemical processes taking place within the system. This need for many different combinations of solutions makes improving the intrinsic properties of electrolyte a nontrivial process.

1.3 Electrochemical properties of electrolytes

Electrolytes also dictate many of the limitations of electrochemical processes taken place in each system. Using a traditional lithium-ion battery as a frame of reference, electrolytes interact with the electrodes, separator, and cell casing of the battery. At each of these interfaces, electrolytes can react to form passivation layers either chemically or electrochemically. Passivation layers are also expected in faradaic processes[21]. These interfaces are commonly referred to as solid electrolyte interfaces (SEI)[22,23]. An SEI is composed of electrolyte degradation products on the surface an electrode. In lithium-ion batteries, it common to see SEIs composed of lithium fluorides, lithium oxides, lithium polycarbonates, organic polymers, and many more species depending on the composition of electrolyte[24]. There are many examples of unsuitable SEIs, but an ideal SEI is one that is ionic conductive to the cation of the system, but electronically insulating so no further degradation of the electrolyte is possible. This is also the case in sodium ion electrolytes and studies of SEIs in sodium electrolytes are still being conducted[25].

Another important factor is the electrochemical stability window of your electrolyte solution. This is dictated by all components within an electrolyte solution. Organic solvents have a wide range of voltage windows. The limits of the voltage window are dependent on the oxidative and reductive stability of each component. Carbonates such as ethyl carbonate (EC), dimethyl carbonate (DMC), and diethyl carbonate (DEC) are show high oxidative stability at around 4.5-4.8 V vs Li/Li^+ but

would be unusable with electrodes that operate at redox potentials greater than 4.8V vs Li/Li^{+}[2,26]. Salts used in the solutions must also be stable across the desired voltage window as well or irreversible degradation of the electrolyte is possible. This limitation is also true for any additives or cosolvents used in the electrolyte solution.

1.4 Electrochemical and characterization methods commonly used in studying electrolytes

As expected, the research of electrolytes is a difficult process, but there are many techniques to elucidate the mechanisms, benefits, and drawbacks of electrolyte solutions. Electrolyte studies are usually a combination of electrochemical techniques to gauge at what potential do reactions take place, the stability of those reactions, the stability of the electrolyte in different environments, and more. This is performed ex-situ or in-situ with various characterization techniques that identify the products of redox reactions, the rate at which those reactions take place, coordination of salt and solvent molecules, chemical side reactions, etc[27–29]. Both approaches have their limitations and drawbacks, but the combination of both leads to a deeper understanding of the electrolyte.

1.4.1 Electrochemical measurements: CVs, GCs, and EIS

There are many electrochemical measurements possible, but the three most used in this thesis are cyclic voltammetry (CV), galvanostatic cycling (GC), and electrochemical impedance spectroscopy. Each of these are performed in one of three distinct configurations in my studies: coin cells, EL-cells, and redox flow batteries. Coin

cells or button cells are commonplace in electrochemical measurements. Coin cells are small cylindrical cells that are quick to fabricate, and many can be cycled in tandem given the equipment is available. They are comprised of a stainless-steel casing and house in order, a stainless-steel spring, space, electrode, separator, and electrode. These cells are then pressed and sealed with a polypropylene gasket. El-cells are like coin cells in fabrication but are capable of being opened and resealed with ease. This allows for accurate postmortem measurements and the introduction of electrolyte additives after cycling. Redox flow batteries are the last are comprised of two tanks with a cell stack where electrolytes meet allowing for the conduction ions through a membrane. The specific redox flow batteries, but for my work will be explained in more detail later in the text.

Cyclic voltammetry (CV) is used to determine the redox potential of both the redox active species in cells and the electrochemical voltage window of an electrolyte solution. Other redox potentials that are important to identify with CVs are possible side reactions that may be electrochemically induced. This is also the extent of what CVs can identify. It can measure if something is occurring, for how long that redox reaction is occurring as function of time and estimate of how much energy is used in that reaction. CVs are graphed as a function of current vs potential. The potential is swept at specific scan rate in volts per second between two potential limits. Redox reactions are displayed as peaks and are considered reversible if the same peak appears during the reverse sweep. The other possible responses in batteries are quasi reversible and irreversible redox

reactions. In all electrochemical devices, an electric double layer forms on the surface of the electrode being measured. If no redox reaction is present, CV can measure the energy stored on the surface of the electrode or capacitance. This is important for non-faradaic devices such as capacitors. That CV is represented in Figure 2 where the shape is typically similar to a square but has peaks towards the end of the range due to response from the instability of the electrolyte at the given potential. Also, the area under the curve can be equated to capacitance of both electrodes by using Equation 8:

Equation 8: $$C_{Tot} = \frac{I_{measured}}{V_{rate}}$$

This equation equates total capacitance, C_{Tot}, to the ratio of the measured current over a given range using an integral of the voltage range, $I_{measured}$, to the scan rate used for the CV, V_{rate}. The integral of the into CV can be performed as well, but the resulting capacitance would need to be divided by two.

Galvanostatic cycling (GC) is a common technique that determines the amount of capacity stored in or on a given electrode material by applying a constant current over a specified period or voltage limit as show in Figure 3a. This measurement leads to several different plots that reflect the electrochemical performance of the studied system. A few typical examples are shown in Figure 3. Voltage profiles show at which potentials reactions take place and for how long.

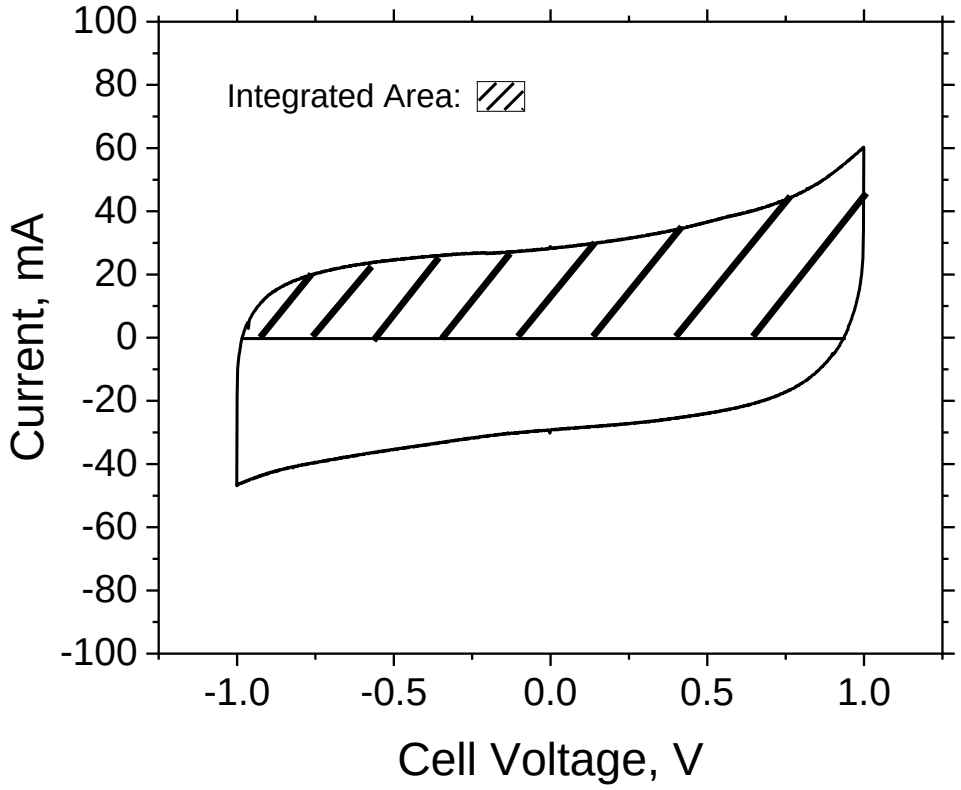

Figure 2: A cyclic voltammetry measurement typical for a supercapacitor. The lined area represents the area that can be integrated to measure capacitance over a given voltage range.

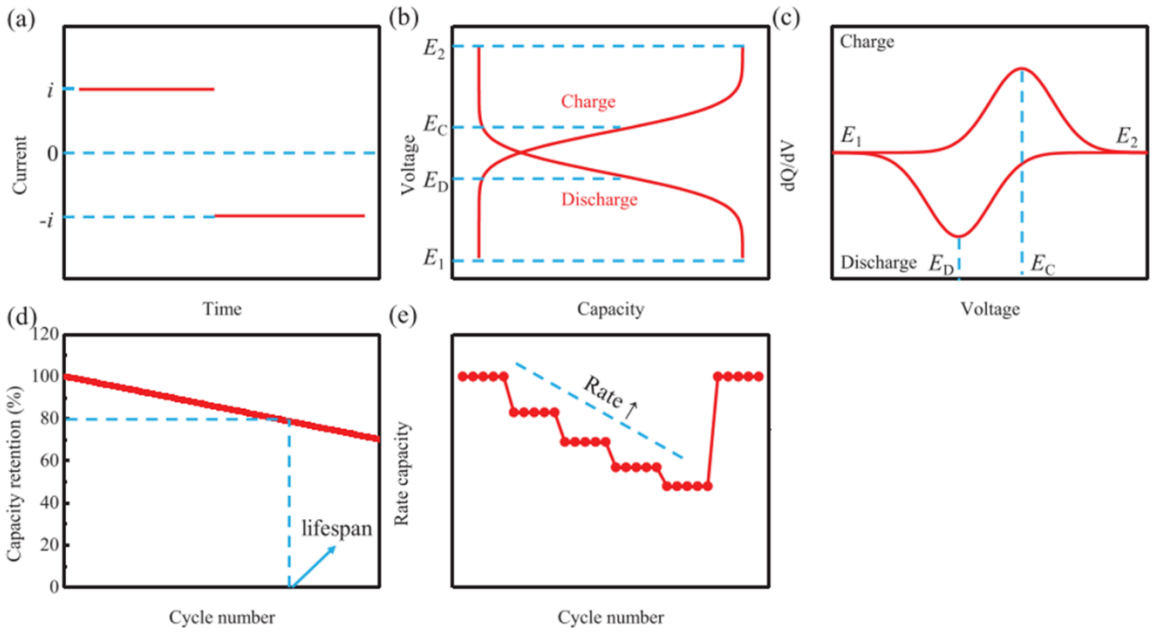

Figure 3: Galvanostatic cycling measurements performed in typical battery experiments. (a) A constant current plot, (b) a voltage profile, (c) dQ/dV plot, (d) capacity retention, and (e) rate capability plot in a typical battery measurement.[30]

They also show how distinct of a reaction is taking place as and commonly referred to as voltage plateaus. These plateaus can be extremely distinct or can be sloppy depending on the kinetics or the reaction and if other reactions are taking place at the same time. Voltage profiles are also useful for identifying which reactions are fading with time. Capacity loss can be tracked as a function of cycling with both a dQ/dV plot or capacity retention plot. Both are used in literature with dQ/dV plots being popular amongst well established electrode materials. Rate capability measurements show how well the system can handle high cycling rates/ higher currents by changing the current during cycling and gauging effective capacity. It is very typical that electrode materials lose usable capacity as current rates increase. The difference between final capacity during the charge and discharge of a cell during cycling can be translated to a coulombic efficiency (CE). CE is the efficiency of each cycle and can be used to determine the cycle life of a given cell. Another important result is the data can be plotted as a function of potential versus capacity. This is commonly referred to as a voltage profile. The voltage profile of typical battery can be seen in Figure 3. The plateaus in the voltage represent redox reactions taking place as the current is being applied.

Electrochemical impedance spectroscopy (EIS) is a technique that measures the resistance response of a cell across by applying an ac voltage perturbation and measuring current. Using a small voltage perturbation result in a linear or pseudo-linear response. This response to the sinusoidal voltage perturbation E will be a sinusoid current I at the

same frequency but shifted in phase. The resulting impedance *Z* is a complex number in Equation 9:

Equation 9: $$\boldsymbol{Z = \frac{E}{I} = Z_0 \exp(j\varphi) = Z_0(cos\varphi + j\, sin\varphi)}$$

This complex number is plotted in a Nyquist plot where the imaginary part of the impedance is plotted against the real impedance[9]. The shape and intercepts of this plot can be fit against equivalent circuits to calculate the capacitance or equivalent series resistance (ESR) within the cell.

The shape of the line can also be attributed to passivation layers, the movement of ions through pores, the resistance and conductivity of the electrolyte, and more[31–34]. This technique also requires are deep understanding of the system being studied as the data can be misinterpreted easily. As such, interpretation of battery EIS is non-trivial and is usually used in combination with other electrochemical measurements. A typical LIB EIS spectrum is shown in Figure 4. Each section of the plot represents a different process or interface being measured and is explained in the figure caption. This plot is of an ideal system. With each new electrode, electrolyte, or cell configuration, the EIS response can change completely even in the most well-known of systems.

1.4.2 Spectroscopic characterization techniques: FTIR, Raman, NMR, and DSC

Fourier transform infrared spectroscopy (FTIR) is a technique that measures the absorbance of infrared light by molecules. The absorbance results in the excitation of

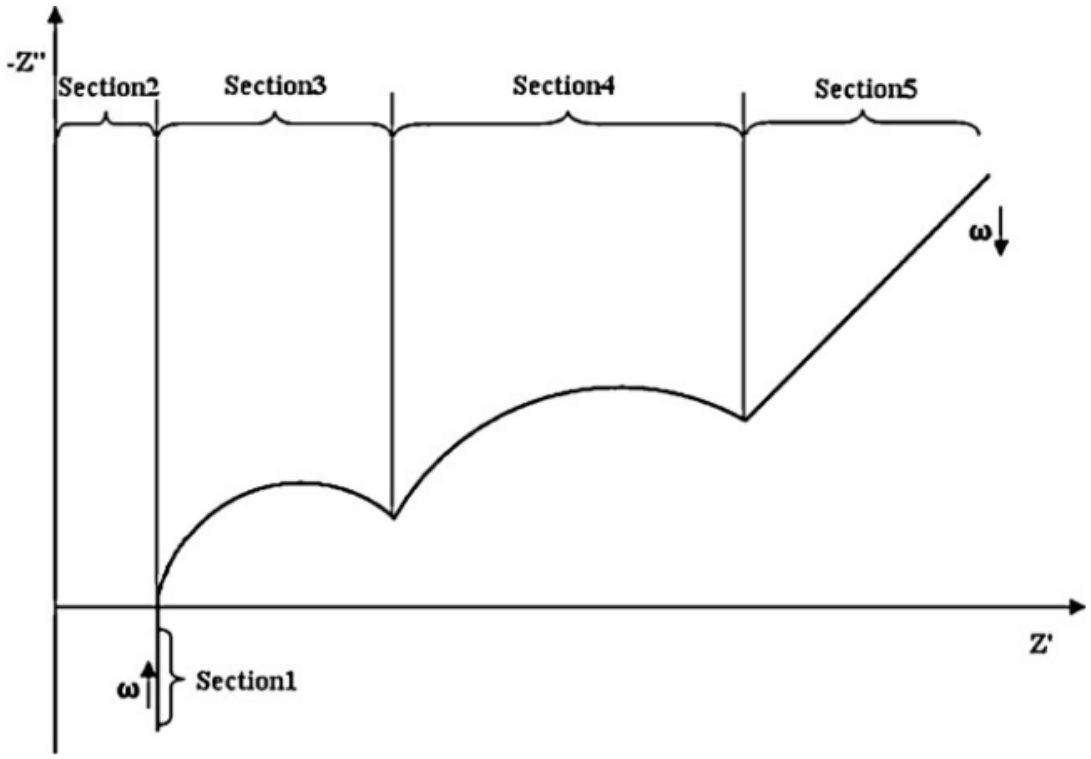

Figure 4: EIS spectra of a typical lithium-ion battery. Section 1 represent the impedance of the metallic elements in the system (i.e., wires, cell components). Section 2 represents the sum ohmic resistance of the current collectors, active material, electrolytes, and separator. Section 3 is a semi-circle associated with SEI on the surface of the active material. Section 4 is a semi-circle associated with double layer capacitance and charge transfer resistance at the electrodes. Section 5 is associated with diffusion processes in the active material.[35]

bonds in molecules which can be related to a specific wavenumber. This allows for the identification of different species that are solid, liquid, or gas phase that have FTIR active bonding[29,36]. Molecules that have permanent dipole moments typically have strong FTIR active peaks. Some molecules and bonds are inherently difficult to measure because of their total lack or weak dipole moment. In electrochemical research, FTIR is typically employed to track changes in the structure of electrode materials after electrochemical and/or chemical changes[28]. For electrolytes, FTIR can track into changes in the electrolyte composition during cycling, new species forming as a function of time, temperature or concentration of additives, and potential subtle shifts in the structure from coordination effects or other intramolecular interactions between molecules[23,27,28,37,38]. Careful analysis is important for using FTIR because many bonds can overlap between species especially in organic electrolytes where the solvent may have similar bonding to the salt or additives present in the solution. Tracking the degradation of electrolyte is uniquely at a disadvantage as decomposition products may be incredibly similar to the reactants[39].

Raman spectroscopy is typically used in tandem with FTIR. Raman spectroscopy relies on the scattering of lasers by molecules. The scattered light has a specific wavelength that can be related to excitation of bonds of a molecule. Molecules with a high polarizability have strong Raman responses. Typically, FTIR weak signals are strong in Raman and vice versa. Combining the two techniques can deliver a deeper understanding of changes in the electrolyte solution and identifying unknown species.

Raman measurements can elucidate specific qualities of electrolyte including coordination of electrolyte solution species, and the products of electrochemical and chemical processes[27,40–42]. Ex-situ measurements are the main form of electrolyte characterization, but some studies have used in-situ and in-operando measurements, but typically the issue of overlapping peaks remains common[42]. This is especially true for looking at subtle changes in the electrolytes as the signals from the solvent and salt are high in comparison and can go unnoticed by the Raman measurement.

Nuclear magnetic resonance (NMR) spectroscopy is a technique that observes the local magnetic fields around different atomic nuclei. NMR has shown to be a powerful tool in battery research for many electrolytes including organic, aqueous, ceramics, and polymer electrolytes[25,43,44]. For liquid electrolytes, NMR can be used to identify the formation of products from chemical and electrochemical reactions including from degradation, electrochemical redox reactions, side reactions, etc[12,25,45]. Another use is using diffusion NMR to track the coordination of different species within the electrolyte solutions. This can give insight into the solvation sheath of cations, the complexation of electrolyte species, and the transference number of the electrolyte. NMR works well when deuterated solvents for NMR but many of the solvents used in organic electrolyte systems can be difficult and expensive to fully deuterate.

Differential scanning calorimetry (DSC) measures the amount of heat necessary to increase or decrease the temperature of a given sample in comparison to a reference material. A typical DSC curve is shown in Figure 5. This technique is useful for

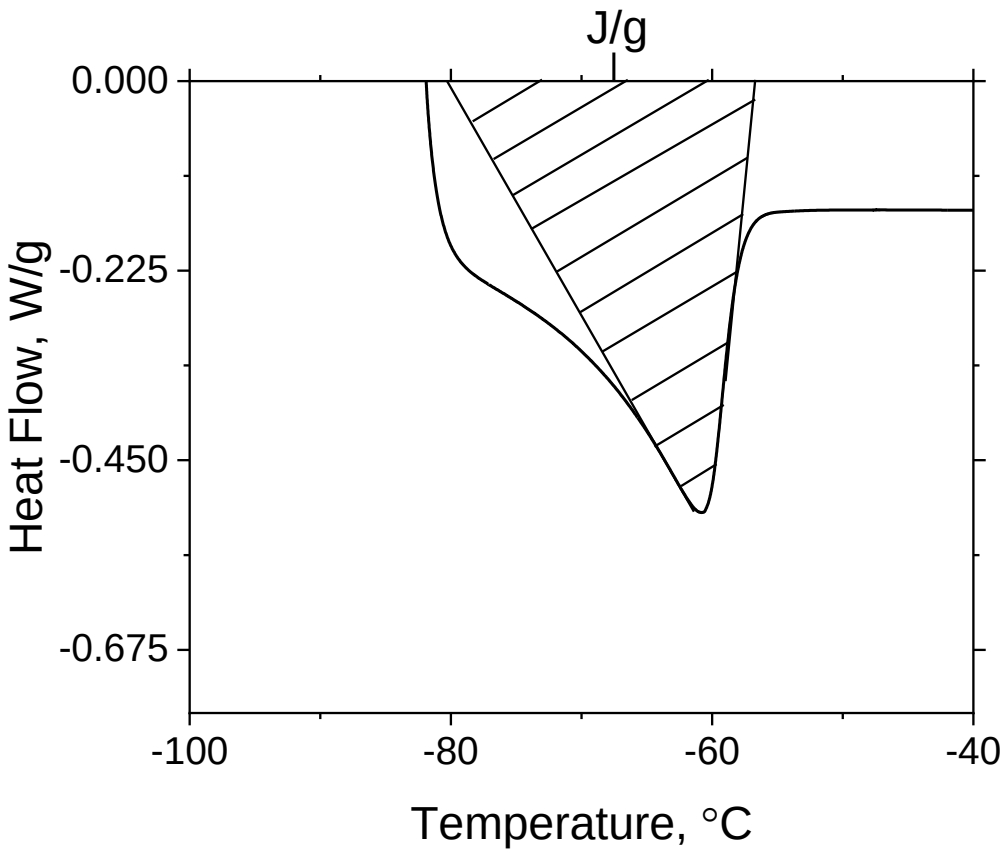

Figure 5: A typical DSC curve for liquid electrolytes. The integrated area can be equated the heat of formation of the electrolyte.

measuring the freezing/ melting point of the liquid electrolytes. It can also detect the presence of eutectic impurities and used to measure the eutectic point of electrolytes. This has become a common technique for studying the effects of co-solvents and electrolyte combination to either lower the freezing point of electrolyte to in improve low temperature stability or increase the boiling point for high temperature stability[46,47]. Also, the heat of formation, which is important for understanding the intermolecular interactions of liquid electrolytes, can be measured by integrating the DSC curve between the onset and offset curves of a given freezing/ melting point as shown in Figure 5.

1.5 Why sodium chemistries for energy storage?

Lithium and lead-acid are two of the most popular battery chemistries industrially, but the growth of the exploration of sodium ion chemistries have increased in the last few decades. The main reasoning is looking for a more environmentally conscience alternative to lithium-ion batteries. Sodium is naturally more abundant than lithium, and from cost analysis much cheaper and easier to harvest than lithium[3]. The issue with transition to sodium from lithium is the major difference in chemical and electrochemical properties of sodium ions and compounds. One of the earliest studies was looking to replace lithium cobalt oxide, one of the most common LIB cathodes, with sodium cobalt oxide, but both materials do not have the same electrochemical pathways and results in a lower capacity, less stable cathode material. The transition from lithium electrolyte to sodium electrolyte has the same issues. The way that sodium electrolytes break down,

conduct ions, and their chemical stability are all different enough to cause a non-one to one transition from lithium ion[3,48,49]. This means that the studies performed in lithium ion may not produce the same or similar results in lithium ion. This also means that it will be necessary to reexamine almost all materials already explored in LIB in SIBs.

Sodium ion electrolytes typically have a higher ionic conductivity than their lithium analogues and some previous electrolyte additives thought to be useless in LIBs could be extremely useful in SIBs[4,43]. The most common electrolyte salts used in SIBs are typically sodium hexafluorophosphate ($NaPF_6$), sodium trifluoromethosulfonate (NaOTf), sodium Bis(trifluoromethanesulfonyl)imide (NaTFSI), and sodium perchlorate ($NaClO_4$).

2. Thermal stability additives for sodium-based electrolytes

2.1 High temperature stability for $NaPF_6$-based electrolytes

Lithium hexafluorophosphate ($LiPF_6$) in carbonate solvents is the most common electrolyte used in traditional lithium-ion batteries in industry. This electrolyte delivers a decent >4V electrochemical voltage window, long term chemical stability, forms a good SEI on both carbon and nickel manganese cobalt oxide (NMC), and has decent ionic conductivity. The most common issues associated with it are its high flammability, instability at higher temperatures and possible presence of hydrofluoric acid[45]. Sodium hexafluorophosphate has been used in many SIB studies and shows similar qualities to its lithium analogue including its instability at higher temperatures (>40 °C)[39].The instability

is based on PF_6 existing in an equilibrium with PF_5 in solution. At room temperature, the presence of PF_5 does not lead to detrimental degradation of the electrolyte, but as the temperature increases, the equilibrium is more favorable for PF_5. PF_5 will then react with almost all components of the electrolyte and form a variety of organic and inorganic compounds which then react with PF_5[50]. This causes an autocatalytic degradation of the electrolyte and ultimately device failure.

In LIB studies, it is known that PF_5 exists as a strong Lewis acid and can be complexed with Lewis bases to stop further formation of PF_5 and satisfying the equilibrium between PF_5 and PF_6 in solution. In the literature, each Lewis base used as an additive also can affect the electrochemical voltage window, ionic conductivity, and SEI formation of the batteries as well[51–53]. Each study also shows that each additive can improve the thermal stability of the electrolyte to varying degrees. In one study, it was shown that use of HMPA maintained the stability of $LiPF_6$ in carbonate solvents for over a year after being stored at greater than 80 °C[53]. Chapter one and two delved into two studies that was conducted by me that explores increasing the high temperature stability of $NaPF_6$ in monoglyme using strong Lewis bases.

Studying instabilities in batteries is non-trivial as one large component to any scientific study is isolating the effects of changes to your system. Any changes to electrolytes for batteries can affect the electrochemical voltage window, cycling rate, SEI formation, and many more chemical and electrochemical processes. In my work, I instead

study these electrolytes in a supercapacitor framework. Supercapacitors offer an easier approach to studying electrolytes from the lack of faradaic reactions[34,54].

2.1.1 The benefits of supercapacitors for temperature stability measurements for electrolytes

Though different kinds of supercapacitors exist, this thesis work focuses on the use of electric double layer capacitors (EDLC) using high surface area carbon electrode. The electric double layer forms when a voltage or current is applied across a system. The double layer is described by Helmholtz as a layer of cations and anions coordinated on the surface an electrode. The use of high surface area carbons allows for the total energy stored on the surface or capacitance to be approximately 10 F/g to 200 F/g depending on the electrode and electrolyte[55]. This form of energy storage is considered non-faradaic as no electrochemical redox reactions are taking place in the electrodes.

Non-faradaic energy storage is limited in energy density but allow for the isolation of properties in electrolytes. Any change in electrolyte composition for a faradaic cell can affect more than one process or property in the device. For example, studying thermal stability of electrolyte in batteries can be difficult as faradaic redox reactions cause some degradation of the electrolyte with each cycle making elucidating electrolyte degradation from thermal stability or electrochemical stability can be difficult. In supercapacitors, the thermal stability of the electrolyte can be gauged with relative ease as all degradation occurring can be attributed to thermal instability of the electrolyte. Determining stable cycling parameters for the supercapacitors is important as the voltage

stability of the electrolyte can cause degradation if cycled beyond the limits of the electrolyte.

2.1.2 Tracking the degradation of electrolyte with electrochemical measurements

Measuring the thermal stability of the electrolyte through electrochemical measurements is performed in a combination of EIS, galvanostatic cycling, and possibly cyclic voltammetry. Ideal EIS supercapacitor Nyquist response of a supercapacitors with two high surface area carbon electrodes and a porous separator gives a semicircle followed by a 45° line then a vertical tail when measuring from low frequency to low frequency[56] and is shown in Figure 6. The semicircle can be attributed to resistance through the interfaces between the electrode cast and current collector. The 45-degree line is attributed to the diffusion of ions in the pores of the carbon electrode. The vertical tail can be extrapolated to -Im(Z)=0 to measure the capacitance of the electrode at the applied voltage by fitting against an equivalent circuit of one resistor and one capacitor in series. If the electrolyte degrades from thermal degradation, a growth in the semicircle due to the passivation of the electrode surface or a bend in the vertical tail can be expected as shown in Figure 6. EIS can be complimented with galvanostatic cycling. GC of supercapacitors as a function of temperature and time can track changes in total capacitance. Loss in the total capacitance can be caused by electrolyte degradation and the subsequent passivation of the electrode surface. As electrolyte breakdown continues, irreversible loss in capacitance is expected and measurable. Combining these two measurements can provide enough evidence to confirm the thermal instability of

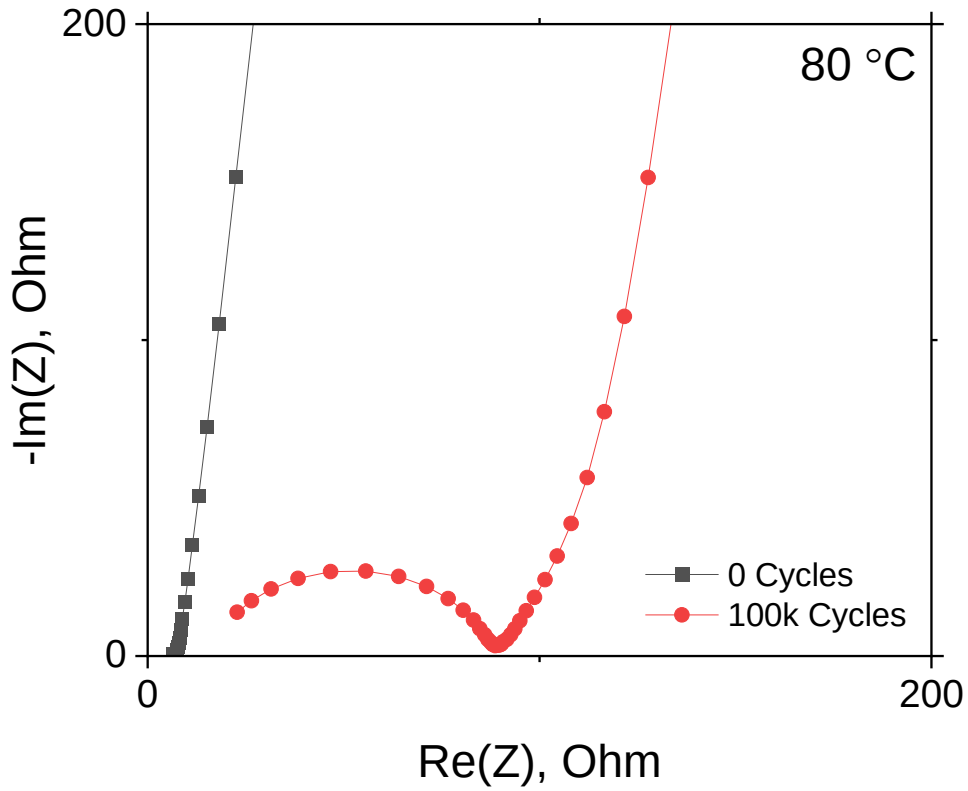

Figure 6: A Nyquist impedance plot for a supercapacitor both before thermal degradation of the electrolyte (black) and after degradation of the electrolyte (red)

electrolytes in supercapacitors. CVs measure the electrochemical voltage windows of electrolytes. CVs as a function of temperature can measure changes in the voltage stability. Typically, electrolytes have high ionic conductivities at higher temperatures but can decrease the voltage window as well.

2.1.3 Tracking degradation of electrolyte with spectroscopic techniques

Electrochemical measurements are commonly paired with different spectroscopies as stated previously. Thermal stability of electrolytes can also be gauged by looking the products of degradation reactions. FTIR and Raman may potentially detect the presence of newly formed species in solution but can be difficult due to the intensity of solvent and salt compounds. Also overlap of peaks attributed to the solution and degradation products is possible. FTIR performed on the gas phase of the electrolyte can prove useful if known degradation species are gaseous such as PF_5. In the case of PF_5, tracking changes in the gas phase of the electrolyte solution is invaluable as liquid phase FTIR measurements result in almost indiscernible difference between PF_6 and PF_5.

Raman of liquid electrolyte can also be difficult due to fluorescence. Fluorescence in measurement is notoriously high in glyme electrolytes and in the presence of PF_6-based electrolytes. Other techniques can also be used to track changes in the electrolyte, but the focus of this work is a mixture of applied research and the fundamentals in the differences in performance.

2.1.4 Determining complexation strength between additives and PF_5

As mentioned previously, the inhibition of the degradation of PF_6 into PF_5 through the Lewis bases has been studied in LIBs with varying degrees of success. One way to study these complexations is performing NMR measurements on the electrolyte solution. The measurements are typically electrolyte solutions that have been exposed to higher temperatures and tracking the formation of new species or the addition of peaks that don't shift with time. These NMR experiments have been key in understanding both the degradation pathway of PF_5 and the interactions that PF_5 has with additives and other electrolyte components[16]. The investigation of PF_5 with additives have shown that the strength of the Lewis base is important for the long-term thermal stability of the electrolyte and the stronger the base is the more stable the electrolyte will be in lithium-ion battery electrolytes.

2.2 Low temperature performance of NaTFSI-based electrolytes

Low temperature environments for electrochemical storage devices have grown in interest because of low temperature environments such as space exploration. The issue with most liquid electrolytes is that organics freeze at low temperature (>40 °C) or significant decrease in ionic conductivity can occur[57]. To enable improved low temperature performance, new electrolyte compositions are being explore. One of much interest both in LIBs and SIBs is TFSI-based electrolytes. LiTFSI and NaTFSI is known to have incredibly high solubility in water (28 moles of solvent/ kg of solvent) and these high concentration electrolytes are commonly known as water-in-salt or solvent-in-salt

electrolytes[58]. The high concentration causes unique solution properties such as extended voltage windows, lower freezing points, and improvements in various other electrochemical properties. Since this discovery, LiTFSI has become a common topic in electrolyte literature. NaTFSI has also been explored for decades as alternative to $NaPF_6$ but has issues with dissolving aluminum in traditional SIBs[59].

Such as with the high temperature measurements, non-faradaic approaches to studying electrolytes at low temperature provide benefits. Batteries are limited for low temperature applications as the faradaic redox reactions are detrimentally impacted by low temperatures to the point of not being able proceed[60]. Supercapacitors are not as severely affected in terms of energy storage by low temperatures as non-faradaic are less affected kinetically by low temperatures. This allows for cycling at temperatures below -20 °C where common battery electrodes are limited. Supercapacitor electrolytes are commonly measured down to -40 °C but typically limited to this temperature due to electrolyte freezing point. Also, high surface area carbon electrodes have recently been studied at temperatures as low as -60 °C far below the freezing point of the electrolyte but still capable of being cycled. This combination of benefits makes EDLC using high surface area carbons an ideal framework for studying the limitations of NaTFSI electrolytes at lower temperatures.

2.2.1 Electrochemical and spectroscopic approach to gauging lower temperature performance

Expected changes in the electrolyte at lower temperatures is lower ionic conductivity, lower capacitance in the carbon electrodes over a specific cycling parameter, and changes in the EIS response due to changes in the conductivity of the electrolyte. Though these changes are predicted, the extent of these changes can be difficult to predict because the electrodes and electrolyte dictate performance at low temperatures. Measuring changes in ionic conductivity and capacitance can be done by using a combination of EIS and galvanostatic cycling as function of temperature. As mentioned before, ionic conductivity and capacitance are relatively straightforward measurements using EIS. Ionic conductivity is typically measured using two planar electrode that allow for now redox reactions or "blocking" electrodes with a known distance between each electrode. The ionic conductivity is calculated using Equation 10:

$$\textbf{Equation 10:} \quad \boldsymbol{\sigma = \frac{1}{R}\frac{L}{A}}$$

The ionic conductivity of the electrolyte, σ, is equal to the inverse of the measured resistance, R, multiplied by the ratio of the distance between the two electrodes, L, and the surface area of those electrodes, A. The resistance of the electrolyte is extrapolated to the point at which Re(Z)=0 as shown in Figure 7a. This is the common way of measuring bulk resistance, but in a device the ionic conductivity is affected by the separator and electrodes. The effective ionic conductivity can be extrapolated in a similar way and an example is shown in Figure 7b. The EIS response shown in Figure 7b highlights the

expected response in cells containing carbon electrodes and a separator found in the capacitors built in the following chapters.

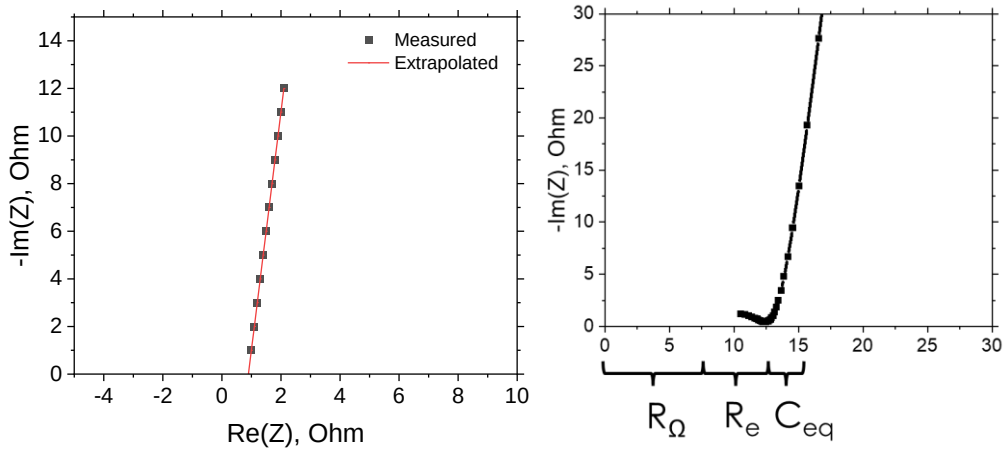

Figure 7: (a) An example of an EIS measurement taken in a blocking electrode configuration with the resistance of the electrolyte extrapolated from the measured impedance of the cell. (b) The EIS measurement of cell containing carbon electrodes and a Celgard separator used as an example for determining the effective conductivity of the electrolyte.

The impedance response is divided into the three sections: the bulk conductivity which is affected by the conductivity of the electrolyte and the resistance of the separator, R_{Ω}, the resistance of ions moving through the electrode, R_e, and the capacitive linear tail, C_{eq}. Using both the bulk conductivity and electrode resistance, Eq. 9 can be translated to an effective ionic conductivity through the electrode and separator:

Equation 11: $$\sigma_{eff} = \frac{1}{(R_{\Omega}+R_e)}\frac{L}{A}$$

Conductivity is typically plotted as a function of temperature and referred to as Arrhenius plots. Arrhenius plots are commonplace in electrolyte studies as they provide insight into major changes in conductivity and processes affected by temperature or electrolyte composition. A typical Arrhenius plot is shown in Figure 8. The slope of an Arrhenius plot can be used to calculate the activation energy, E_a, of chemical process or reaction and is described the Arrhenius equation shown in Equation 12:

Equation 12: $$k = Ae^{-\frac{E_a}{RT}}$$

The equation relates the rate constant, k, with a pre-exponential factor, A, absolute temperature, T, the gas constant, R, and activation energy, E_a. The Arrhenius equation as mentioned is commonly used in ionic conductivity studies of many kinds of electrolyte and have been modified to account for temperature dependent processes as well[61]. The activation energy calculated from these plots can be used to compare and discuss changes in the overall chemical environment of the solvated ions

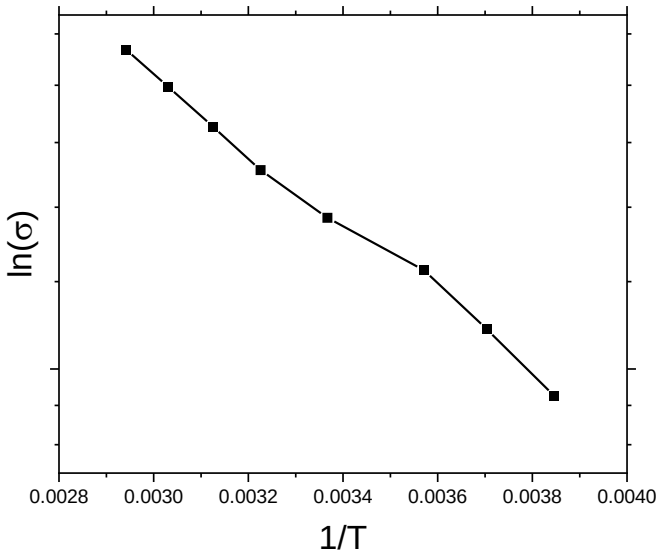

Figure 8: An example of Arrhenius plot having a natural log ionic conductivity vertical axis and an inverse temperature horizontal axis.

such as lowering ion mobility barriers, promoting movement in ions through additives, or other similar effects[62].

The linearity of the slope also gives evidence of processes taking place as the temperature is changed. As you approach lower temperatures, the slope of the line quickly skews from linear to of an exponential approach to zero. This is typically due to freezing of the electrolyte. This causes the diffusion of ions to become affected by something more than temperature in this case a phase change that ultimately blocks the diffusion of ions.

Shifts in electrochemical performance can be complimented with DSC measurements. DSC measurements of electrolytes to measure changes in the freezing point/ melting point as a function of electrolyte composition. DSC is key in determining the eutectic point of electrolytes or the point at which the composition of the electrolyte reaches the lowest freezing point possible for the electrolyte. The combination of DSC and electrochemical measurements allow for a better understanding of an electrolyte at low temperatures.

3. Improving sodium-based nonaqueous redox flow batteries

3.1 What is and why a nonaqueous redox flow battery (NARFB)

Redox flow batteries are a unique architecture of battery design that rely on fully dissolved redox couples stored in reservoirs to store energy. These redox couples replace the conventional solid cathode and anode and are referred to as the catholyte and anolyte. Redox flow batteries have been studied for decades ranging from aqueous to organic flow

batteries and incorporating dozens of newly discovered redox couples, cell designs, and issues[63]. The development of RFBs has been fueled by the need for an alternative for lithium-ion batteries for large scale energy storage or grid-scale energy storage. RFBs have many advantages of its LIB counterpart. Since the redox couples are dissolved in electrolyte rather than cast onto a current collector, the energy density is determined by the solubility of the redox couple. The overall energy density of a device can simply be increased by increasing the reservoir size of the capacity where traditional LIBs are capped due to space issues in terms of energy density within a single device[64]. Simply put, a single RFB can replace the need of many LIBs for the same energy needs.

The most common and well developed RFB is vanadium redox flow batteries (VRBs). VRBs are comprised of vanadium redox couples on either side and dissolved in water. VRBs have already been built and used in industry but are marred by low power density, low operating voltage windows (1.3V), and toxicity of redox couples[65].
The move to organic based or nonaqueous redox flow batteries (NARFBs) has been fueled by the potentially high energy density materials, larger voltage windows, and possibly safer alternatives to VRB and other aqueous redox flow batteries[66].

NARFBs designs range from using alkali metal anodes in metal-redox flow batteries, to sulfur containing catholytes, radical-based redox couples, and many more organic and inorganic chemistry[67–69]. In my work, I explored the use of sodium polysulfide as a catholyte for NARFBs paired with a radical anolyte, sodium biphenyl. This work showed promising results of a redox couple with long term stability, high

theoretical capacity, and very low costs. This work was ultimately finished by my collaborator, Dr. Ethan Self, but my contributions to the work are the long-term cycling of full redox flow batteries containing both sodium polysulfide and sodium biphenyl radical separated by a sodium beta alumina separator and showed a hundred cycles with little fade in capacity[70]. Moving forwards, the issues regarding NARFB development shifted to looking for cheaper alternatives to sodium beta alumina.

3.2 Membranes are a large bottleneck for NARFB development

As stated, sodium beta alumina was used in our study and many other sodium based NARFB studies. This is due to its high chemical stability, high ionic conductivity at room temperature, and ease of use. The issue is that this membrane and many other common RFB membranes are expensive and can constitute above 20% of the total cell fabrication costs.

Membranes for RFBs are typically divided into porous membranes or ion selective membranes. Porous membranes separate by size and allow for high ionic conductivity through the membrane and are typically cheaper. Many porous membranes are polymer-based but ceramics such as glass fiber mats are common in battery literature. The alternative is using ion selective membranes that separate based on relative charge difference between the membrane and species trying to pass through it. This typically lowers ionic conductivity but improves selectivity of the membrane. Selectivity is extremely important in RFBs. It is well known that the crossover of redox couples during cycling typically leads to irreversible loss in capacity and other forms of cell degradation.

Due to this, the use of ionic selective membranes in common place, but they also have issues.

Ionic selective membranes can come in many forms but are typically in either a ceramic or polymer film. Composites of ceramics and polymers exist as well. Ceramic films typically have higher chemical and mechanical stability but can suffer from extremely low ionic conductivity[64]. Polymer membranes have high ionic conductivity but suffer from swelling issues that lead to mechanical degradation and some polymer will react with the redox couples or organic solvent. Finding a good membrane can prove troublesome and studies have cited that fact that to fully gauge the usefulness of a redox couple and membrane must deny the crossover with the redox couple and allow high ionic conductivity. In Chapter Four, I explore using a Nafion membrane as a separator for sodium polysulfide based NARFBs and more detail will provide there.

3.3 Using $NaPF_6$ in 2EGDME as a possible alternative to membranes

Membrane-free approaches in RFBs are not unheard of but each rely on novel approaches to the issue of mitigating crossover. These novel methods have included unique cell geometries, and immiscible solvents for each redox couple[71]. One possible method is not mitigating crossover but inhibiting the reactions that occur due to crossover. $NaPF_6$ in 2EGDME has been shown in SIBs to form a stable SEI on the surface of sodium metal[25,72]. This stable SEI allows for hundreds of cycles without the loss of capacity or formation of dendrites. SEIs are known to block furth electrolyte

breakdown in LIBs and SIBs when properly formed. Using this knowledge, a stable electrolyte may be able to block reactions with redox couples as well.

CHAPTER I

ANION COORDINATION IMPROVES HIGH-TEMPERATURE PERFORMANCE AND STABILITY OF $NAPF_6$-BASED ELECTROLYTES FOR SUPERCAPACITORS

A version of this chapter was originally published by J. Landon Tyler, Robert L. Sacci, and Jagjit Nanda:

Tyler, J.L.; Sacci, R.L.; Nanda, J. Anion Coordination Improves High-Temperature Performance and Stability of NaPF6-Based Electrolytes for Supercapacitors. Energies 2021, 14, 4409. https://doi.org/10.3390/ en14154409

This work was primarily performed by me. All electrochemical and characterization techniques were performed by me. This includes experimental design and analysis work. Robert Sacci assisted in the analysis of the FTIR measurements and in the experimental design for those measurements. Jagjit Nanda was the primary investigator for this work.

Abstract

Electrolyte stability can be improved by incorporating complexing agents that bind key decomposition intermediates and slow down decomposition. We show that hexamethylphosphoramide (HMPA) extends both the thermal stability threshold of sodium hexafluorophosphate ($NaPF_6$) in dimethoxyethane (DME) electrolyte and the cycle life of double-layer capacitors. HMPA forms a stable complex with PF_5, an intermediate in PF_6 anion thermal degradation. Unbound, this intermediate leads to autocatalytic degradation of the electrolyte solution. The results of electrochemical

impedance spectroscopy (EIS) and galvanostatic cycling measurements show large changes in the cell without the presence of HMPA at higher temperatures (≥60 ◦C). Fourier transform infrared spectroscopy (FTIR) on the liquid and gas phase of the electrolyte shows without HMPA the formation of measurable amounts of PF_5 and HF. The complimentary results of these measurements proved the usefulness of using Lewis bases such as HMPA to inhibit the degradation of the electrolyte solution at elevated temperatures and potentially lead to improve cycle life of a nonaqueous capacitor. The results showed a large increase in capacitance retention during cycling (72% retention after 750,000 cycles). The results also provide evidence of major decomposition processes (0% capacitance retention after 100,000 cycles) that take place at higher temperatures without the additive of a thermal stability additive such as HMPA.

1. Introduction

Energy storage devices have taken on a monotony of various forms (fuel cells, capacitors, batteries, etc.) to satisfy numerous operating conditions: energy density, voltage windows, cycle rate, power density, high temperature ranges, et cetra[9,17,54,73,74]. Commercial supercapacitors or electric double-layer capacitors (EDLC) generally have lower energy densities but higher power densities compared to Li-ion batteries, 10 vs. 200 Wh kg^{-1}, and 104 vs. 102 W kg^{-1} [54,55,75–79] respectively. Unlike batteries, supercapacitors do not utilize the Faradaic redox process to store charge in the bulk of the materials; rather, they store charge along the electric double layer (surface) of pores

within high surface area electrode materials. Double-layer charging is fast, which enables supercapacitors to have excellent power (rate) performance and long cycle life (>106 cycles) at the cost of poor energy density. As such, EDLCs are used for cold start assists for generators and memory back-up, as well as to deliver high power for smart grids, transport, and aerospace applications[78–80]. Aqueous-based EDLC are limited to 1.2 V due to the electrochemical window of water. The maximum energy stored (W) within capacitors is directly related to the specific capacitance (C) and the voltage window of the system (V) as follows:

$$W = \frac{1}{2} CV^2 \quad (1)$$

Equation (1) suggests that increasing the working voltage of the electrolyte will dramatically improve the amount of stored energy. Nonaqueous EDLC electrolytes have been developed based on acetonitrile and propylene carbonate as solvent systems. These electrolytes were shown to increase energy stored, at the expense, however, of the power[55,77,81,82]. Clearly, successful development of new electrolyte compositions needs optimization of a number of materials, as well as electrochemical properties such as working potential window, cycling rate, compatible carbon and binder systems, and other factors. Operating temperature is also an important factor as some electrolytes are unstable at temperatures above 60 °C. This instability leads to the creation of byproducts that inevitably increase the effective series resistance (ESR), reduce the operating voltage and power, and may cause cell pressure build-up. Another major issue is the corrosion of the current collector (aluminum) at higher oxidation potential and instability of the binder

material, Teflon, at voltages 60 ºC). Based on these observations, we propose a simplistic pathway on how the HMPA–PF_5 complex inhibits the autocatalytic decomposition reaction as reported in other systems[45,53] and improves cycle life and performance.

2. Materials and Methods

Electrolyte preparation: Electrolytes were prepared in an argon-filled glovebox. Before mixing, DME and HMPA were dried over a 4A molecular sieve. $NaPF_6$ (98%, Sigma Aldrich) was dissolved into DME (battery grade, Mitsubishi Chemical Company) to give a 1 molal solution (1 mol $NaPF_6$/1 kg of DME). The electrolyte was stored over sodium to remove impurities for at least one week. HMPA (Sigma Aldrich) was added to the electrolyte solution prior to testing in specified amounts—typically 20% by weight of the solution. It is important to note that HMPA cannot be in the presence of sodium metal as it will violently react.

Electrode preparation: The carbon electrodes were prepared from ultrasonicated aqueous slurries containing Black Pearls 2000 (BP2000, Cabot Corporation, Boston, MA, USA, BET surface area: around 1460 m^2/g) with carboxymethyl cellulose (CMC, Sigma Aldrich, St. Louis, MO, USA, molecular weight 700,000) as a binder. The electrode slurry was made by tape casting 85% BP2000 and 15% CMC onto an aluminum current collector. The electrodes were dried at 120°C under vacuum. The weight balance between the two electrodes is 1 to 1. Electrochemical measurements: Two electrode button cells (316 L stainless steel, CR2032, Hohsen Corp., Osaka, Japan) containing two carbon electrodes and a Celgard separator (2325) were used for all measurements. All impedance

measurements were made in the frequency range of 20 kHz to 10 mHz and acquired using Bio-Logic instruments (VSP3). The tests were performed at elevated temperatures and were controlled in a Cincinnati Sub Zero temperature chamber. Galvanic cycling measurements were performed between 0 and 1 V or 3 V at 5 mA using Bio-Logic instruments (VSP3). Cyclic voltammetry was performed at 10 mV/s.

Characterization: The infrared spectroscopy spectra of the solution was measured using a diamond attenuated total reflection accessory (ATR) attached to a Bruker ALPHA FTIR spectrometer within an argon-filled glovebox. Gas-phase FTIR (Cary 680 FTIR, Agilent Technologies, Santa Clara, CA, USA) spectra were measured every 3 min over 15 h inside a gas cell specifically made for studying gaseous products without interference from the ambient atmosphere. The cell was purged with helium and then sealed from the environment using Viton gaskets and KBr windows. The cell was sealed with KBr windows and wrapped in a heating coil and heated to 85 °C.

3. Results and Discussion

Cyclic voltammetry was performed to establish the electrochemical stability window of the electrolyte. Figure 9a,b shows that the voltage window is much smaller in the presence of HMPA of around 2.5 V (green curve, Figure 9b) versus the 3 V of the HMPA free electrolyte 2.8 V (purple curve, Figure 9a). Though the voltage window is lower, cycling at 80 ºC at both 1V and 3V show a remarkable difference in cycling performance. Without HMPA, the capacitance of the cell quickly drops from around 50 to ~0 F/g, which can be corroborated by the EIS measurements taken after 5000 cycles,

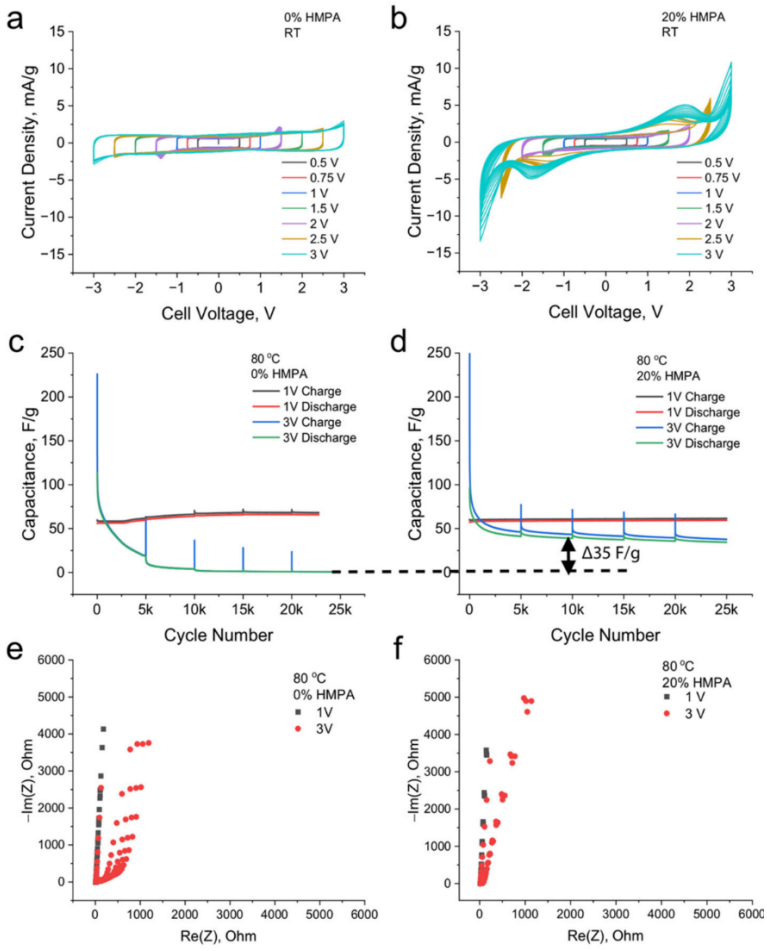

Figure 9: The cyclic voltammetry of 1m NaPF6 without HMPA (a) and with HMPA (b). The galvanostatic cycling measurements of 1m NaPF6 in DME without HMPA (c) and with HMPA (d) at 5 mA at 80 ◦C. The spike in capacitance is an artifact from performing EIS at OCV before every 5000 cycles and normalizes after 500 cycles. The Nyquist plots of cells were taken every 5000 cycles without HMPA (e) and with HMPA (f).

An increase of around 40 F/g of stable cycling can be observed with the addition of HMPA at 80 ◦C and cycling at 3 V. Which show significant increase in cell resistance (7 to 150 Ω at the end of the semicircle). We attribute these changes to electrolyte breakdown and the passivation of the carbon surface. A similar effect on high-voltage, high-temperature cycling is seen in the HMPA-bearing electrolyte— specifically, the capacitance decays from around 50 to 35 F/g after 25,000 cycles. This shows that in addition to impeding electrolyte decomposition at 80 ◦C, HMPA limits the destructive effect of high-voltage cycling. The impedance measurements in Figure 9e,f suggest that HMPA prevents surface passivation as the cell impedance (the semicircle in the Nyquist plots) growth is much slower (50 Ω) than without HMPA (150 Ω). Given that cycling at 3 V induces electrochemical degradation, all measurements beyond this point were performed at 1 V and focus solely on the thermal chemical degradation of the electrolyte.

EIS measurements were performed to verify ideal capacitive behavior in the cells for this study. The low frequency region shown in Nyquist plots should be parallel with the imaginary axis for an ideal capacitor[56,81]. Deviation from this ideality can be attributed to surface roughness, adsorption processes, and side reactions with the electrolyte[83]. With that said, near-ideal capacitive behavior in the EIS measurements was found when the cell voltage was kept between 0 and 1 V with and without HMPA— Figure 10a,b. The figures also show that the addition of HMPA did not affect the room temperature impedance except in small deviation of capacitance, though ideal capacitive

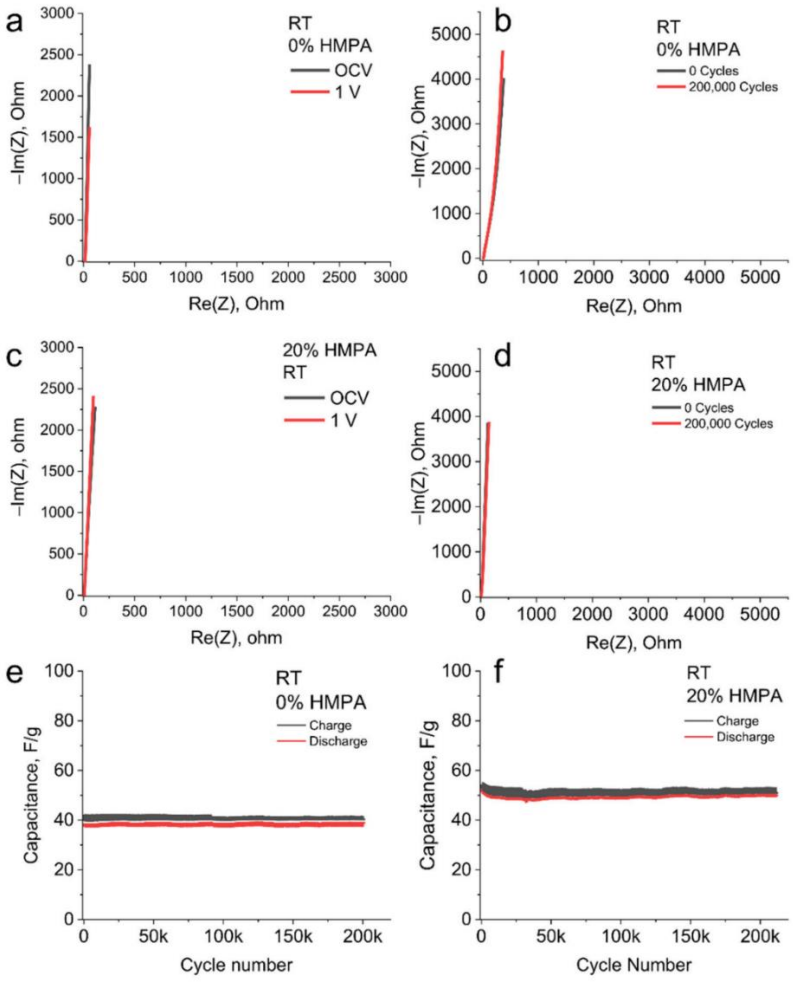

Figure 10: Nyquist plot without (a) and with HMPA (b) at room temperature. EIS measurements taken during galvanostatic cycling without (c) and with HMPA (d). Galvanic cycling capacitance vs. cycling number plots without (e) and with (f) HMPA.

behavior was observed. Room temperature galvanostatic cycling was performed to measure the cycling performance of cells containing 0% and 20% HMPA by weight.

During cycling, the EIS measurements performed every 1000 cycles show no change in capacitive behavior at well over 200,000 cycles—see Figure 10c,d. The specific capacitance is retained with a 99% retention over 200,000 cycles as shown in Figure 10e,f. This provided evidence that the addition of HMPA does not cause a detrimental effect on the cycling performance of the electrolyte.

The impedance of the cells was measured periodically during cycling (every 1000 cycles) to track changes in the capacitive behavior of the cell. The cells underwent testing at 80 ºC after being equilibrated for at least 1 h. The cells were then cycled between 0 and 1 V, while an impedance measurement was taken every 5000 cycles. Without HMPA, a noticeable growth in a semicircle in the high-frequency domain indicates a possible passivation of the electrode surface. This would lead to a decrease in capacitance while cycling, which can be observed in Figure 11b. The cell is essentially dead after 60,000 cycles after a quick decrease in capacitance. The cell continued cycling for 1,000,000 cycles without any change in capacitance, but a larger growth in passivation on the surface. The addition of HMPA lead to stable cycling over 739,000 cycles at 80 ºC—see Figure 11c,d. The EIS measurements also showed no significant change in impedance during cycling. There was slight fading with each cycle, but this electrode and electrolyte composition was not optimized, as it falls outside the focus of this study.

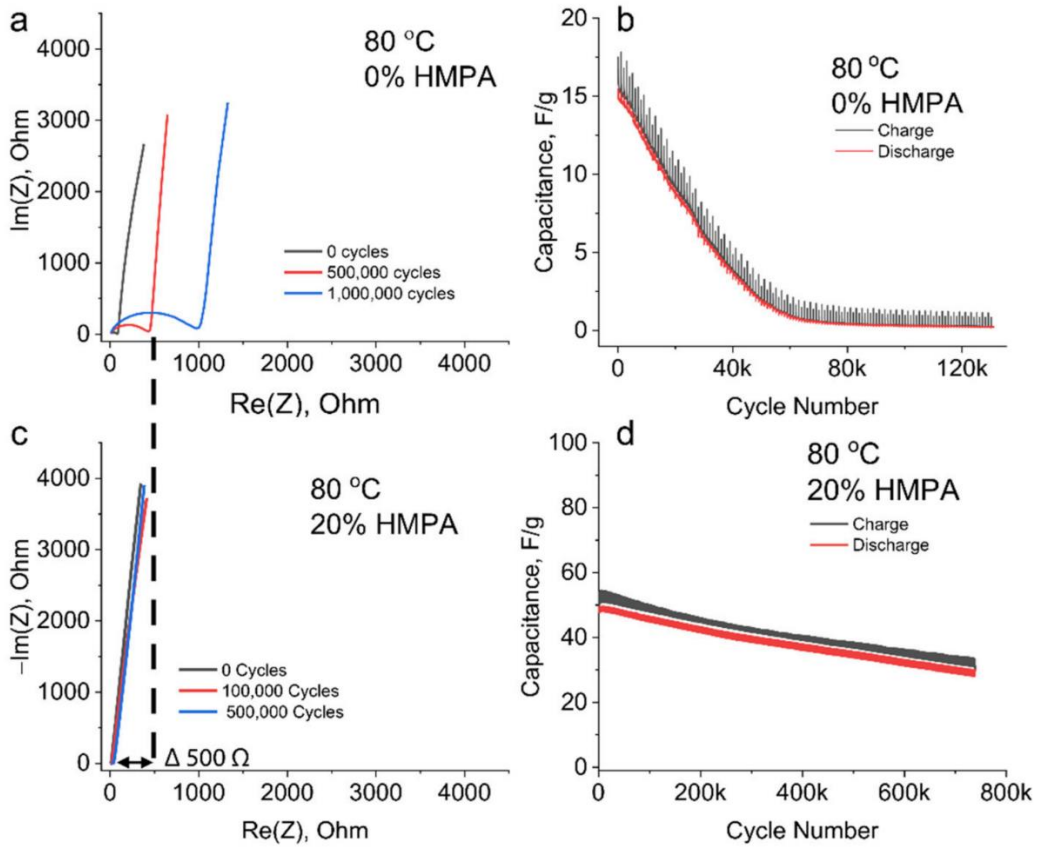

Figure 11: Electrochemical data of cells without HMPA at 80 ºC; (a) representative impedance data; (b) galvanic cycling data at 5 mA. There is clear evidence of cell degradation without the addition of HMPA. (c) Representative impedance data with 20% by wt. HMPA at 80 ºC; (d) galvanic cycling data (The spikes in the data are an artifact of how the data is taken. They occur after every EIS measurement). Note also that the initial capacitance of cells without HMPA at 80 °C vary due to unaccounted for degradation while equilibrating at 80 °C.

These results provided evidence that the addition of HMPA led to longer cycle life at elevated temperatures.

Visual evidence to the improved thermal stability brought on by HMPA. Here, the addition of 5% and 10% of HMPA keeps the electrolyte from turning dark brown after 40 h of heating at 85 ºC. The mechanism for increasing the thermal stability of PF_6-based electrolytes includes scavenging PF_5 or acidic byproducts. An equilibrium is suspected to develop between PF_6 − and PF_5 in the solution phase[53].

This equilibrium is disrupted, and the reaction shifts towards the formation of PF_5 at higher temperatures and begins the process of continual electrolyte degradation. In a typical lithium-ion battery electrolyte, PF_5 reacts with impurities found within the cell, including trace water in the electrolyte solution, surface impurities of the electrode, and the solvent of the electrolyte[53]. The plausible decomposition pathway for $NaPF_6$ in DME is shown in Figure 12. The reaction products are primarily a combination of hydrofluoric acid, POF_3, fluorine containing organic compounds, and carbon dioxide. The reaction is considered autocatalytic since PF_5 will also react with products from its own decomposition pathway as shown in Figure 12. The decomposition pathway shows a large combination of possible products that can be consumed to further the decomposition of the electrolyte. The decomposition products could also act as reactants for surface passivation of the carbon electrodes leading to the loss of capacitance. This phenomenon was measured in Figure 11a, which shows a large increase in resistance with continuous exposure to elevated temperatures.

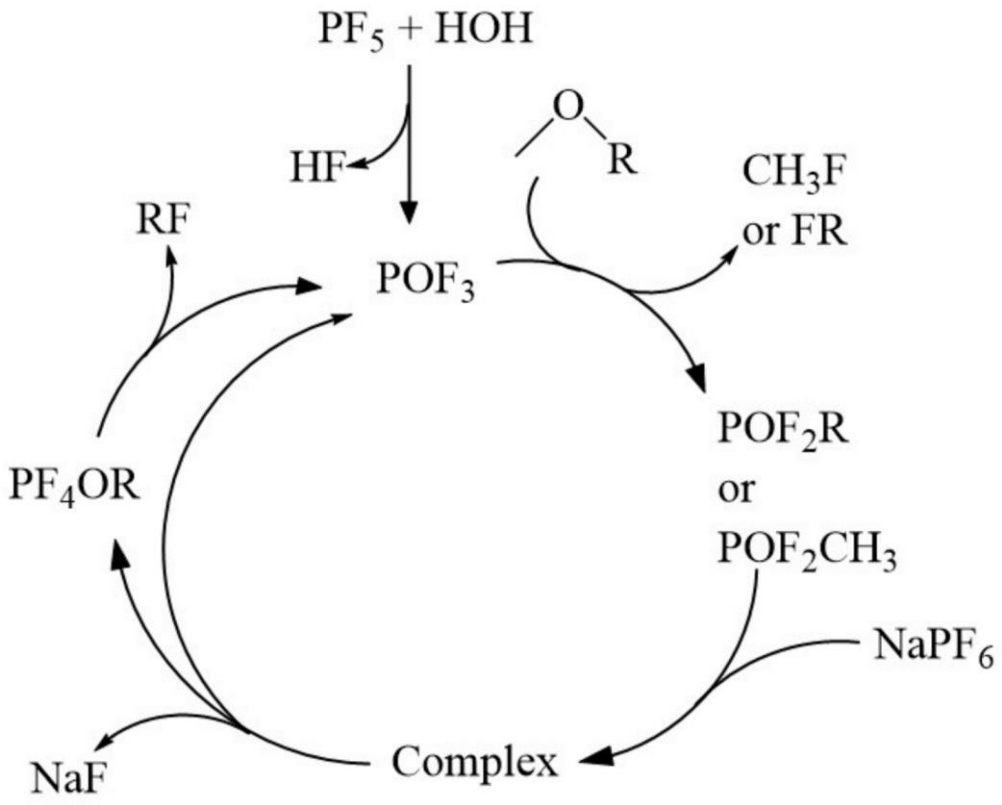

Figure 12: Possible autocatalytic decomposition pathway for $NaPF_6$ in DME without complexing agents

The reaction pathway also highlights that all components of the electrolyte solution are affected by the presence of PF_5. The more important factor is that as PF_5 reacts, it disrupts the equilibrium and results in more PF_5 forming and further degradation of the electrolyte solution in the cell.

On the contrary, HMPA binds with PF_5, as shown in Figure 13, and forms a highly stable complex. The kinetics of this complexation are thought to be rapid, as PF_5 is unable to induce the autocatalytic decomposition of PF_6^- and other electrolyte species. As with many sacrificial additives, there is a limit to the amount or quantity of HMPA in the electrolyte that can suppress the formation of PF_5. When all the HMPA in the system is utilized, $NaPF_6$ thermal degradation resumes[45]. The scope of the paper is not to optimize the necessary amount of HMPA for sodium supercapacitors, but to prove the concept of using a Lewis base such as HMPA as an additive for inhibiting the thermal degradation of $NaPF_6$.

FTIR was used to track the decomposition reactions within the electrolytes with and without HMPA added—see Figure 14. The peak at 807 cm^{-1} corresponds to the asymmetric P-F stretching band of the PF_6^- anion, and the peaks centered at about 1087 and 1110 cm^{-1} correspond with the C-O stretching of DME[29]. Signals from HMPA are at 740, 985, 1200, and 1295 cm^{-1}. The relative intensity between 807 and 1087 cm^{-1} drastically decreases after 24 h at 85 ºC without HMPA—see Figure 14a. This decrease indicates a decomposition of PF6. The same bands show little change when 20% HMPA

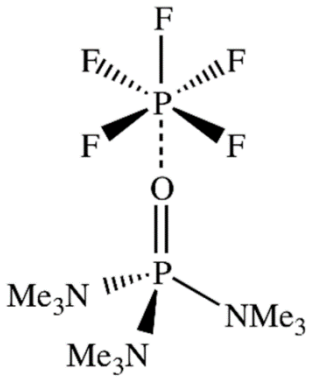

Figure 13: The complex structure between HMPA and PF_5 that may function to prevent thermal decomposition

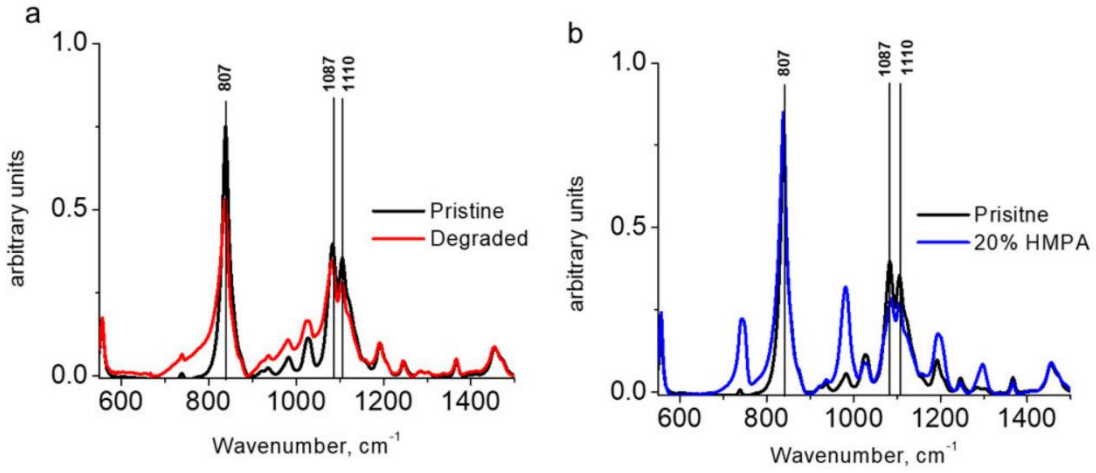

Figure 14: (a) FTIR spectra 1 M $NaPF_6$ in DME before and after decomposition at 85 ºC; (b) FTIR spectra of 1 m $NaPF_6$ in DME after exposure to 85 °C (compared to pristine 1 m $NaPF_6$ in DME). Liquid-phase FTIR shows changes in peak intensity of the PF_6 P-F stretch (807 cm^{-1}).

is present—see Figure 14b. This could be because PF_5 exists as a gas at room temperature.

To discern the formation of PF_5, FTIR was performed on the gases evolving from the electrolyte solution at 85 ºC—see Figure 15. After 7 h of exposure, new peaks at 480 and 735 cm^{-1} appear, which are attributed to the PF stretching bonds of PF_5[84]. Another notable feature is the generation and consumption of HF corresponding to the peaks between 3600–4000 cm^{-1}—see Figure 15b. After 7 h, these peaks begin to diminish which is representative of consumption due to the previously discussed decomposition pathway. Both HF and PF_5 are typical decomposition products of $LiPF_6$ in organic solvents[85,86].

Neither of these compounds are observed in the FTIR spectra for electrolyte solutions containing HMPA—see Figure 15c. The gas-phase FTIR provides evidence that without HMPA, the electrolyte solution degraded and formed PF_5 gas. The correlation of the lack of degradation of $NaPF_6$ in the liquid phase and the absence of the formation of PF_5 in the gas phase means that HMPA complexed with PF_5. This complexation led to inhibition of the degradation reaction and stability of the electrolyte at higher temperatures.

4. Conclusions

Electrochemical and infrared spectroscopy provided evidence that without HMPA, fluorophosphate-based electrolytes undergo rapid thermal degradation.

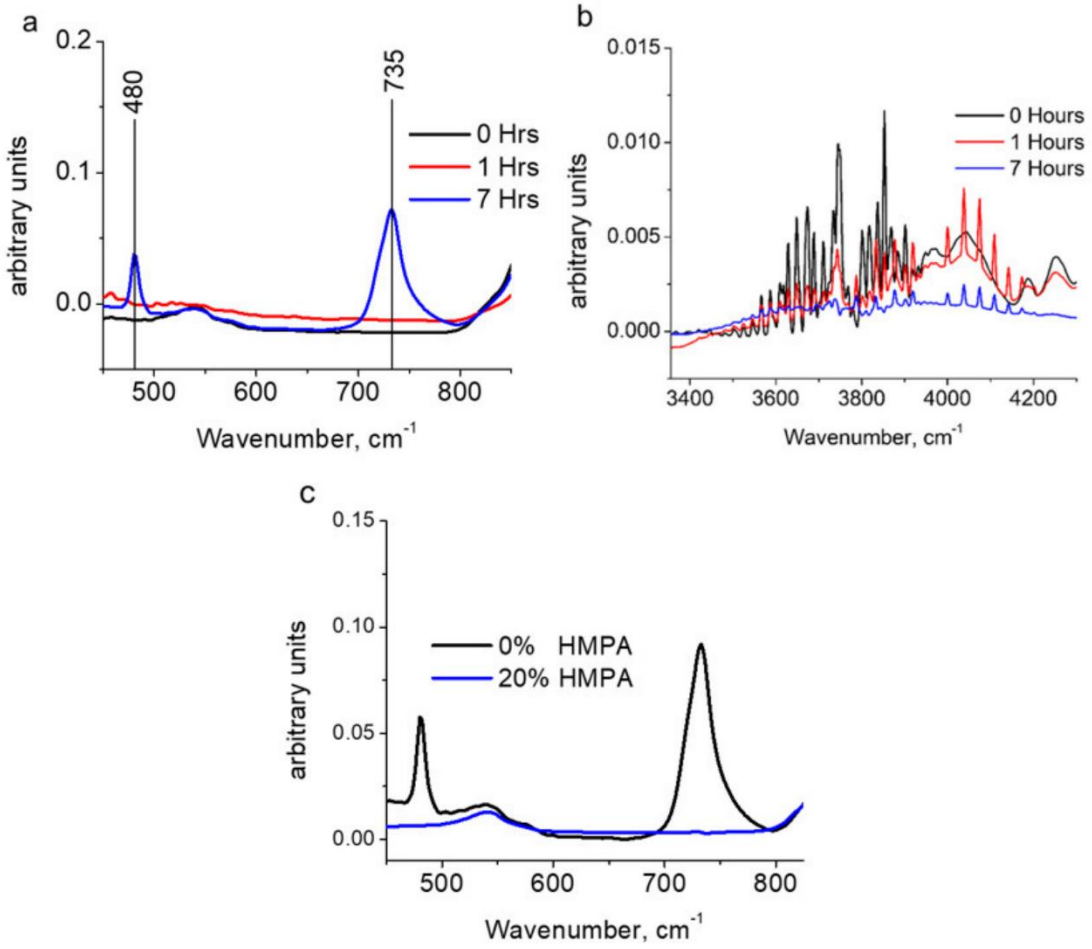

Figure 15. FTIR spectra of gas phase of 1 M $NaPF_6$ in DME at 85 ºC. Top spectra are without HMPA, with (a) highlighting the HF region, (b) highlighting the PF_5 region during degradation, and (c) comparing the effect of HMPA addition after 7 h. $NaPF_6$ will degrade into PF_5 and HMPA suppresses PF_5 formation in the gas phase.

FTIR results indicate that PF_6^- undergoes thermal breakdown into PF_5 and HF. With the addition of HMPA, EDLC cells retained their capacitive behavior and showed stable cycling performance at elevated temperatures. Here, no major changes in the FTIR spectra were observed. Our results support the notion that HMPA complexes with PF_5 in a similar manner as that previously hypothesized in Li-ion systems. Similar research could be performed pairing Lewis bases with other PF_6-based or Lewis acid anion salts for a myriad of applications and working temperatures. This provides one possible avenue for the development of PF_6-based supercapacitors for high-temperature applications.

CHAPTER II

ANION COORDINATION OF LEWIS BASES INHIBIT THERMAL DEGREDATION IN $NAPF_6$-BASED ELECTROLYTES

A version of this chapter is planned to be published by J. Landon Tyler, Robert Sacci, Josh Damron, and Jagjit Nanda.

Tyler, J.L.; Sacci, R.L.; Nanda, J. Anion Coordination Improves High-Temperature Performance and Stability of NaPF6-Based Electrolytes for Supercapacitors. Energies 2021, 14, 4409. https://doi.org/10.3390/ en14154409

This work was primarily performed by me. All electrochemical and characterization techniques were performed by me. This includes experimental design and analysis work. Josh Damron performed all NMR measurements and analysis of those results. Robert Sacci and Jagjit Nanda are primary investigators of this work.

Abstract

Thermal electrolyte stability is a known issue for PF_6-based electrolytes for LIBs. Lewis bases have been used in LIBs as additives to inhibit the thermal degradation pathway of PF_6 forming PF_5. $NaPF_6$ is a common electrolyte in SIBs and suffers from the same thermal instability issues as its lithium analogue. In this work, we explore using Lewis bases used in LIBs as thermal stability additives for $NaPF_6$ in DME. The long term cycling stability was increased with the addition of Lewis bases (TTFP, PPP, and THA) and was measured with galvanostatic cycling and EIS 80 ºC. The additives were also studied using NMR to track changes in the complexation and identify any new species forming as a result of additive addition.

1. Introduction

Lithium-ion batteries (LIB) are one of the most popular forms of energy storage for mobile applications such as electric vehicles and portable devices. Unfortunately, the rapid development and implementation of LIBs has resulted in resource scarcity for materials commonly used in these batteries[87]. A transition to a more abundant cation like sodium is necessary for the progression of the next generation of energy storage devices. The transition to sodium ion batteries (SIB) is not trivial as sodium ion battery material differ from their lithium analogue signficantly[3]. The cation difference leads to differences in solid electrolyte interface (SEI) formation, redox reactions of electrode materials, solvent interactions, and more[3]. This is also true for sodium ion electrolytes as additives commonly used to improve LIBs do not improve or are detrimental to SIBs. One example is the use of vinyl carbonate (VC) as an SEI promoter in LIBs. The use of VC in SIBs lead to unstable SEI formation and quick capacity fade[4,36]. Examples like these have become common place in the literature and has promoted the research of additives for SIB electrolytes.

The most common electrolyte for LIBs is lithium hexafluorophosphate ($LiPF_6$) in carbonate solvents[88]. The benefits of this electrolyte have also been adopted by SIBs which shows similar electrolyte and chemical properties as its lithium analogue. One common issue faced by PF_6-based electrolytes is the lack of thermal stability of the anion at higher temperatures (>60 °C). With the ever-growing demands of batteries, devices can be placed on conditions that are less than ideal for LIBs. Electrolyte additives have

been studied to halt the thermal degradation of PF_6 in LIBs. These additives are typically strong Lewis bases that complex with the decomposition product of PF_6, PF_5 which is a strong Lewis acid. The complex formed with PF_5 is considered a Lewis adduct and the stability of this adduct varies with each additive. This has been thoroughly explored in LIBs and in our previous work, we showed that hexamethylphosphoramide (HMPA) acts a thermal stability additive for $NaPF_6$ in dimethyl glycol ether (DME). Further exploration of the other additives from LIBs is necessary for the quick development of SIBs using $NaPF_6$ as an electrolyte. In this body of work, we will examine three different additives used in LIBs as possible thermal stability additives in SIBs using $NaPF_6$ in DME.

The three additives explored in this work are (pentafluorophenyl)-diphenylphosphine (PPP)[52], tris(2,2,2-trifluoroethyl)phosphite (TTFP)[89], and trihexylamine (THA)[90]. All three are Lewis bases of varying strength and have all been shown to increase the thermal stability of $LiPF_6$-based electrolytes in lithium-ion batteries. The addition of any of these additives improves the electrochemical performance of the electrolyte at elevated temperatures but to varying degrees of improvement. The degree of variation is discussed as each of these additives have different chemical properties that can affect the Lewis adduct that form in the electrolyte. To isolate the effects on thermal stability of this electrolyte, the electrochemical experiments are performed in a carbon electric double-layer supercapacitor framework.

This elevates the effects of sodium-based electrodes which introduce extra-complexity that can affect the overall performance and stability of the electrolyte itself.

2. Materials and methods

Electrochemical measurements: All electrochemical measurements were performed on symmetric coin cells (316 L stainless steel, CR2032, Hohsen Corp., Osaka, Japan) on VMP3 Biologic Potentiostats (#). The electrode slurries for the coin cells were 85% by wt BP2000 (#) and 15% carboxymethylcellulose (#) dispersed in water by probe ultrasonication for 10 minutes. The electrodes were sprayed coated on to aluminum current collectors to a loading of 1.1 mg/cm2then dried at 90°C. The electrodes were then punched and stored in an argon-filled glovebox. The electrolyte solution was 1 molal NaPF6(#) in DME (#) and stored under 4A molecular sieve (#) and sodium metal inside an argon-filled glovebox. The coin cells were fabricated in the same argon-filled glovebox. The galvanostatic cycling was performed at 5mA/cm2from 0 to 1V unless otherwise mentioned. For the elevated temperature experiments, coin cells were exposed to the elevated temperature one hour prior to measurement and maintain in a Cincinnati Sub-Zero temperature chamber (#). Electrochemical impedance spectroscopy (EIS) was performed at both room temperature and elevated temperatures from 20kHz to 100 mHz.

NMR characterization technique: All NMR was collected on Avance III 400 MHz NMR spectrometer using a single pulse sequence with 1H decoupling in the heteronuclear cases. 19F was collected with 8 scans and a 10s recycle delay, 31P was collected with 8 scans and a 4s recycle delay, and 1H was collected with 16 scans and a 40s recycle delay.

The samples were placed in NMR tubes and allowed to degrade at 50 °C for seven days. The samples consist of 1m $NaPF_6$ in deuterated tetrahydrofuran (d-THF) with 10% TTFP, PPP, or THA.

3. Results and Discussion

Galvanostatic cycling was performed at 80 °C to gauge the effectiveness of each thermal stability additive. The cycling performance for 1m $NaPF_6$ in DME without additives is shown in Figure 16a. The capacitance quickly begins to fade during cycling and reaches zero capacitance after 100k cycles. The same measurement was taken at room temperature to isolate the effects of elevated temperatures during cycling as shown in Figure 16b. The capacitance is retained over the course of 100k cycles at room temperature at ~ 99% retention. EIS was taken periodically during cycling and shows a rapid growth in equivalent series resistance (ESR) of ~100 Ohms at 80 ºC shown in Figure 16c. As compared the same measurements taken at room temperature, little change in ESR was measured. The loss in capacitance and growth in ESR can attributed to degradation of electrolyte that is expected 80 °C. Electrolyte decomposition is known to increase ESR and decrease capacitance from passivation of the electrode surface caused by the decomposition products. These measurements confirm that 1m $NaPF_6$ in DME is not stable at elevated temperatures. Next, three additives were implemented as possible thermal stability additives for 1m $NaPF_6$ in DME. Galvanostatic cycling and EIS were used to gauge the effectiveness of each additive at improving thermal stability as

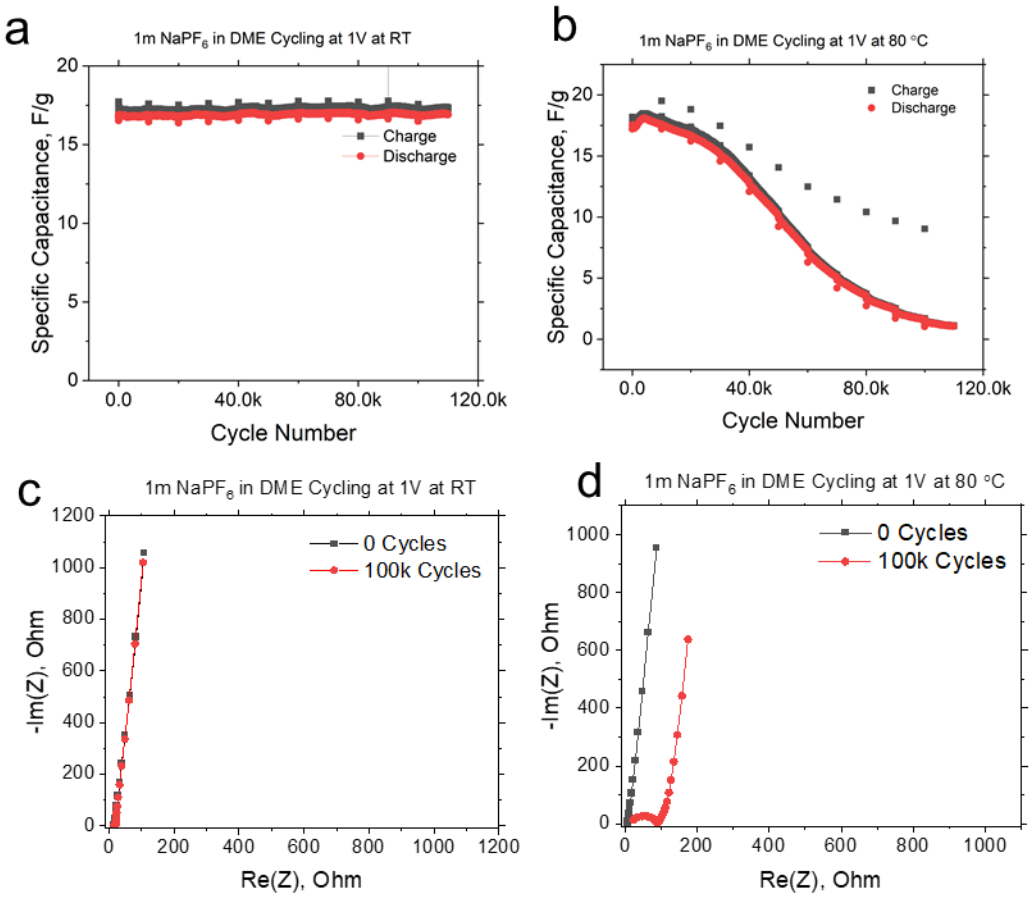

Figure 16: (a) The galvanostatic cycling of a 1m $NaPF_6$ in DME supercapacitor at (a) room temperature and (b) 80 °C. The EIS measurements taken before cycling and after 100k cycles at room temperature (c) and 80 °C (d).

show in Figure 17. TTFP shows the greatest cycling stability with as high as 99% capacitance retention after 100k cycles at 80 °C. THA shows the second best with 90% capacitance retention and PPP with only 70% retention. All three improve the 0% capacitance retention after 100k cycles of pure 1m $NaPF_6$ in DME. The increase in ESR for TTFP and THA are negligible while the PPP seen a shift in 25 Ohms over the course of 100k cycles. The difference in capacitance retention can be attributed to the Lewis basicity of each additive. PPP is known to be a weak Lewis base while TTFP and THA are strong Lewis bases. In similar studies performed in LIBs, the strength of the Lewis base affects the strength of the complexation with weaker complexes typically leading to larger losses in capacity over time. TTFP could also have the largest capacitance retention due to it being a softer Lewis base than THA. As PF_5 is a soft Lewis acid, it is expected that interactions with a strong soft Lewis base such as TTFP would give the most stable Lewis adduct. Gauging the strength of these complexations can be performed in several ways. Gutmann donor number can be measured using calorimetry which can be used a reference for comparing Lewis basicity. Though, this method has its limitations as Lewis acid-base interactions are difficult to predict and rely heavily on the two substances being studied.

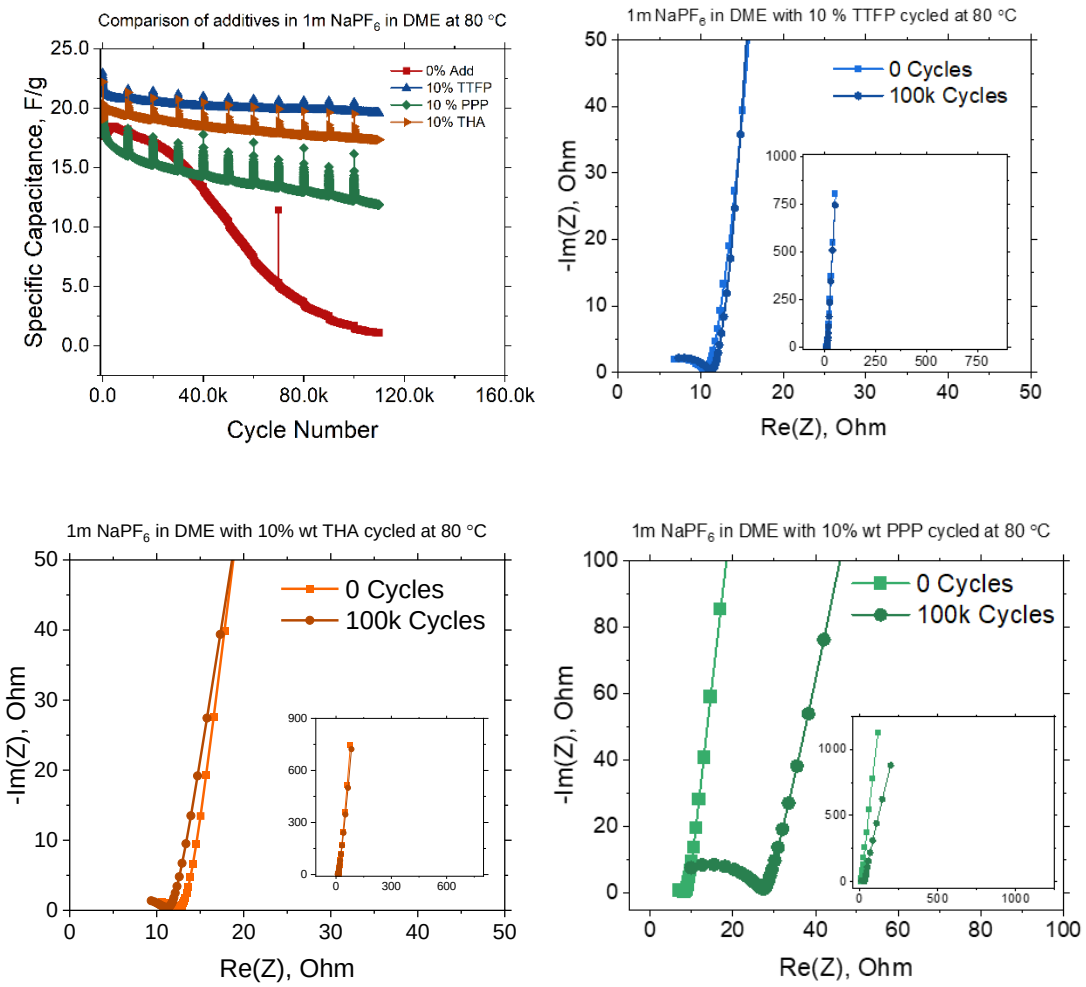

Figure 17: Galvanostatic cycling of supercapacitors from 0 to 1V with 1m $NaPF_6$ and 10% by weight TTFP, PPP, or THA at 80 °C. The EIS of supercapacitors cycled 0 times and 100k times at 80 °C containing 10% wt TTFP (b), THA (c), or PPP (d).

NMR has commonly been employed to both identify degradation products in the electrolyte and identify chemical complexes that form in the electrolyte. NMR measurements was performed on electrolyte containing 1m $NaPF_6$ in deuterated tetrahydrofuran containing either no additive, 10% wt TTFP, 10% wt PPP, or 10% THA. The resulting identification of peaks are found in Table 1. The electrolytes were both measured pristine with no exposure to elevated temperatures and after being exposed to 50 °C for seven days. $NaPF_6$ shows distinct NMR features in ^{13}F and ^{31}P NMR as a doublet at -80 ppm for ^{19}F NMR and a septet at -142 ppm for ^{31}P NMR in Figure 18 and 20. After exposure, new peaks are measured that can be attributed to electrolyte degradation products namely POF_3, a common decomposition product of PF_5 in carbonate-based electrolytes shown in Figure 18b,d. Theses degradation products are difficult to predict and are different for each solvent used, but degradation products containing a fluorine and/or phosphorous bond can be expected. The peaks typically occur at lower chemical shifts than the peaks for $NaPF_6$. After seven days of being exposed to 50ºC, a new doublet at a lower chemical shift (-89 ppm) than $NaPF_6$ was measured were measured. These can be attributed to either POF_3 or $OPF_2(OH)$. In this work, it will be described as POF(R) as the specific product is not the focus of this work.

In the samples containing, TTFP one new features in the ^{19}F NMR at -62.5 ppm after 7 days of exposure to 50 ºC. One feature is also measured at 5.98 ppm in the ^{31}P NMR as shown in Figure 19c. These features do not appear in the solutions containing

Table 1: ^{19}F and ^{31}P NMR values for $NaPF_6$ in d-THF solutions containing additives

Species	*^{19}F ppm,*	*^{31}P ppm*
PF_6	-80, d	-142, sept,
POF(R)	-89, d	-18.8, d, -8.3, d
TTFP	-80.5, s, -82.2, s	-3.8, s, -7.7, d
PPP	-145, d	-24.9, s
THA	-	-
TTFP Complex	-62.5, d	5.98, d
PPP Complex	-133, d, -167, s	-
THA Complex	-	-

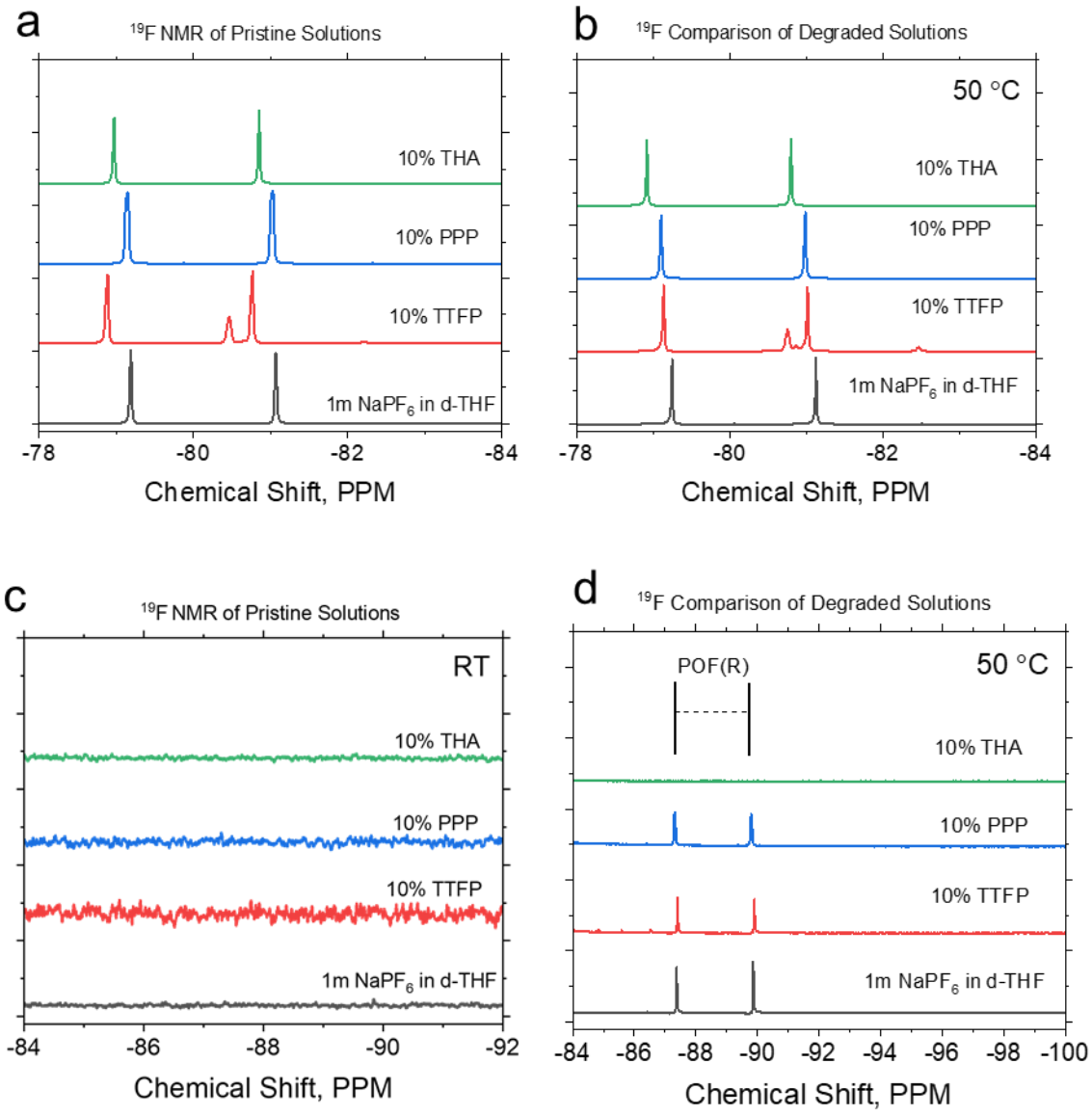

Figure 18: ^{13}F NMR of 1m $NaPF_6$ in d-THF containing no additive, 10% wt TTFP, 10% PPP, or 10% wt THA (a,c) pristine and (b,d) after seven days of exposure at 50 °C.

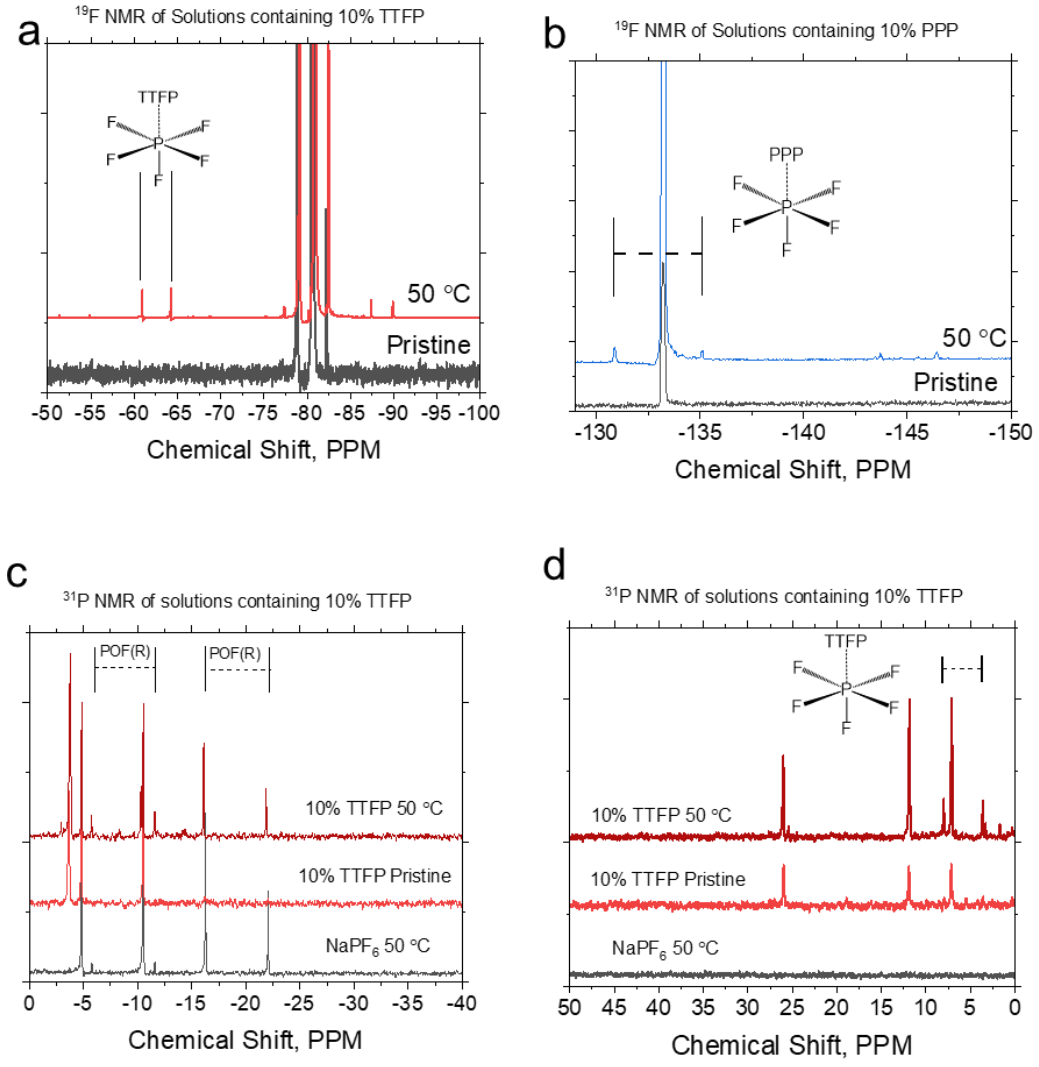

Figure 19: The ^{19}F or ^{31}P NMR spectras of solutions containing 10% TTFP in 1m $NaPF_6$ in d-THF (a, c, and d) or 10% PPP (b). a, c, and d highlight peaks that can be attributed to possible complexes of TTFP with PF_5. b highlights newly formed peaks that can be attributed to possible complexation with PF_5.

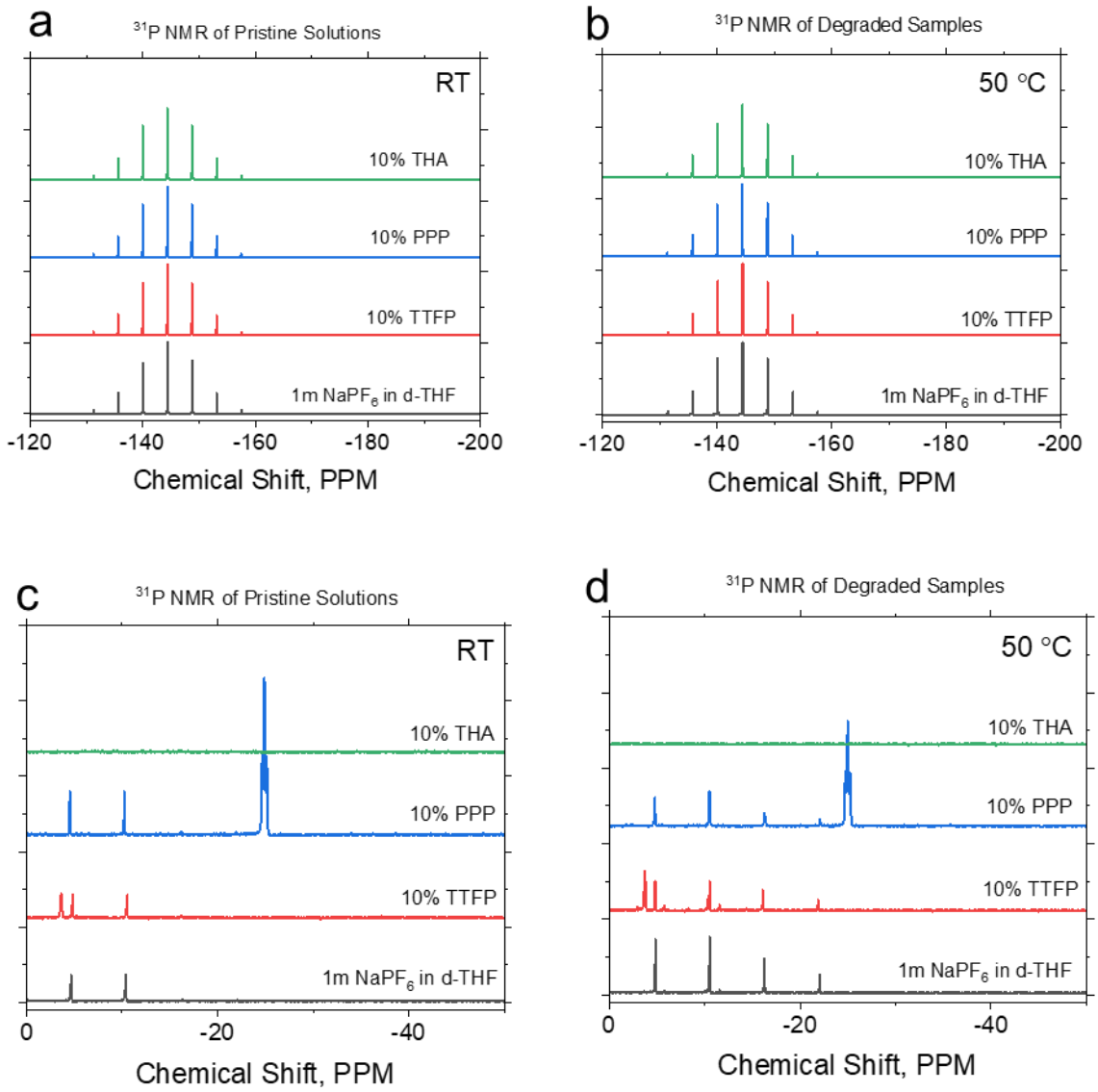

Figure 20: ^{31}P NMR spectrums of 1m $NaPF_6$ in d-THF containing no additive, 10% wt TTFP, 10% wt PPP, or 10% wt THA (a,c) pristine and (b,d) after exposure to seven days at 50 °C.

only 1m $NaPF_6$ in DME and are not attributed to the measured peaks of TTFP. These new peaks then can be attributed to a complex between PF_5 and TTFP. For samples containing, PPP many new features form between -120 and -160ppm, but the most prominent features being the doublet at -133 ppm and the singlet at -167 ppm as shown in Figure 19b. Neither of these features are present in the 1m $NaPF_6$ in DME solutions and are attributed to complexes between PF_5 and PPP. THA interestingly shows no new features in either the ^{19}F or ^{31}P NMR. Proton NMR was also performed in Figure 21, but no useful information for the formation of complexes was ascertained.

The strength of these complexes is difficult to gauge in a two-point comparison and in similar studies, it is necessary to take NMR measurements over the course of months to truly gauge the effectiveness of the complexation. Other studies focus on the formation of hydrofluoric acid. No measurable amount of HF was detected in any of the samples measured. A more accurate way to gauge the Lewis basicity of these different additives would be to measure the donor number through calorimetry or a more in-depth NMR approach. A matrix of Lewis bases with different donor number, donor atoms, hardness, and functional groups would be useful for measuring the deciding factor for PF_5 complexation and the highest thermal stability possible for PF_6-based electrolytes.

4. Conclusion

In this work, the addition of Lewis bases, TTFP, PPP, and THA, increased the thermal stability of $NaPF_6$ in DME at elevated temperatures. Without the addition of a

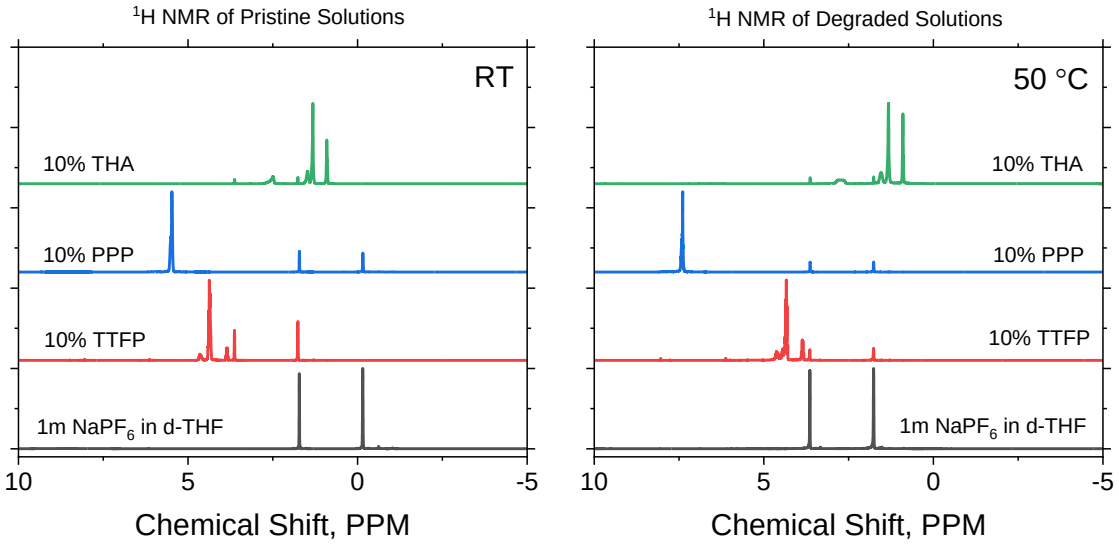

Figure 21: ^{1}H NMR of 1m $NaPF_6$ in d-THF containing no additive, 10% wt TTFP, 10% PPP, or 10% wt THA (left) pristine and (right) after seven days of exposure at 50 °C.

Lewis base, the electrolyte decomposes, and the capacitance retention is 0% after 100k cycles. The use of TTFP shows the greatest increase in capacitance retention of the solvents, but the larger conclusion is that like lithium-ion electrolytes, Lewis bases can be used with $NaPF_6$-based electrolytes to increase thermal stability of the electrolyte. NMR of the solutions after exposure to elevated temperatures provide evidence of complexations with PF_5 with both TTFP and PPP. ^{19}F and ^{31}P NMR spectrums include peaks that indicate the presence of complexations with electrolytes containing TTFP and PPP. Following up this work with a more rigorous NMR approach could provide evidence of complexation in solutions containing THA as well.

CHAPTER III

COSOLVENTS ENABLE USE OF NATFSI IN ACN AT BELOW FREEZING TEMPERATURES

A version of this chapter is planned to be published by J. Landon Tyler, Robert L. Sacci, Xiamon and Jagjit Nanda:

This work was primarily performed by me. All electrochemical techniques were performed by me. This includes experimental design and analysis work. Robert Sacci assisted in the analysis of the electrochemical results. Xiamon performed DSC measurements and analysis. Jagjit Nanda was the primary investigator of this work.

Abstract

Low temperature applications are uniquely suited to supercapacitors due to a lack of kinetic limits typically found in batteries. In this work, we screen cosolvent with lower freezing points than acetonitrile to promote low temperature performance and lower the freezing point of the electrolyte. Through a combination of galvanostatic cycling, DSC, and EIS, NaTFSI in acetonitrile is shown to have a higher capacitance retention, lower ESR growth, and lower freezing point with the addition of acetone and chloroform.

1. Introduction

Modern batteries are rated to -20 °C due to the physical and kinetic constraints of the chemistries used to store energy within those cells. Supercapacitors are commonly studied to temperatures as low as -40 °C. With the development of spacecrafts, avionics, and even submersibles, the want for energy storage devices that can operate at extremely low temperatures has grown. Supercapacitors are uniquely suited to this endeavor as their

electrochemical process is not limited to the kinetics of faradaic redox reactions, but rather the movement of ions through the electrolyte and reorganization of those ions[60]. As mentioned, supercapacitors are commonly studied to temperatures far below batteries while maintaining high currents and quick cycling.

Acetonitrile has a known freezing point of around -40 ºC, but studies have shown that cosolvents with lower freezing points such as ethyl acetate can lower the freezing point of the electrolyte solution to -55 ºC[91]. Lower the freezing point alone is not enough. Maintaining a reasonable amount of capacitance at lower temperatures is also necessary for low temperature operations. Electrochemical performance of supercapacitors is gauged with a combination of DC cycling and EIS measurement as a function of temperature. Previous studies have shown that screening multiple solvents is an ideal way of determining which cosolvent prove useful for enabling low temperature operation in supercapacitors.

In this work, three cosolvents were screened to gauge improvements to low temperature performance of NaTFSI in ACN solution below – 40 ºC: acetone, chloroform, and dimethyl ether (DME). Acetone has been studied in both aqueous and organic systems as cosolvents. In aqueous electrolytes, the presence of acetone lowers the freezing and melting point of electrolytes. Also, in a similar LiTFSI in ACN electrolyte, the addition of acetone affected the conductivity by causing changes in the solvation structure. In a previous study performed by Martins et al, the addition of chloroform into LiTFSI in ACN promoted chemical diffusivity higher than that of the bulk electrolyte

without chloroform. An increase in the mobility of chemical species in solution could possibly promote a lower freezing point in the solution. DME is a common solvent for organic electrolytes. It is also commonly used a cosolvent as it promotes ionic conductivity and typically increases ionic conductivity of electrolytes. Through a combination of EIS and galvanostatic cycling, the low temperature performance of each of these cosolvents was measured.

2. Materials and methods

Electrochemical measurements: All measurements were performed in coin cells (316 L stainless steel, CR2032, Hohsen Corp., Osaka, Japan) containing two stainless steel spacers, wave spring, two symmetric carbon electrodes, and Celgard 2325 separator. The carbon electrodes were made by spray coating a slurry containing 85% BP2000 carbon (X) and 15% CMC (X) dispersed ultrasonically in distilled water. The slurry was cast onto an aluminum foil. The electrodes were then punched and dried at 90 °C under vacuum. The electrolyte solutions were prepared in an argon filled glovebox. The electrolytes were made by dissolving NaTFSI (X) in acetonitrile (ACN, X). The cosolvents: DME (99%, Mitsubishi), acetone (99%, Thermoscientific), and chloroform (99%, Thermoscientific) were added to a mole ratio of 1:10:1 of NaTFSI:ACN:Cosolvent. The coin cells were fabricated in an argon filled glovebox. The galvanostatic cycling was performed at 5mA from 0 to 1V using a VMP3 Biologic potentiostat. The EIS was performed from 20 kHz to 10 mHz on the same potentiostat. Temperature was maintained within a Tennie Temperature chamber.

Cyclic voltammetry was performed at 1, 2, 10, 20, 50, 100, 200, 500, and 1000 mV/s from -1 to 1 V three times.

DSC measurements: All DSC samples were sealed in aluminum DSC pans. The samples were cool at a rate of -20 °C/min to -85 °C from room temperature. The DSC measurements were performed using a Q100 DSC.

3. Results and Discussion

Freezing point of the various electrolyte solutions was measured using DSC. The DSC thermogram of each electrolyte is in Figure 22. NaTFSI shows eutectic features with two peaks at -43 ºC and -50 °C. This is not unexpected as LiTFSI and NaTFSI are known to form eutectic solutions with various solvents both in aqueous and organics[58]. The chloroform containing electrolyte shows a similar eutectic feature but at -50 ºC and -62 °C. The acetone containing electrolyte has a freezing point of -62 °C. The DME containing electrolyte has a freezing point of -59 ºC. The addition of any of these cosolvents lowered the freezing point of the NaTFSI ACN solution by at least 10 °C. The findings from the DSC for the freezing points and the heat release of each sample is in Table 2.

EIS and GC cycling were used to measure changes in capacitance and ESR. The cells were cycled a thousand times at each temperature step at 5mA/cm^2 from 0 to 1V and EIS was measured before and after each measurement. The resulting cycling performance was shown in Figure 23. NaTFSI:ACN and in the presence of any cosolvent

Table 2: Freezing points and heat release for electrolyte solutions containing NaTFSI in ACN with acetone, DME, or chloroform as a cosolvent.

Composition of electrolyte	*Freezing point of co-solvent (°C)*	*Freezing point of solution (°C)*	*Heat release (J/g)*
NaTFSI:ACN	NA	-50.67	65.08
NaTFSI:ACN:acetone	-95	-61.13	65.58
NaTFSI:ACN:DME	-65	-59.42	27.05
NaTFSI:ACN:CF	-63.5	-50.35	35.26

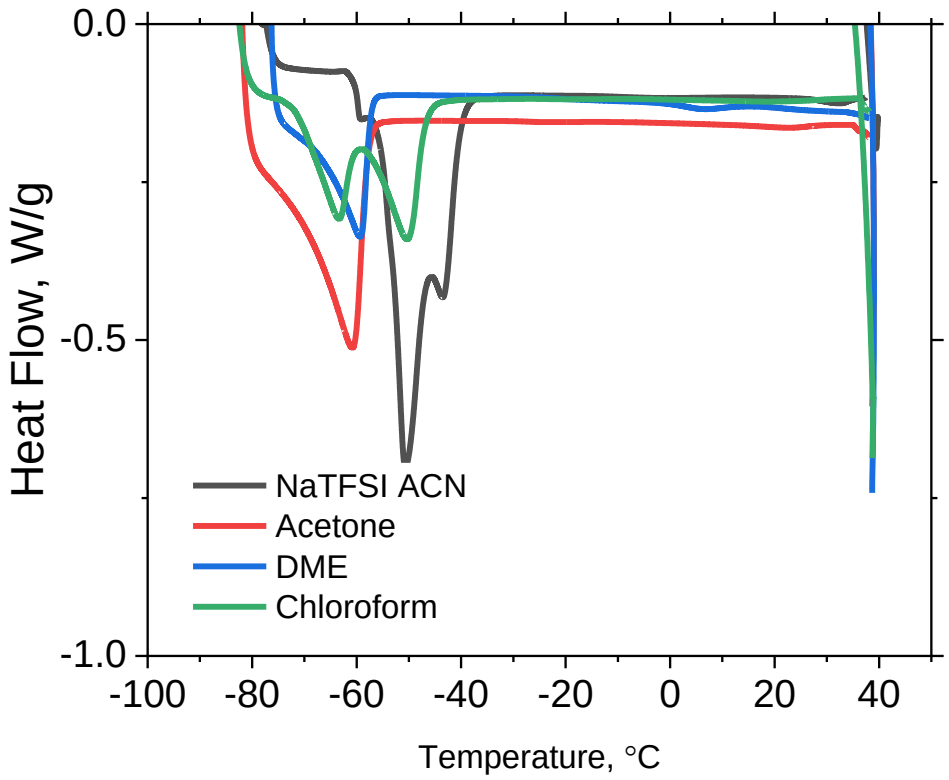

Figure 22: The DSC thermogram of electrolyte solutions of NaTFSI in ACN with or without acetone, DME, or chloroform.

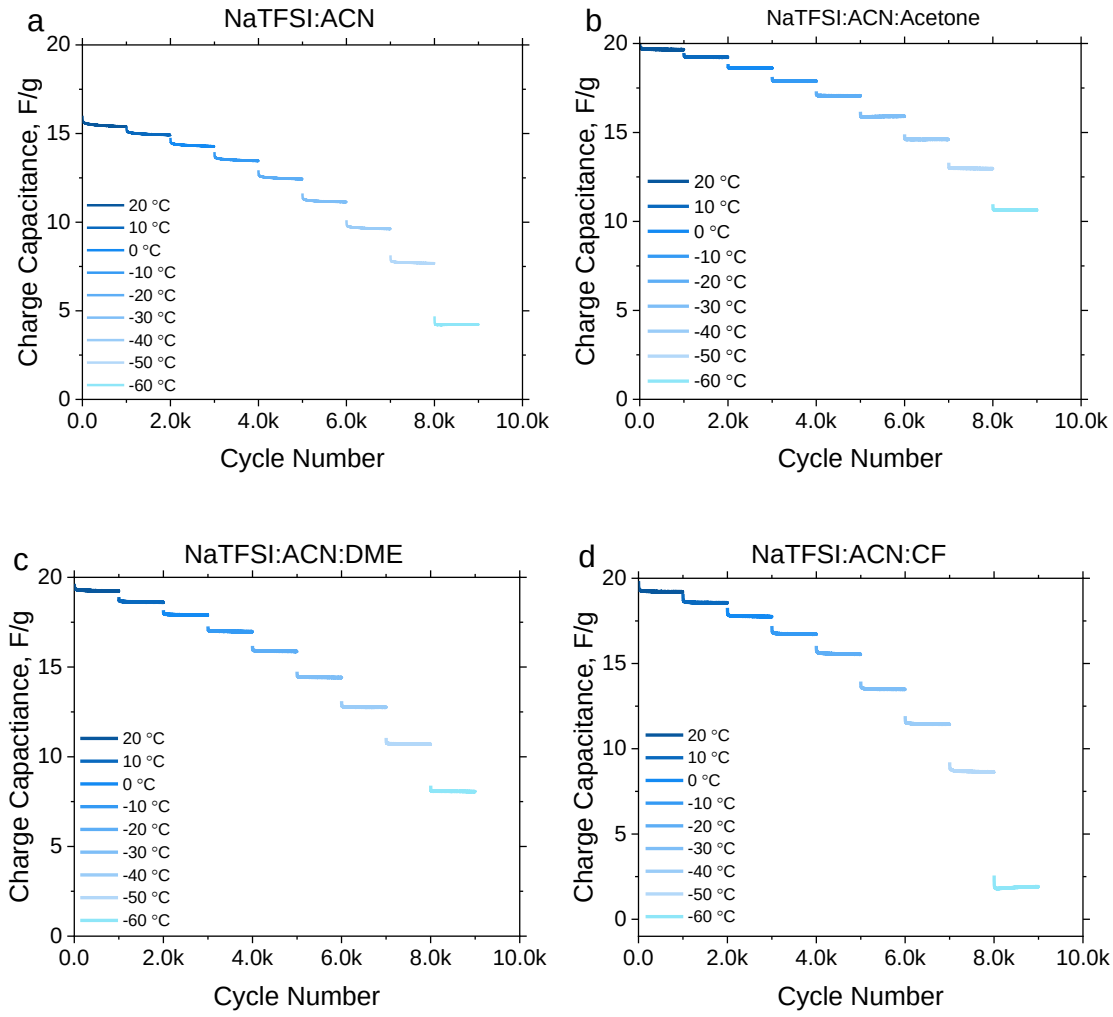

Figure 23: The galvanostatic cycling of supercapacitors containing (a) NaTFSI:ACN , (b) NaTFSI:ACN:Acetone, (c) NaTFSI:ACN:DME, and (d) NaTFSI:ACN:CF in a 1:10:1 molar ratio solution.

shows a steady decline in capacitance as the temperature decreases to -60 °C. The most pronounced decreases occurred after the expected freezing point of the NaTFSI:ACN and NaTFSI:ACN:CF as shown in Figure 23a and d. NaTFSI:ACN:DME and NaTFSI:ACN:Acetone have the largest capacitance retention below -50 ºC as shown in Figure 15b and c. On closer inspection, the amount of capacitance follows this order: acetone>DME>no cosolvent>chloroform as shown in Figure 24.

EIS measurements were also taken as a function of temperature and before and after cycling. The EIS measurements show no change in the EIS response as a function of cycling, but the ohmic resistance of each electrolyte grows as the temperature is decreased is shown in Figure 25. The effective conductivity of the electrolyte measured from extrapolating the ESR of the semicircle before the vertical tail (100 Hz) to -Im(Z)=0 is shown in Figure 26. As expected, the conductivity of the electrolyte decreases as the temperature decreases. The Arrhenius plot shown in Figure 26 also provides evidence that the electrolyte containing acetone is not affected by a temperature dependent process and retains linearity as low as – 60 °C. The ESR before the vertical tail of NaTFSI:ACN and NaTFSI:ACN:CF increase ESR by 50 and 75 Ohms respectively. NaTFSI:ACN:Acetone and NaTFSI:ACN:DME ESR increased by 35 Ohms. The EIS also shows a capacitance decrease like the capacitance measured during galvanostatic cycling.

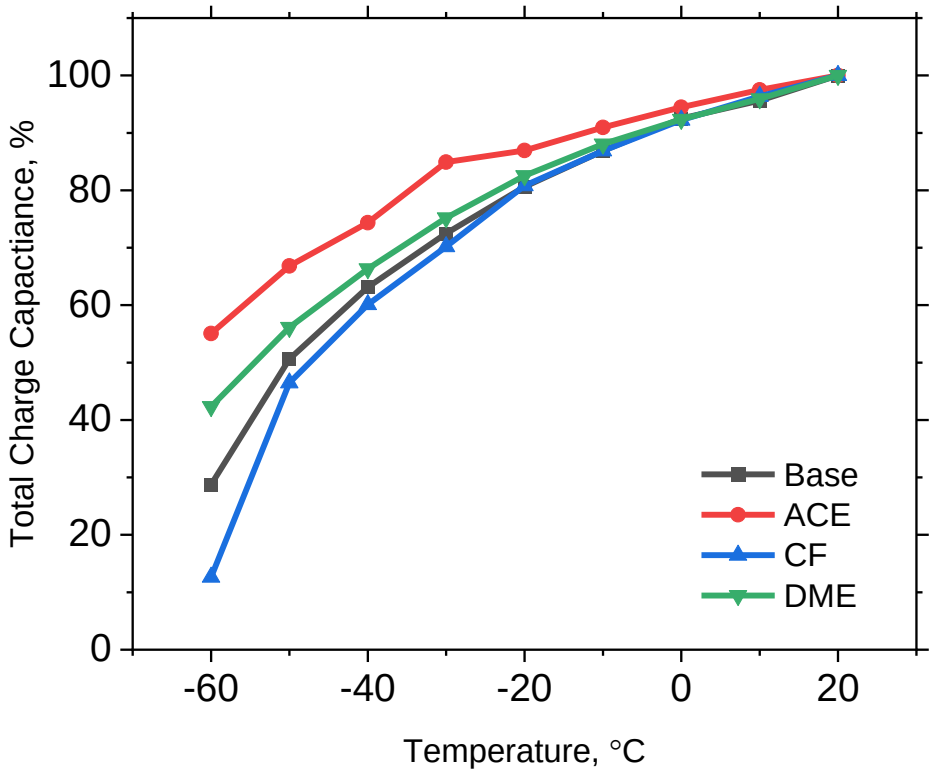

Figure 24: The % total charge capacitance as a function of time in cells containing NaTFSI in ACN with and without acetone, chloroform, and DME.

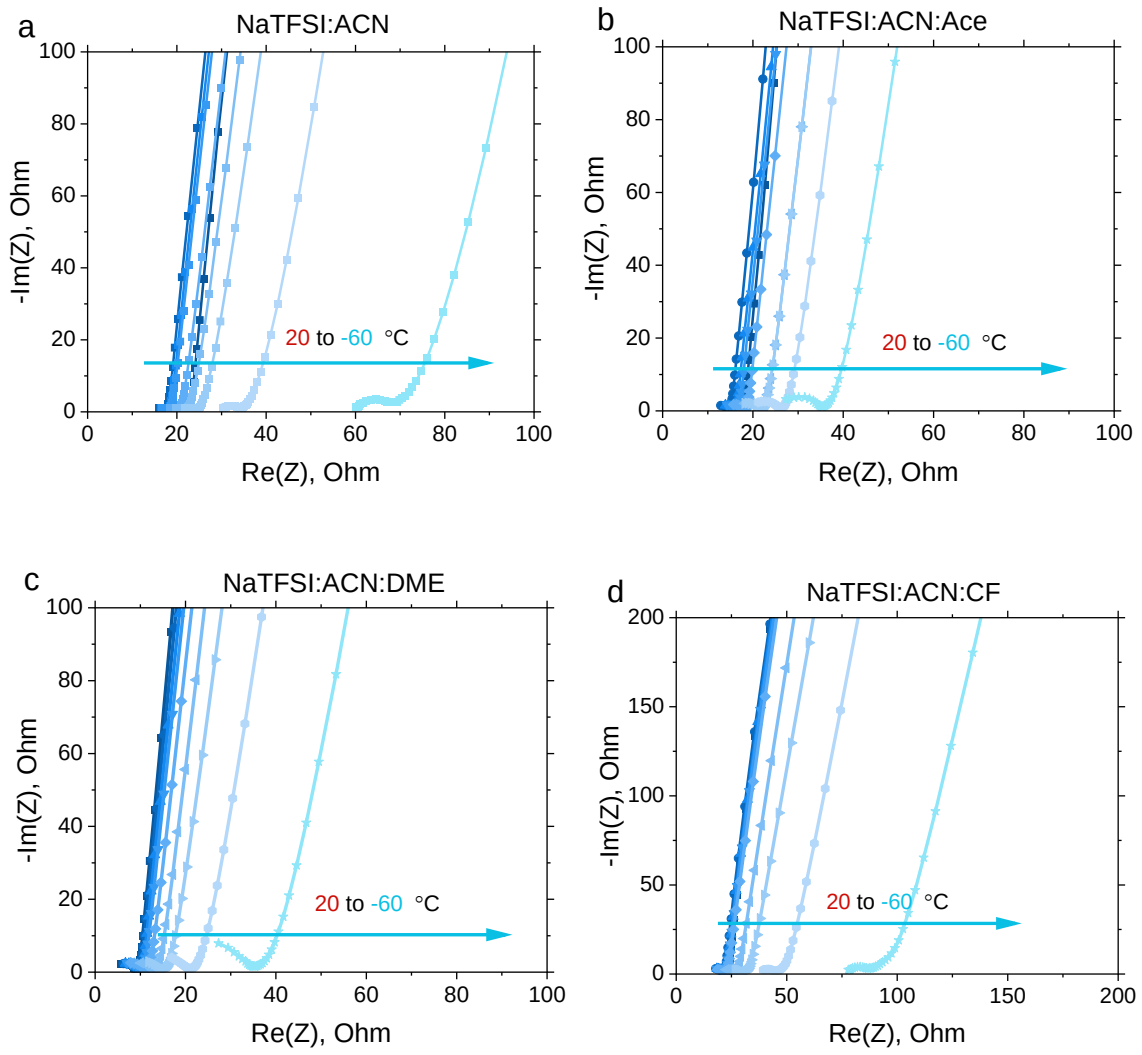

Figure 25: The EIS measurements of cells containing (a) NaTFSI in ACN with (b) acetone, (c) DME or (d) chloroform. The measurements were taken every 10 degrees and from 20 kHz to 10 mHz.

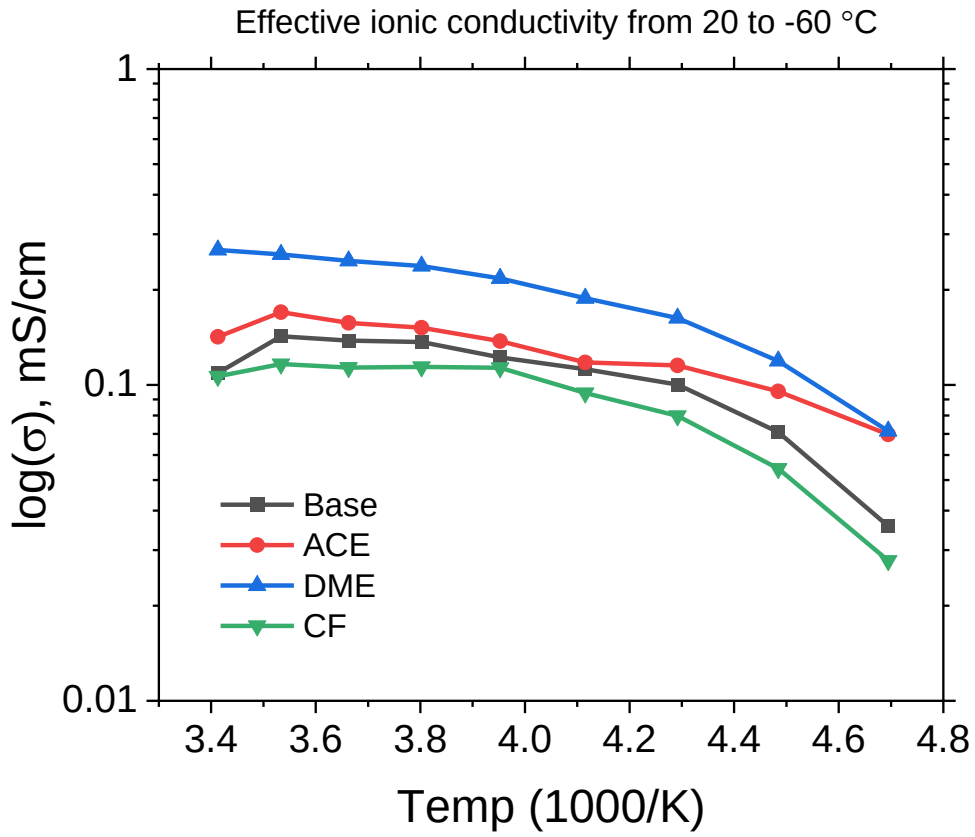

Figure 26: The effective ionic conductivity of the electrolyte equated from the EIS measurements taken in Figure 25.

Also, NaTFSI:ACN and NaTFSI:ACN:CF have a larger semicircle in the high frequency region of the EIS measurements that is absent in the other two electrolyte solutions. Elucidating these features could be possible with studying the interface of the electrode as a function of temperature in the presence of these electrolytes but falls out of the scope of this work.

Cyclic voltammetry was also performed as both a function of temperature and scan rate. The results from those measurements are presented in Figure 27. The CVs show that as you go lower in scan rate, much lower capacitance is capable of being obtained than at lower scan rates. Also, as you go to lower temperatures the overall capacitance at each scan rate is lower than at how higher temperatures. Comparing the different electrolyte combinations at 1 mV/s which produced the CVs with the highest capacitance shows a similar effect measured with the galvanostatic cycling mentioned earlier. The results are shown in Figure 28. As before, acetone and DME both show an improvement on capacitance retention as a function of temperature. Chloroform also decreases the capacitance retention similar to that of the cycling measurements. The combination of these results provided that these cosolvents play an important role in the low temperature performance of the electrolyte.

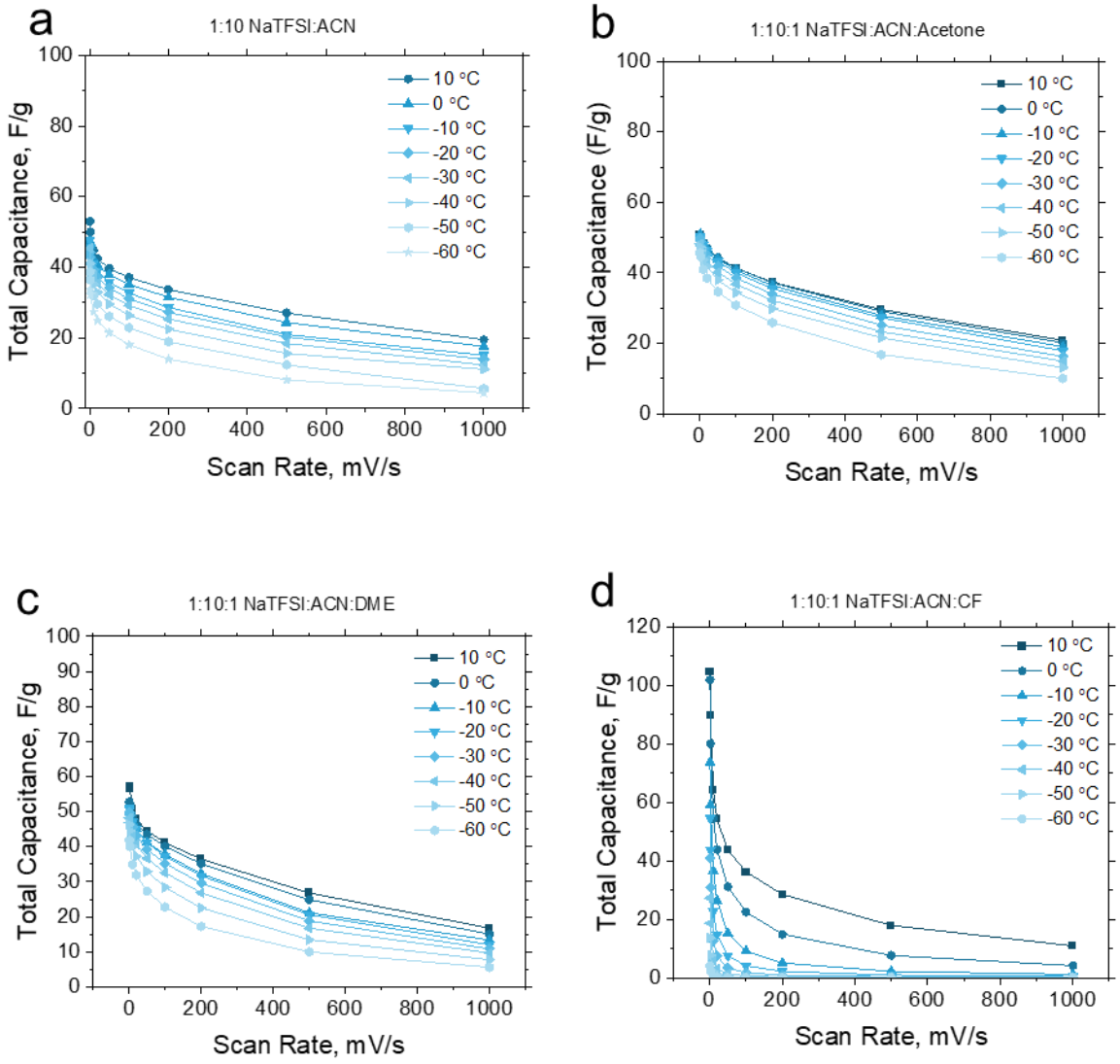

Figure 27: Total capacitance calculated from CV's taken from 1 mV/s to 1000 mV/s at 10 ºC to -60 ºC for cells containing (top left) NaTFSI in ACN and (top right) acetone, (lower left), DME, or (lower right) chloroform.

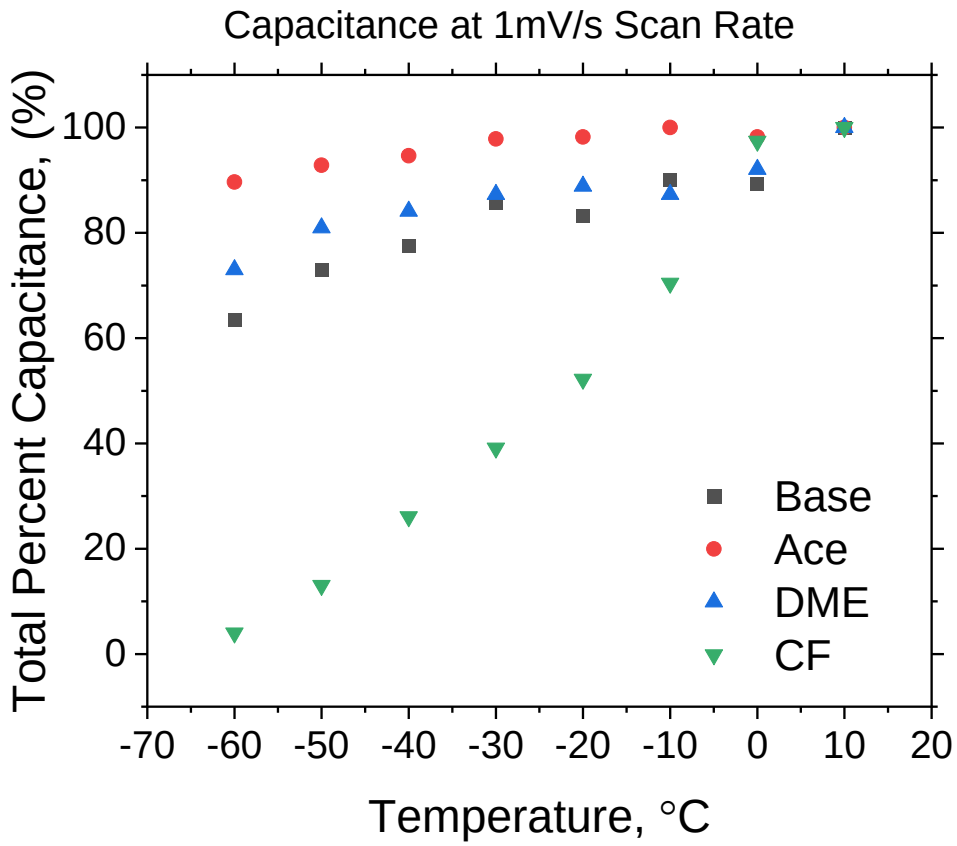

Figure 28: Total percent capacitance versus temperature for cells containing NaTFSI with acetone, DME, or chloroform. The capacitance is calculated from CVs taken at 1 mV/s.

Conclusion

These results provide evidence that NaTFSI in ACN with the addition of acetone or DME lowers the freezing point, increases the capacitance retention of the electrodes, and lowers the increase in ESR as a function of temperature. On the other hand, the addition of chloroform to this electrolyte results in detrimental side effects that cause no change in freezing point but lowers the capacitance retention and increases ESR as a function of temperature. Further screening of cosolvents is necessary to build a framework of chemicals that show benefits for low temperature applications. Also, exploration into the fundamental mechanisms resulting in these benefits would be key into understanding how to develop this field of research.

CHAPTER IV

NAFION AS AN EFFECTIVE INHIBITOR OF CROSSOVER OF SODIUM POLYSULFIDE IN NONAQUEOUS SODIUM REDOX FLOW BATTERIES.

A version of this chapter is planned to be published by J. Landon Tyler, Robert Sacci, Michelle Lehman, Ethan Self, and Jagjit Nanda

This work was primarily performed by me. All electrochemical and characterization techniques were performed by me with assistance from Ethan Self. This includes experimental design and analysis work. Robert Sacci assisted in the analysis of the UV-Vis measurements and in the experimental design for those measurements. Jagjit Nanda was the primary investigator for this work.

Abstract

We used a sodiated-Nafion membrane as separator in a sodium-sulfur nonaqueous redox flow battery to inhibit the crossover of sodium polysulfide. The capacity retention (75% after 50 cycles) and coulombic efficiency (99%) were significantly improved using a porous membrane that allowed for significant crossover (20% capacity retention after 45 cycles, 70% CE).

1. Introduction

Redox flow batteries (RFB) have been studied for decades as a possible solution to large scale energy storage[66,92,93]. RFBs offer a unique advantage, having their energy density decoupled from physical constraints, such as found in traditional batteries like lithium-ion[64,66]. In short, to increase the energy stored in a single RFB, the tanks storing redox active materials can be scaled up to meet specific energy demands. Furthermore,

nonaqueous redox flow batteries (NARFBs) offer key advantages to improve energy density: high specific capacity materials, large operating voltage windows (>3V), and flexible designs[92]. One NARFB of interest is metal redox flow batteries that utilize high energy density alkali metals like sodium and lithium as shown in Figure 29[94]. However, the realization of large scale NARFB requires solving key technological problems, such as developing membranes that inhibit crossover of active species while having high ionic conductivities and remaining stable against a myriad of chemicals and pressures[64,95,96]. Having all these metrics is difficult to implement into a single membrane. This fact is especially true for nonaqueous systems where organic solvents, and organic redox couples can be highly reactive towards polymeric membranes. In addition, detrimental effects such as passivation of current collectors, runaway side reactions, irreversible capacity loss, and short cycle life due to the crossover of neutral and charged electro-active species through the membrane being more pronounced and irreversible than in aqueous systems[97].

Membrane selection for NARFBs typically falls into two categories: ceramics and polymers. Low porosity ceramics offer zero crossover of active species, high conductivity ($1.67x10^{-3}$ S/cm at room temperature)[98] for Sodium Beta Alumina), and high chemical and mechanical stability but have difficult scalability and relatively high cost. For example, Na-β-Al_2O_3 has a current market price of $ 4,750 per kg vs that of a typical polymer membrane ($50 per kg of Nafion 117). Polymer membranes offer low cost, more easily produced, but typically allow for crossover of active species and degrade quickly in the presence of organic compounds[99,100].

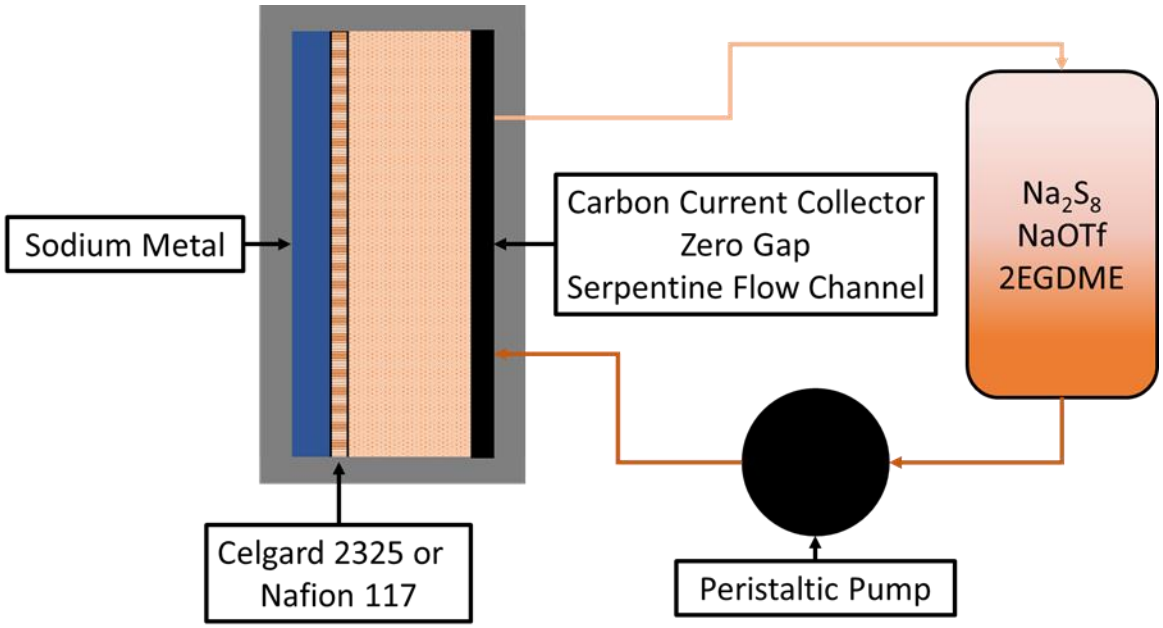

Figure 29: Schematic of a metal redox flow battery comprised of a sodium metal anode and sodium polysulfide catholyte separated by a Celgard or Nafion separator.

Polymer membranes are typically separated into porous membranes or single ion conductors. Porous membranes allow for high ionic conductivity and high permeability, but low selectivity which results in issues related to crossover of active species by separating molecules based on relative size to the pores[71]. Ion selective membranes allow for high selectivity through separating molecules based on relative charge compared to the membrane, but are marred by low ionic conductivity[101,102]. In this work, we will explore using a sodium conducting Nafion 117 versus a porous membrane, Celgard.

Nafion's success is based mainly in fuel cells and aqueous redox flow batteries for its high ionic conductivity, long cycle life, and its ability to mitigate crossover of active species[103]. Nafion has been explored for various applications for organic based batteries with vary levels of success[68,104,105]. Specifically, Nafion has been shown to mitigate the polysulfide shuttle effect which is similar to polysulfide crossover in NARFBs[38,106]. Taking inspiration from this previous work, we propose using Nafion as a polymer membrane in a sulfur-based metal NARFB. An effective membrane will allow for long duration cycling by mitigating crossover of the active species and provide a step towards realizing NARFBs as a transformative grid scale energy storage technology. With the model system of sodium polysulfides and sodium metal utilized, the detrimental effect of active species crossover is greatly enhanced due to the high reactivity of sodium metal with polysulfide species[107]. Sodium polysulfide also represents one of the highest specific capacity materials for NARFBs (1648 mAh/g_{sulfur}) though is limited by low order phase insolubility (Na_2S_4 →

Na_2S)[92]. For this purpose, cycling in this work was limited to a soluble regime with an expected capacity of (300-200 mAh/g), similar to other studies[70].

2. Materials and Methods

Materials: All electrochemical measurements, diffusion measurements, UV-Vis measurements, cell fabrication, and solution fabrication was performed in an INERT glovebox under an argon environment. The diglyme (2EGDME, 99%, Sigma Aldrich) and 1 molal sodium triflate (NaOTF, 98% Sigma Aldrich) solution were stored over 4A molecular sieve prior to electrochemical experiments. The Nafion 117 (Fuel Cell Store) membrane and Celgard 2325 were dried under vacuum prior to use. The Nafion 117 was sodium exchanged by soaking a Nafion membrane in 1M sodium hydroxide (NaOH, Thermoscientific) aqueous solution for 24 hours, with solution being replaced three times with fresh 1M NaOH solution. The membranes were then rinsed well with deionized water and dried under vacuum at 65 C for 24 hours. The carbon current collectors (Fuel Cell Store, Graphite Felt) were dried under vacuum overnight prior to use.

Electrolyte chemical experiments: The electrochemical cells used in this experiment were built from two stainless steel blocks with serpentine flow channels on the inner walls. The two compartments of the cell are separated by butyl rubber gaskets and either a Celgard or Nafion separator. The electrolyte was then added to reservoirs connected to the cell with polypropylene tubbing and using a peristatic pump for flow. The electrochemical experiments were performed on a VMP3 Biologic potientiostat.

Galvanostatic measurements were performed at a constant current of 0.427 mA from 1.75 to 3V vs Na/Na^+. Sodium metal was used as anode. Sodium polysulfide solutions made from a combination of sodium sulfide (Na_2S, Sigma Aldrich) and sulfur in 2EGDME (98%, Sigma Aldrich) were made at 1 molal concentrations.

UV-Vis spectroscopy: All measurements were performed on a JAZZ (Oceanoptics) spectrometer. The cuvette used was a flowthrough quartz cuvette with a pathlength of 1mm. The flowthrough cuvette was attach to a H-style diffusion cell which was constructed of two glass compartments separated by Celgard or Nafion using butyl rubber gaskets.

3. Results and Discussion

Crossover of sodium polysulfide was tracked using an H-cell configuration as shown in Figure 30a. Each compartment of the cell is filled with 1m sodium triflate (NaOTf) in diglyme (2EGDME) and the cell compartments are separated by either Celgard or Nafion, as shown in Figure 30a. One side is charged with a gram of 1m Na_2S_8 in 2EGDME. To note all references to polysulfide in this manuscript are to Na_2S_8 and not the derivates of this species. The blank compartment is connected to a flow through cuvette that allows for ultraviolet-visible (UV-Vis) spectroscopy. In these measurements, the change in concentration of the polysulfide has a linear relationship at peaks 297nm (99% R^2) and 426 nm (96% R^2) with the spectra used for the calibration curve shown in Figure 30b. The concentration can then be accurately equated to the absorbance of the band at 297 nm by using Beer's Law shown in Equation 13:

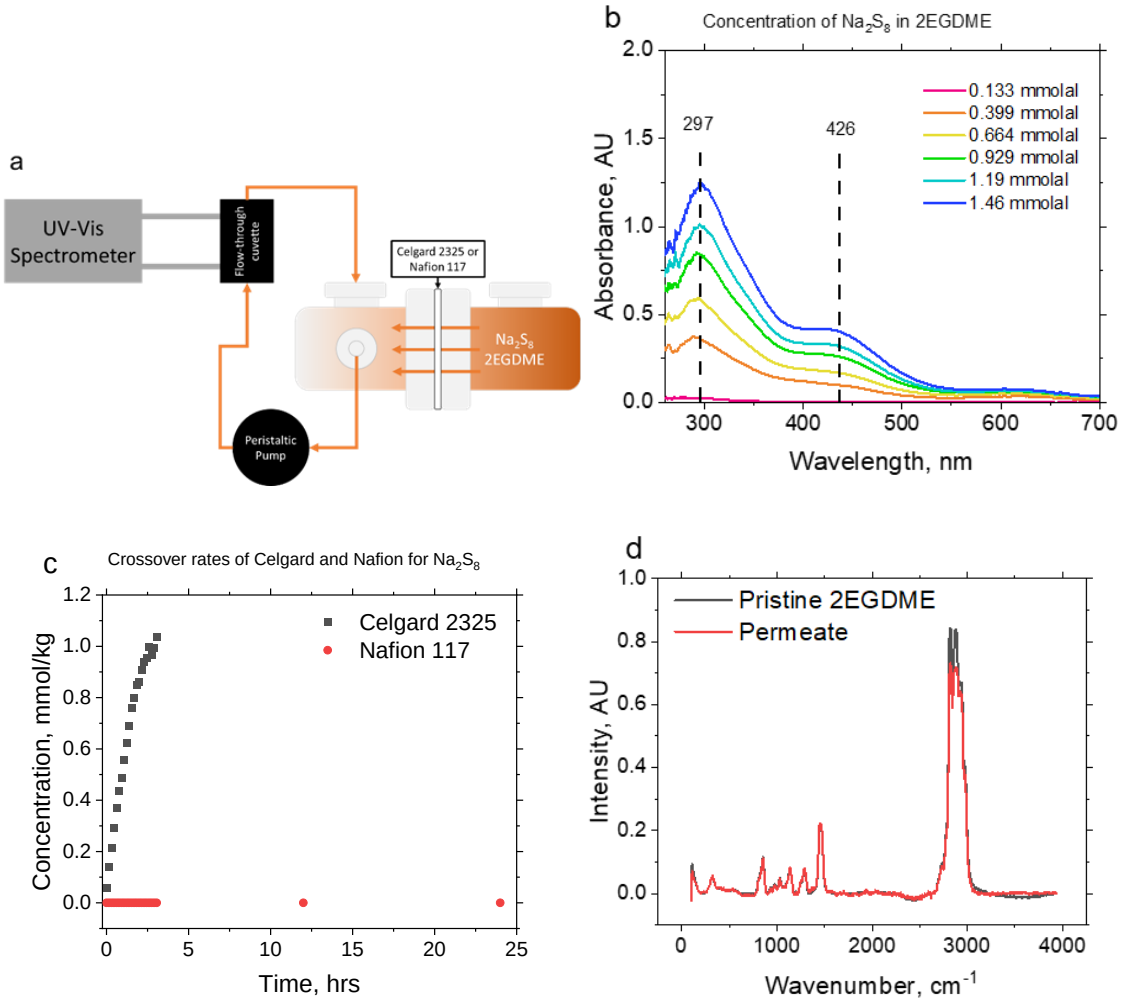

Figure 30: (a) Schematic of UV-Vis crossover setup using a glass diffusion cell with either Nafion or Celgard connected to a flow-through cuvette, (b) UV-vis spectra of Na_2S_8 in 2EGDME as a function of concentration, (c) concentration over time of the of Na_2S_8 that has crossed through Celgard 2325 or Nafion 117 and (d) Raman spectra of permeate from diffusion measurement after 7 days versus pristine diglyme.

Equation 13: $$\boldsymbol{A = \varepsilon b C}$$

Beer's Law equates absorbance of light, *A*, with a constant molar absorption coefficient, ε, the path length, *b*, and the concentration of the species in solution, *C*. The slow of the calibration curve gives the constants for the equation and allows for the accurate measurement of concentration as a function of absorbance. The time derivate of the detected polysulfide was taken as a function of concentration versus time by tracking changes in intensity of the absorbance peak at 297 nm The resulting translation of that measurement is shown in Figure 30c. Celgard shows a high rate of polysulfide crossover (3.9×10^4 mol/kg hr or 6.74×10^{-7} mol/cm^2 sec). This can be expected due to the high porosity of Celgard, 39%. The crossover rate begins to slow after the first two hours, but this can be attributed to an expected shift in the concentration gradient between the compartments of the diffusion cell. Nafion showed no polysulfide crossover over the course of three weeks.

We measured the Raman spectra of the permeate from the diffusion experiment after seven days showed no discernable amount of sodium polysulfide which has a strong Raman signal between 400-500 cm^{-1} from S-S bonding[98] as shown in Figure 30d. The fluorescence in the Raman spectra can be attributed to being exposed to Nafion as shown in Figure 31[41]. Similar results have been reported by Bauer et al that used Nafion as a blocker for polysulfide shuttling, an effect prominent in traditional sodium sulfur batteries[108]. Compared to the high crossover rate found in Celgard for Na_2S_8, Nafion

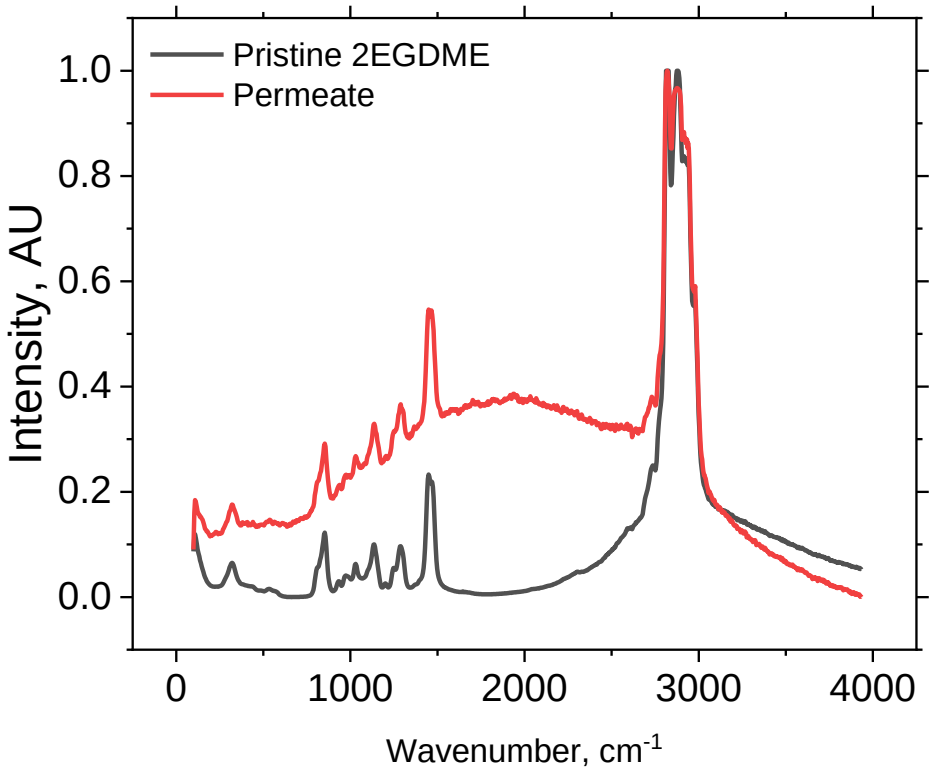

Figure 31: Raw Raman spectra of pristine 2EGDME and the permeate from a diffusion cell containing a Nafion membrane with 2EGDME//Nafion// Na_2S_8 in 2EGDME.

showed promising results as an inhibitor of active species crossover as the crossover rate was reduced to zero and confirmed with UV-Vis and Raman.

Crossover rate of polysulfide relates directly to cell performance as sodium polysulfide chemically reacts with sodium metal causing a passive film of sodium sulfide to form on its surface. This is typically represented as irreversible capacity loss as a function of time. The electrochemical cells utilized here consist of a stainless-steel cell stack with serpentine flow channels on each side. The cell stack is separated by Celgard or Nafion and contains a sodium metal anode and sodium polysulfide catholyte in 1m NaOTf in 2EGDME.

Both were cycled from 1.75 to 3V vs Na/Na^+ at C/10. With a Celgard membrane, huge losses in coulombic efficiency (as low as 74%) and quick capacity loss (20% capacity retention after 45 cycles) were measured. With a Nafion membrane, both the coulombic efficiency and capacity retention are higher than the Celgard counterpart (98% CE, 70% after 50 cycles). This improvement in cycling performance can attributed to the lack of crossover present in the system using a Nafion separator.

The voltage profiles for each in Figure 32c and 32d show that the large difference in charge and discharge capacity is during reduction of the Na_2S_8 but no new electrochemical redox reaction has occurred. This provides evidence that a chemical reaction is taking place between Na_2S_8 with another chemical most likely the sodium metal as that loss is reductive species is not present in the Nafion cell. It is also worth mentioning

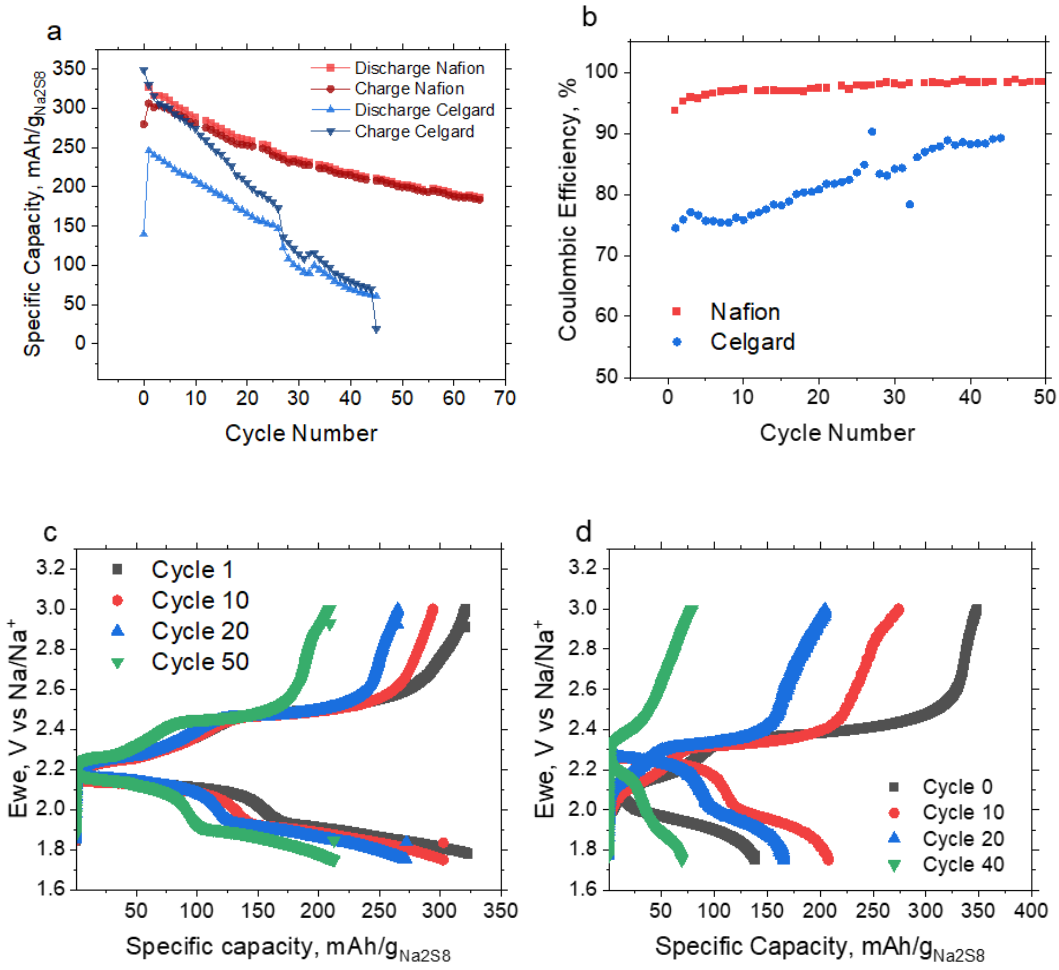

Figure 32: The galvanostatic cycling performance (a) and coulombic efficiency (b) of a Na metal//Celgard or Nafion//Na_2S_8 in 1m NaOTf in 2EGDME RFB cycling at C/10. The voltage profiles from the same cells for (c) Nafion 117 and (d) Celgard 2325.

that capacity losses of Na_2S_8 can also be contributed to side reactions with the carbon felt or by higher cycling rates as compared to literature (C/20)[69]. After disassembly, cells containing Nafion showed no visible sign of reaction of the sodium metal anode with the polysulfide, which is typically a deep yellow coloration on the surface of the sodium metal.

4. Conclusion

We used Nafion as an ion selective membrane for a sodium polysulfide NARFB. Its use showed significant improvement over porous polyethylene membranes in terms of cycle stability and high coulombic efficiency. For example, the Nafion-containing cell had a capacity retention of 75% after 50 cycles compared 25% after 45 cycles for cells using Celgard. The UV-Vis and electrochemical measurements suggests that the driver of these improvements is rooted in Nafion inhibition of polysulfide crossover. Further exploration of Nafion as an effective inhibitor of sodium polysulfide crossover in RFB could produce results that could improve the scalability of NARFB technology.

CHAPTER V

STABLE SODIUM METAL SEI ENABLES “MEMBRANE-LESS” NARFBS

A version of this chapter is planned to be published by J. Landon Tyler, Ethan Self, Guang Yang, Frank Delnick, Robert Sacci, and Jagjit Nanda

This work was primarily performed by me. All electrochemical experiments were performed by me. Experimental design and analysis were performed by me, Ethan Self, Frank Delnick, and Guang Yang. EIS measurements and analysis was assisted by Robert Sacci. Jagjit Nanda was the primary investigator of this work.

Abstract

Nonaqueous redox flow batteries are bottlenecked by current membrane selections. Membranes for NARFBs act as an inhibitor of the crossover of redox couples during cycling while allowing the conduction of ions. In this work, we explore forming a stable SEI on the surface of sodium metal to protect against redox couple reactions. Using a combination of EIS and galvanostatic cycling, we demonstrate the possibility of using this stable SEI in NARFBs as an alternative to a crossover inhibiting membrane. Results from this work indicate that the passive is stable for hundreds of hours and its stability versus a selection of common redox couples used commonly in literature.

1. Introduction

Redox flow batteries have been in the development for the last few decades. RFBs offer the potential for high energy density per battery and long duration storage which are ideal for grid-scale storage. Even with decades of research, RFBs are still bottlenecked by

fundamental issues related to the crossover of active species within the electrolyte. Nonaqueous redox flow batteries (NARFBs) have a greater potential at higher energy and power density than its aqueous analogue, but crossover is even more pronounced. Crossover of active species during cycling typically leads to irreversible capacity loss, quick fading of capacity, and ultimately device failure. Crossover can be solved with the use of suitable membranes, but current membranes are expensive, not scalable for grid-scale storage, or not suitable for long duration storage.

Clever solutions have been studied by using various novel cell designs to mitigate crossover. In this study, we propose forming a stable SEI on the surface of sodium metal to mitigate the effects of crossover rather than the crossover itself. In previous studies, it has been shown that sodium metal in the presence of $NaPF_6$ in 2EGDME and other glymes forms a stable SEI that can withstand hundreds of cycles with no loss in coulombic efficiency. Redox couples in NARFBs are known to be chemically reactive and a thorough investigation of the SEI both as a function of time, in the flow cell configuration, and in the presence of various redox couples is necessary for a full understanding of the SEI's viability in NARFBs.

2. Materials and methods

Electrochemical measurements: coin cells (316 L stainless steel, CR2032, Hohsen Corp., Osaka, Japan) were fabricated in an argon-filled glovebox. The cells contained either two sodium metal electrodes or a sodium anode and copper foil working electrode. The electrolyte solution was either $NaPF_6$ (98%, Sigma Aldrich), NaTFSI (98%, Sigma

Aldrich), NaFSI (98%, Sigma Aldrich), or $NaClO_4$ (98%, Sigma Aldrich) in DME (99%, Mitsubishi), 2EGDME (98%, Sigma Aldrich), or TEGMDE (98%, Sigma Aldrich). The electrolyte solution was stored in an argon filled glovebox. Redox flow batteries were fabricated using a stainless-steel cell stack with serpentine flow channels, butyl rubber gaskets, and a Celgard 2325 separator. The flow was maintained with a peristaltic pump. The current collector for the flowing redox couple was copper foil/ mesh or graphite felt. All electrochemical measurements were performed with a VMP3 or SP Biologic potentiostat. The cycling rates are detailed in the manuscript. EIS measurements were performed from 20 kHz to 10 mHz.

3. Results and discussions

Long duration energy storage requires periods of time that last months and years. To gauge the durability of the SEI formed on sodium metal, EIS measurements were performed as a function of time in various electrolyte solutions is shown in Figure 33. To gauge the effectiveness and stability of the passive film formed on sodium metal in the presence of 1m $NaPF_6$ in 2EGDME. Figure 33a shows that after an initial pulse, the EIS response shows a large decrease in the ESR of the first semicircle which attributed to the passive film on sodium metal. This decrease in ESR continues even after 144 hours. Comparing these results to the other glymes, DME and TEGDME, in Figure 33b. The ESR for both DME and TEGDME are larger than that of 2EGDME on average over the course of 100 hours. This matches well with the cycling performance presented in a previous studying this specific sodium passivation. $NaClO_4$, NaTFSI, and NaOTf were

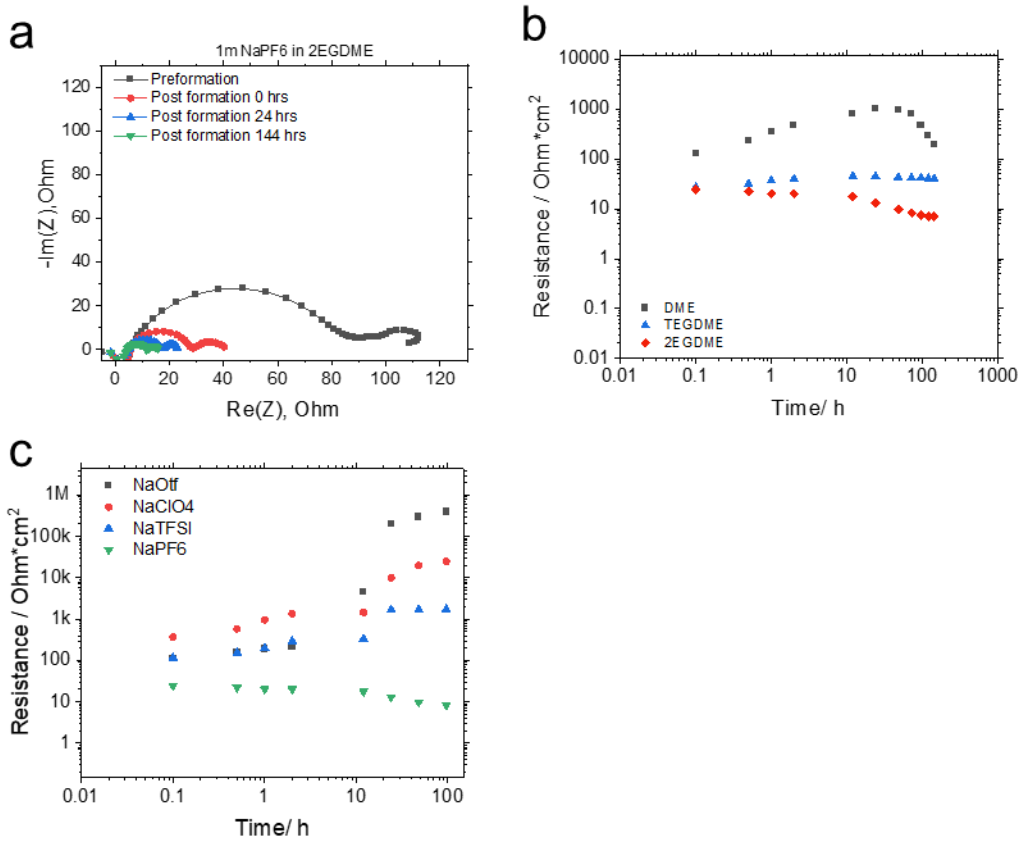

Figure 33: (a) The EIS measurements of Na//Celgard//Na coin cell containing 1m $NaPF_6$ in 2EGME over time preformation and periodically after formation. (b) The ESR of the passive film on sodium metal as a function of time with cells containing 1m $NaPF_6$ in DME, 2EGDME, TEGDME. (c) The ESR of the passive film on sodium metal as a function of time with cells containing 1m $NaPF_6$, NaOTf, NaTFSI, or $NaClO_4$ in 2EGDME.

also investigated to confirm that inability to form a stable passive film. Figure 33c shows EIS measurements of the passive film formed in each of these electrolytes. $NaPF_6$ is the only electrolyte solution that forms a stable passive film.

The cycle performance of sodium also matches well with Figure 34 shows stable cycling up to 50 cycles with 99% CE. The rate capability of the sodium metal was also gauged to measure the limiting current density for this electrochemical process. Figure 34c demonstrate the rate capability measurements and that the limiting current density is approximately 2 mA/cm^2.

For these passive films to be useful for NARFBs, the passive films must be stable against presence of the redox chemicals. EL-cells were implemented for measuring changes in the passive film in the presence of dissolved redox couples. EL-cells can be easily opened and reassembled. Figure 35a shows that the addition of sodium polysulfide causes a large increase in the ESR over the period of 24 hours but decreases after 10 days. This decrease in ESR could be caused by the reactions of the polysulfide with the sodium metal SEI which in a recent study. The study shows that new SEI formed from the reaction between the SEI and polysulfide results in a new, stable SEI that allows for long term, efficient sodium plating and stripping. The key difference is that polysulfide is used in an extremely small amount as an additive rather than in large excess that would be present in a flow cell. TEMPO shows a slight increase in ohmic resistance which could be due to opening of the EL-cell, but after an hour, the ohmic resistance returns to

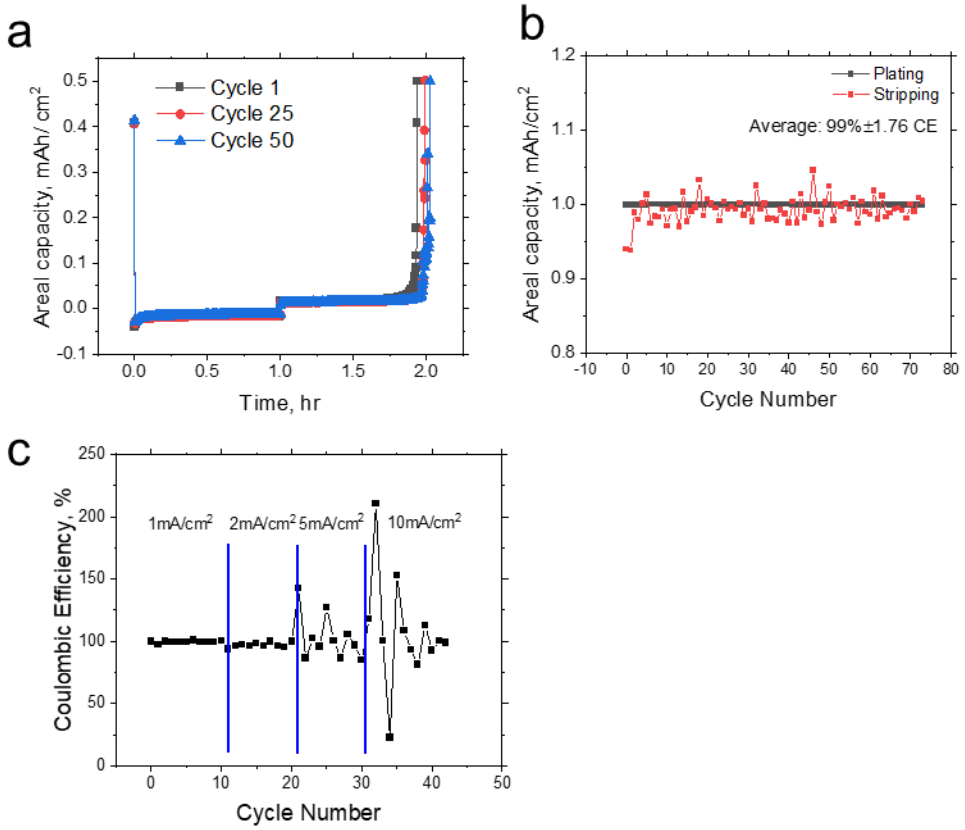

Figure 34: (a) The voltage profile of stripping and plating of sodium metal in a Na//Celgard//Cu coin cell containing 1m $NaPF_6$ in 2EGDME. (b) The coulombic efficiency of the plating and stripping cycling. (c) The rate capability of sodium plating and stripping of sodium metal in the coin cells containing 1m $NaPF_6$ in 2EGDME.

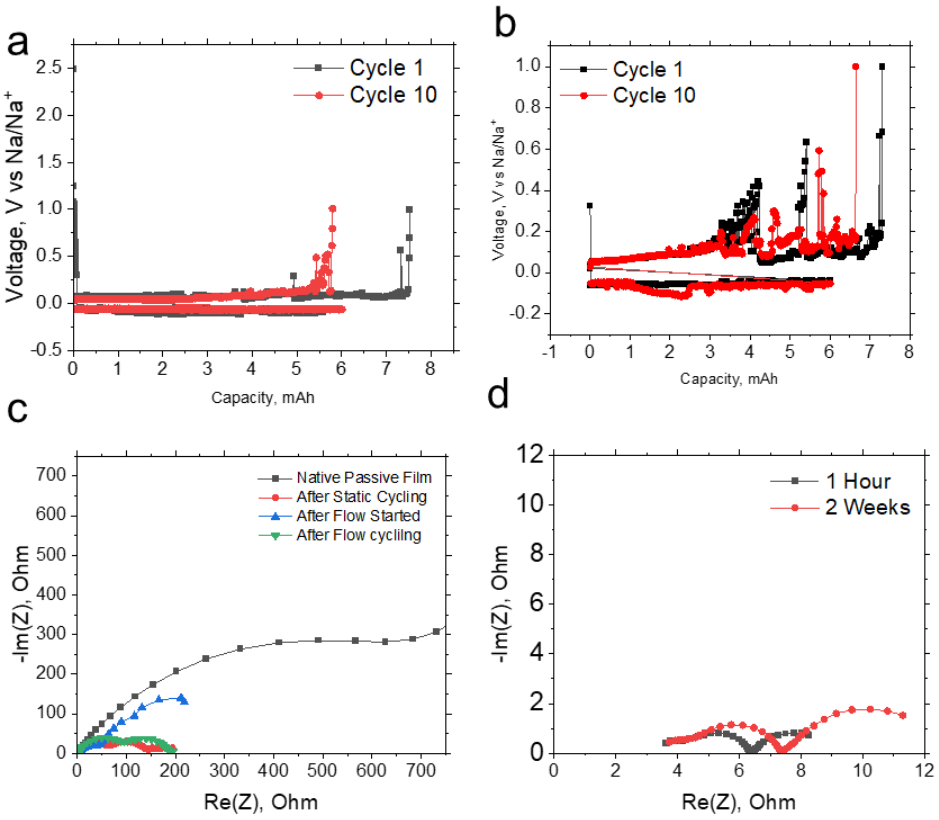

Figure 35: The cycling performance of a redox flow battery containing a sodium metal anode and copper foil working electrode (a) static and (b) with electrolyte flowing. (c) The EIS of different states of the flow battery including the native passivation layer on sodium, the passivation layer on sodium after static cycling and flowing cycling, and immediately after starting the flow. (d) The EIS of the flow battery after sodium has been plated on the copper after an hour of waiting and two weeks of waiting.

normal. The passive film also does not increase in ESR as a function of time as shown in Figure 35c. This result shows a promising result of being a potential redox couple that is stable against sodium metal. Benzoquinone has the largest increase in ESR and also visibly reacts on contact with sodium metal.

It is also important to see how the passive film and stripping and plating of sodium are affected in a flow battery. A flow battery containing a sodium metal anode and copper foil working electrode was constructed using 1m $NaPF_6$ in 2EGDME as the electrolyte. The cell was cycled without flow showing that the formation step used for the coin cells is not long enough, but after 10 cycles a coulombic efficiency of 99% was reached as shown in Figure 36a. This same measurement performed while the electrolyte is flowing showed spikes in voltage during stripping as shown in Figure 36b. EIS measurements were performed during different stages of operation shown in Figure 36c. After cycling with no flow of electrolyte, the ESR of the cell attributed to the passive film decreased drastically (1000 Ohms to 65 Ohms). The flow of the electrolyte was started after static cycling. The frequency region attributed to diffusion shows a large change and becomes uninterpretable. After 10 cycles while flowing the electrolyte, the EIS response returns to a similar response to that after 10 cycles of static cycling. EIS was also taken periodically after plating sodium on to the copper foil. After two weeks of no further electrochemical influences, the passive film shows little growth in ESR. These results indicate that the plating and stripping of sodium in the redox flow battery geometry is possible but can be affected by the flow of electrolyte. Also, the passive film on the

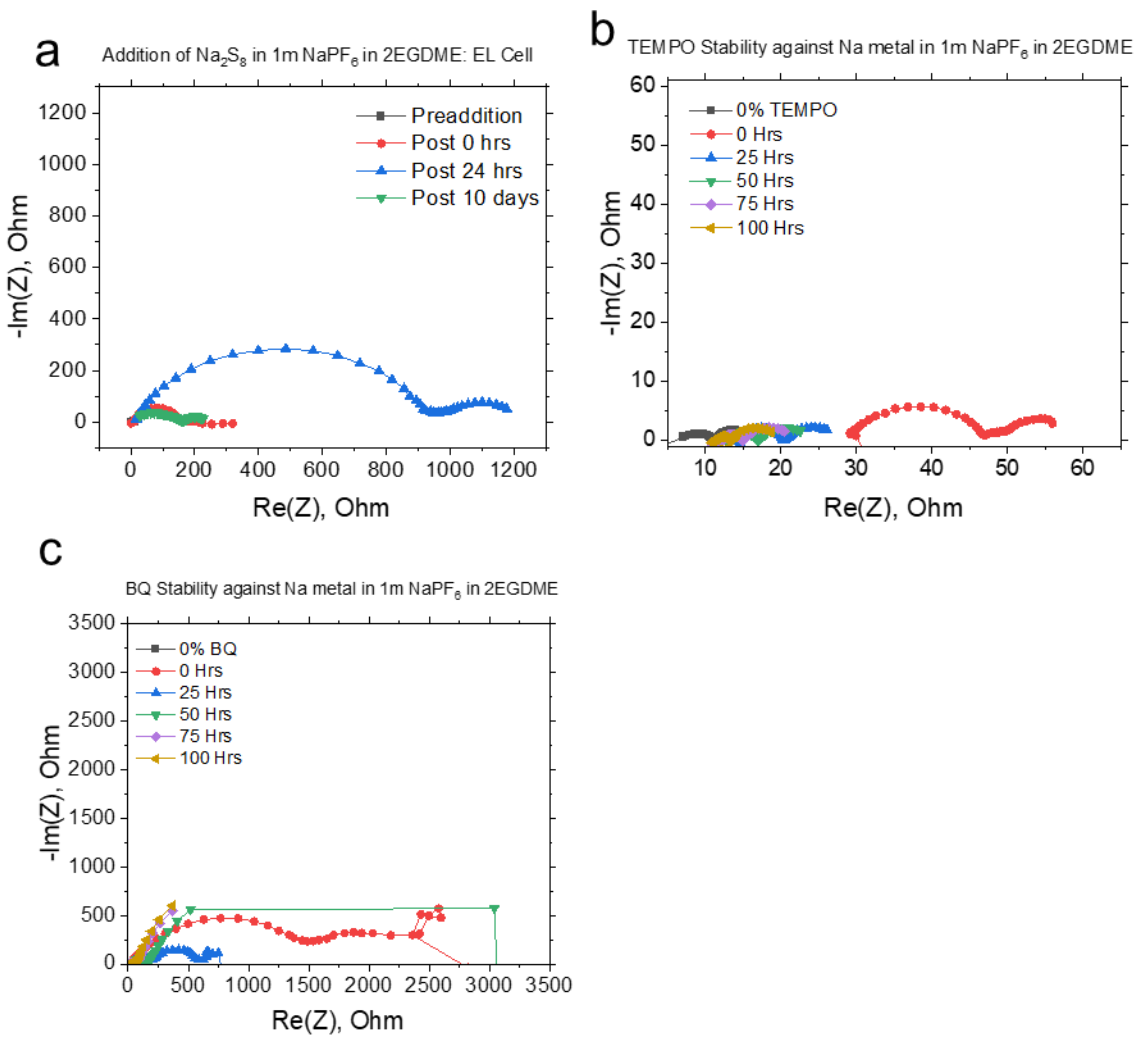

Figure 36: The EIS measurements of EL-cells containing Na//Celgard//Cu foil containing 1m $NaPF_6$ then exposed to (a) sodium polysulfide, (b) TEMPO, or (c) BQ after a formation cycle.

sodium is not as stable and shows a growth in ESR as time passes which was not observed in the static coin cells.

4. Conclusion

This work provides evidence of stable sodium metal SEI in a flow cell geometry and potential framework for studying the effect of redox couples against sodium metal. The SEI on sodium metal shows stability greater than 100 hours, but only for electrolyte containing both $NaPF_6$ and 2EGDME. Further measurements in a flow cell geometry show that the passive film is affected by the flowing electrolyte and causes a small growth in resistance over time. The EIS measurements of the passive film in contact with Na_2S_8, TEMPO, and BQ prove that passive film can potentially be stable against some redox couples, but more research is necessary to learn the extent of the protection of this passive film.

CONCLUSION

In conclusion, the addition of Lewis bases can improve the thermal stability of $NaPF_6$ in DME at temperatures as high as 80 °C as confirmed with EIS, GC, and FTIR. Acetone and DME can improve the low temperature performance of NaTFSI in acetonitrile at temperatures as low as -60 °C as confirmed with EIS, DSC, and GC. Nafion can be used as an effective inhibitor of sodium polysulfide crossover and increase capacity retention up to 70% after 50 cycles as confirmed with UV-Vis, Raman, EIS, and GC. Passive films on sodium metal can enable possible membrane-less approach for nonaqueous redox flow batteries and are stable for hundreds of hours with no increase in ESR when using 1m $NaPF_6$ in 2EGMDE as an electrolyte as confirmed with EIS and GC.

REFERENCES

1. Yang, Y. *et al.* On the sustainability of lithium ion battery industry – A review and perspective. *Energy Storage Mater.* **36**, 186–212 (2021).
2. Marom, R., Amalraj, S. F., Leifer, N., Jacob, D. & Aurbach, D. A review of advanced and practical lithium battery materials. *J. Mater. Chem.* **21**, 9938–9954 (2011).
3. Nayak, P. K., Yang, L., Brehm, W. & Adelhelm, P. From Lithium-Ion to Sodium-Ion Batteries: Advantages, Challenges, and Surprises. *Angew. Chemie - Int. Ed.* **57**, 102–120 (2018).
4. Bommier, C. & Ji, X. Electrolytes, SEI Formation, and Binders: A Review of Nonelectrode Factors for Sodium-Ion Battery Anodes. *Small* **14**, (2018).
5. Kühnel, R. S., Lübke, M., Winter, M., Passerini, S. & Balducci, A. Suppression of aluminum current collector corrosion in ionic liquid containing electrolytes. *J. Power Sources* **214**, 178–184 (2012).
6. Gachot, G. *et al.* Gas chromatography/mass spectrometry as a suitable tool for the li-ion battery electrolyte degradation mechanisms study. *Anal. Chem.* **83**, 478–485 (2011).
7. Yu, Y. *et al.* Non-flammable organic electrolyte for sodium-ion batteries. *Electrochem. commun.* **110**, 106635 (2020).
8. Lahiri, A. & Endres, F. Review—Electrodeposition of Nanostructured Materials from Aqueous, Organic and Ionic Liquid Electrolytes for Li-Ion and Na-Ion

Batteries: A Comparative Review. *J. Electrochem. Soc.* **164**, D597–D612 (2017).

9. Zhang, S. S. A review on electrolyte additives for lithium-ion batteries. *J. Power Sources* **162**, 1379–1394 (2006).
10. Galiński, M., Lewandowski, A. & Stepniak, I. Ionic liquids as electrolytes. *Electrochim. Acta* **51**, 5567–5580 (2006).
11. Brushett, F. R., Vaughey, J. T. & Jansen, A. N. An All-Organic Non-aqueous Lithium-Ion Redox Flow Battery. *Adv. Energy Mater.* 1–7 (2012) doi:10.1002/aenm.201200322.
12. Hayamizu, K. & Aihara, Y. Ion and solvent diffusion and ion conduction of PC-DEC and PC-DME binary solvent electrolytes of LiN(SO2CF3)2. *Electrochim. Acta* **49**, 3397–3402 (2004).
13. Quartarone, E. & Mustarelli, P. Electrolytes for solid-state lithium rechargeable batteries: recent advances and perspectives. *Chem. Soc. Rev.* **40**, 2525 (2011).
14. Park, M., Zhang, X., Chung, M., Less, G. B. & Sastry, A. M. A review of conduction phenomena in Li-ion batteries. *J. Power Sources* **195**, 7904–7929 (2010).
15. Zhang, S. S. A review on electrolyte additives for lithium-ion batteries. *J. Power Sources* **162**, 1379–1394 (2006).
16. Guillot, S. L., Peña-Hueso, A., Usrey, M. L. & Hamers, R. J. Thermal and Hydrolytic Decomposition Mechanisms of Organosilicon Electrolytes with Enhanced Thermal Stability for Lithium-Ion Batteries. *J. Electrochem. Soc.* **164**,

A1907–A1917 (2017).

17. Hu, M., Pang, X. & Zhou, Z. Recent progress in high-voltage lithium ion batteries. *J. Power Sources* **237**, 229–242 (2013).

18. Zhang, H., Feng, W., Nie, J. & Zhou, Z. Recent progresses on electrolytes of fluorosulfonimide anions for improving the performances of rechargeable Li and Li-ion battery. *J. Fluor. Chem.* **174**, 49–61 (2015).

19. Lewandowski, A. & Świderska-Mocek, A. Ionic liquids as electrolytes for Li-ion batteries-An overview of electrochemical studies. *J. Power Sources* **194**, 601–609 (2009).

20. Tarascon, J. M. & Armand, M. Issues and challenges facing rechargeable lithium batteries. *Nature* **414**, 359–67 (2001).

21. Aurbach, D. *et al.* Design of electrolyte solutions for Li and Li-ion batteries: A review. *Electrochim. Acta* **50**, 247–254 (2004).

22. Zhu, M. *et al.* An in-situ formed stable interface layer for high-performance sodium metal anode in a non-flammable electrolyte. *Energy Storage Mater.* **42**, 145–153 (2021).

23. Verma, P., Maire, P. & Novák, P. A review of the features and analyses of the solid electrolyte interphase in Li-ion batteries. *Electrochim. Acta* **55**, 6332–6341 (2010).

24. Zhang, S. S., Xu, K. & Jow, T. R. EIS study on the formation of solid electrolyte interface in Li-ion battery. *Electrochim. Acta* **51**, 1636–1640 (2006).

25. Gao, L. *et al.* Revealing the chemistry of an anode-passivating electrolyte salt for high rate and stable sodium metal batteries. *J. Mater. Chem. A* **6**, 12012–12017 (2018).

26. Zhang, Z. *et al.* Fluorinated electrolytes for 5 v lithium-ion battery chemistry. *Energy Environ. Sci.* **6**, 1806–1810 (2013).

27. Morales, D., Ruther, R. E., Nanda, J. & Greenbaum, S. Ion transport and association study of glyme-based electrolytes with lithium and sodium salts. *Electrochim. Acta* **304**, 239–245 (2019).

28. Aurbach, D. Electrode-solution interactions in Li-ion batteries: A short summary and new insights. *J. Power Sources* **119**–**121**, 497–503 (2003).

29. Goren, E., (Youngman) Chusid, O. & Aurbach, D. The Application of In SITU FTIR Spectroscopy to the Study of Surface Films Formed on Lithium and Noble Metals at Low Potentials in Li Battery Electrolytes. *J. Electrochem. Soc.* **138**, 6–9 (1991).

30. Yang, X. & Rogach, A. L. Electrochemical Techniques in Battery Research: A Tutorial for Nonelectrochemists. *Adv. Energy Mater.* **9**, 1–10 (2019).

31. Shobukawa, H., Tokuda, H., Tabata, S. I. & Watanabe, M. Preparation and transport properties of novel lithium ionic liquids. *Electrochim. Acta* **50**, 305–309 (2004).

32. Park, Y. *et al.* Investigation of solid electrolyte interface (SEI) film on LiCoO2cathode in fluoroethylene carbonate (FEC)-containing electrolyte by 2D

correlation X-ray photoelectron spectroscopy (XPS). *J. Mol. Struct.* **1069**, 157–163 (2014).

33. Pajkossy, T. & Kolb, D. M. The interfacial capacitance of Au(100) in an ionic liquid, 1-butyl-3-methyl-imidazolium hexafluorophosphate. *Electrochem. commun.* **13**, 284–286 (2011).

34. Taberna, P. L., Simon, P. & Fauvarque, J. F. Electrochemical Characteristics and Impedance Spectroscopy Studies of Carbon-Carbon Supercapacitors. *J. Electrochem. Soc.* **150**, A292 (2003).

35. Andre, D. *et al.* Characterization of high-power lithium-ion batteries by electrochemical impedance spectroscopy. I. Experimental investigation. *J. Power Sources* **196**, 5334–5341 (2011).

36. Santner, H. J., Korepp, C., Winter, M., Besenhard, J. O. & Möller, K. C. In-situ FTIR investigations on the reduction of vinylene electrolyte additives suitable for use in lithium-ion batteries. *Anal. Bioanal. Chem.* **379**, 266–271 (2004).

37. Xu, M. *et al.* Experimental and theoretical investigations of dimethylacetamide (DMAc) as electrolyte stabilizing additive for lithium ion batteries. *J. Phys. Chem. C* **115**, 6085–6094 (2011).

38. Bauer, I., Thieme, S., Brückner, J., Althues, H. & Kaskel, S. Reduced polysulfide shuttle in lithium-sulfur batteries using Nafion-based separators. *J. Power Sources* **251**, 417–422 (2014).

39. Tyler, J. L., Sacci, R. L. & Nanda, J. Anion Coordination Improves High -

Temperature Performance and Stability of NaPF6 - Based Electrolytes for Supercapacitors. *Energies* **14**, 4409 (2021).

40. Piscanec, S. *et al.* Raman spectroscopy of silicon nanowires. *Phys. Rev. B* **68**, 241312 (2003).

41. Janz, G. J., Roduner, E., Coutts, J. W. & Downey, J. R. Raman Studies of Sulfur-Containing Anions in Inorganic Polysulfides. Barium Trisulfide. *Inorg. Chem.* **15**, 1751–1754 (1976).

42. Morita, M., Asai, Y., Yoshimoto, N. & Ishikawa, M. A Raman spectroscopic study of organic electrolyte solutions based on binary solvent systems of ethylene carbonate with low viscosity solvents which dissolve different lithium salts. *J. Chem. Soc. Faraday Trans.* **94**, 3451–3456 (1998).

43. Carbone, L. *et al.* Characteristics of glyme electrolytes for sodium battery: nuclear magnetic resonance and electrochemical study. *Electrochim. Acta* **231**, 223–229 (2017).

44. Nie, M., Abraham, D. P., Chen, Y., Bose, A. & Lucht, B. L. Silicon Solid Electrolyte Interphase (SEI) of Lithium Ion Battery Characterized by Microscopy and Spectroscopy Silicon solid electrolyte interphase (SEI) of lithium ion battery characterized by microscopy and spectroscopy. *J. Phys. Chem. C* **117**, 13403–13412 (2013).

45. Campion, C. L. *et al.* Suppression of Toxic Compounds Produced in the Decomposition of Lithium-Ion Battery Electrolytes. *Electrochem. Solid-State Lett.*

7, 194–197 (2004).

46. Geoffroy, I., Willmann, P., Mesfar, K., Carré, B. & Lemordant, D. Electrolytic characteristics of ethylene carbonate-diglyme-based electrolytes for lithium batteries. *Electrochim. Acta* **45**, 2019–2027 (2000).

47. Vali, R., Janes, A. & Lust, E. Vinylene Carbonate as Co-Solvent for Low-Temperature Mixed Electrolyte Based Supercapacitors. *J. Electrochem. Soc.* **163**, A851–A857 (2016).

48. Chayambuka, K., Mulder, G., Danilov, D. L. & Notten, P. H. L. Sodium-Ion Battery Materials and Electrochemical Properties Reviewed. *Adv. Energy Mater.* **8**, (2018).

49. Kundu, D., Talaie, E., Duffort, V. & Nazar, L. F. The emerging chemistry of sodium ion batteries for electrochemical energy storage. *Angew. Chemie - Int. Ed.* **54**, 3432–3448 (2015).

50. Li, W. *et al.* Additives for Stabilizing LiPF[sub 6]-Based Electrolytes Against Thermal Decomposition. *J. Electrochem. Soc.* **152**, A1361 (2005).

51. Zhang, S. S., Xu, K. & Jow, T. R. Tris(2,2,2-trifluoroethyl) phosphite as a co-solvent for nonflammable electrolytes in Li-ion batteries. *J. Power Sources* **113**, 166–172 (2003).

52. Bolloju, S., Chiou, C. Y., Vikramaditya, T. & Lee, J. T. (Pentafluorophenyl)diphenylphosphine as a dual-functional electrolyte additive for LiNi 0.5 Mn 1.5 O 4 cathodes in high-voltage lithium-ion batteries. *Electrochim.*

Acta **299**, 663–671 (2019).

53. Li, W. *et al.* Additives for Stabilizing LiPF[sub 6]-Based Electrolytes Against Thermal Decomposition. *J. Electrochem. Soc.* **152**, A1361 (2005).

54. Winter, M. & Brodd, R. J. What are batteries, fuel cells, and supercapacitors? *Chem. Rev.* **104**, 4245–4269 (2004).

55. Ruther, R. E. *et al.* Stable Electrolyte for High Voltage Electrochemical Double-Layer Capacitors. *J. Electrochem. Soc.* **164**, A277–A283 (2017).

56. Taberna, P. L., Simon, P. & Fauvarque, J. F. Electrochemical Characteristics and Impedance Spectroscopy Studies of Carbon-Carbon Supercapacitors. *J. Electrochem. Soc.* **153**, 292–300 (2003).

57. Cho, Y. G., Kim, Y. S., Sung, D. G., Seo, M. S. & Song, H. K. Nitrile-assistant eutectic electrolytes for cryogenic operation of lithium ion batteries at fast charges and discharges. *Energy Environ. Sci.* **7**, 1737–1743 (2014).

58. Martins, M. L. *et al.* Addition of Chloroform in a Solvent-in-Salt Electrolyte: Outcomes in the Microscopic Dynamics in Bulk and Confinement. *J. Phys. Chem. C* **124**, 22366–22375 (2020).

59. Kramer, E. *et al.* Mechanism of Anodic Dissolution of the Aluminum Current Collector in 1 M LiTFSI EC:DEC 3:7 in Rechargeable Lithium Batteries. *J. Electrochem. Soc.* **160**, A356–A360 (2012).

60. Brandon, E. J., West, W. C., Smart, M. C., Whitcanack, L. D. & Plett, G. A. Extending the low temperature operational limit of double-layer capacitors. *J.*

Power Sources **170**, 225–232 (2007).

61. Petrowsky, M. & Frech, R. Temperature dependence of ion transport: The compensated arrhenius equation. *J. Phys. Chem. B* **113**, 5996–6000 (2009).

62. Sun, Y. *et al.* Salty Ice Electrolyte with Superior Ionic Conductivity Towards Low-Temperature Aqueous Zinc Ion Hybrid Capacitors. *Adv. Funct. Mater.* **31**, 1–10 (2021).

63. Chen, H., Cong, G. & Lu, Y. Recent progress in organic redox flow batteries : Active materials , electrolytes and membranes. *J. Energy Chem.* **27**, 1304–1325 (2018).

64. Shin, S. H., Yun, S. H. & Moon, S. H. A review of current developments in non-aqueous redox flow batteries: Characterization of their membranes for design perspective. *RSC Adv.* **3**, 9095–9116 (2013).

65. Minke, C. & Turek, T. Materials , system designs and modelling approaches in techno-economic assessment of all-vanadium redox flow batteries – A review. *J. Power Sources* **376**, 66–81 (2018).

66. Gong, K., Fang, Q., Gu, S., Li, S. F. Y. & Yan, Y. Nonaqueous redox-flow batteries: Organic solvents, supporting electrolytes, and redox pairs. *Energy Environ. Sci.* **8**, 3515–3530 (2015).

67. Wei, X. *et al.* Radical Compatibility with Nonaqueous Electrolytes and Its Impact on an All-Organic Redox Flow Battery **. *Angew. Commun.* **54**, 8684–8687 (2015).

68. Abdul Aziz, M., Oh, K. & Shanmugam, S. A sulfonated poly(arylene ether ketone)/polyoxometalate-graphene oxide composite: A highly ion selective membrane for all vanadium redox flow batteries. *Chem. Commun.* **53**, 917–920 (2017).

69. Pan, H., Wei, X., Henderson, W. A., Shao, Y. & Chen, J. On the Way Toward Understanding Solution Chemistry of Lithium Polysulfi des for High Energy Li – S Redox Flow Batteries. *Adv. Energy Mater.* **5**, 1–7 (2015).

70. Self, E. C., Tyler, J. L. & Nanda, J. Ambient Temperature Sodium Polysulfide Catholyte for Nonaqueous Redox Flow Batteries. *J. Electrochem. Soc.* **168**, 080540 (2021).

71. Liang, Z. *et al.* Comparison of Separators vs Membranes in Nonaqueous Redox Flow Battery Electrolytes Containing Small Molecule Active Materials. *ACS Appl. Energy Mater.* **4**, 5443–5451 (2021).

72. Seh, Z. W., Sun, J., Sun, Y. & Cui, Y. A highly reversible room-temperature sodium metal anode. *ACS Cent. Sci.* **1**, 449–455 (2015).

73. Liu, C., Yu, Z., Neff, D., Zhamu, A. & Jang, B. Z. Graphene-Based Supercapacitor with an Ultrahigh Energy Density. *Nano Lett.* **10**, 4863–4868 (2010).

74. Scrosati, B. & Garche, J. Lithium batteries: Status, prospects and future. *J. Power Sources* **195**, 2419–2430 (2010).

75. Balducci, A., Dugas, R., Taberna, P. L., Simon, P. & Pl, D. High temperature carbon – carbon supercapacitor using ionic liquid as electrolyte. *J. Power Sources*

165, 922–927 (2007).

76. Yan, J., Wang, Q., Wei, T. & Fan, Z. Recent Advances in Design and Fabrication of Electrochemical Supercapacitors with High Energy Densities. *Adv. Energy Mater.* **4**, 1300816 (2014).

77. Béguin, F., Presser, V., Balducci, A. & Frackowiak, E. Carbons and Electrolytes for Advanced Supercapacitors. *Adv. Mater.* **26**, 2219–2251 (2020).

78. Conte, M. Supercapacitors Technical Requirements for New Applications. *Fuel Cells* 806–818 (2010) doi:10.1002/fuce.201000087.

79. Kanchev, H., Lu, D., Colas, F., Lazarov, V. & Francois, B. Energy Management and Operational Planning of a Microgrid With a PV-Based Active Generator for Smart Grid Applications. *IEEE Trans. Ind. Electron.* **58**, 4583–4592 (2011).

80. Hung, K., Masarapu, C., Ko, T. & Wei, B. Wide-temperature range operation supercapacitors from nanostructured activated carbon fabric. *J. Power Sources* **193**, 944–949 (2009).

81. Rafik, F., Gualous, H., Gallay, R., Crausaz, A. & Berthon, A. Frequency , thermal and voltage supercapacitor characterization and modeling. *J. Power Sources* **165**, 928–934 (2007).

82. Jian-wen, L. I. U., Xin-hai, L. I. & Zhi-xing, W. Preparation and characterization of lithium hexafluorophosphate for lithium-ion battery electrolyte. *Trans. Nonferrous Met. Soc. China* **20**, 344–348 (2010).

83. Bohlen, O., Kowal, J. & Sauer, D. U. Ageing behaviour of electrochemical double

layer capacitors Part I . Experimental study and ageing model. *J. Power Sources* **172**, 468–475 (2007).

84. Lugez, C. L., Irikura, K. K. & Jacox, M. E. Experimental and ab initio study of the infrared spectra of ionic species derived from and and trapped in solid neon. *J. Chem. Phys.* **108**, 8381–8393 (1998).

85. Wilken, S., Johansson, P. & Jacobsson, P. Infrared spectroscopy of instantaneous decomposition products of LiPF 6 -based lithium battery electrolytes. *Solid State Sci.* **225**, 608–610 (2012).

86. Lekgoathi, M. D. S., Vilakazi, B. M., Wagener, J. B., Roux, J. P. Le & Moolman, D. Decomposition kinetics of anhydrous and moisture exposed LiPF 6 salts by thermogravimetry. *J. Fluor. Chem.* **149**, 53–56 (2013).

87. Nishi, Y. Lithium ion secondary batteries; past 10 years and the future. *J. Power Sources* **100**, 101–106 (2001).

88. Tan, S., Ji, Y. J., Zhang, Z. R. & Yang, Y. Recent progress in research on high-voltage electrolytes for lithium-ion batteries. *ChemPhysChem* **15**, 1956–1969 (2014).

89. Zhang, S. S., Xu, K. & Jow, T. R. Tris(2,2,2-trifluoroethyl) phosphite as a co-solvent for nonflammable electrolytes in Li-ion batteries. *J. Power Sources* **113**, 166–172 (2003).

90. Shi, Y. *et al.* Role of Amines in Thermal-Runaway-Mitigating Lithium-Ion Battery. *ACS Appl. Mater. Interfaces* **8**, 30956–30963 (2016).

91. Galimzyanov, R. R. *et al.* Electrolyte mixture based on acetonitrile and ethyl acetate for a wide temperature range performance of the supercapacitors. *J. Power Sources* **495**, (2021).

92. Zhang, S. *et al.* Reviews Recent Progress in Polysulfide Redox-Flow Batteries. *Batter. Supercaps* **2**, 627–637 (2019).

93. Self, E. C., Delnick, F. M., Ruther, R. E., Allu, S. & Nanda, J. High-Capacity Organic Radical Mediated Phosphorus Anode for Sodium-Based Redox Flow Batteries. *ACS Energy Lett.* **4**, 2593–2600 (2019).

94. Yang, Y., Zheng, G. & Cui, Y. A membrane-free lithium/polysulfide semi-liquid battery for large-scale energy storage. *Energy Environ. Sci.* **6**, 1552–1558 (2013).

95. Yang, G. *et al.* Anomalously high elastic modulus of a poly(ethylene oxide)-based composite electrolyte. *Energy Storage Mater.* **35**, 431–442 (2021).

96. Lehmann, M. L. *et al.* Tailored crosslinking of Poly(ethylene oxide) enables mechanical robustness and improved sodium-ion conductivity. *Energy Storage Mater.* **21**, 85–96 (2019).

97. Huang, J. *et al.* A Two-Electron Storage Nonaqueous Organic Redox Flow Battery. *Adv. Sustain. Syst.* **1700131**, 2–7 (2018).

98. Yu, J. *et al.* A class of liquid anode for rechargeable batteries with ultralong cycle life. *Nat. Commun.* **8**, 1–7 (2017).

99. Li, X., Zhang, H., Mai, Z., Zhang, H. & Vankelecom, I. Ion exchange membranes for vanadium redox flow battery applications. *Energy Environ. Sci.* **4**, 1147–1160

(2011).

100. Prifti, H., Parasuraman, A., Winardi, S., Lim, T. M. & Skyllas-kazacos, M. Membranes for Redox Flow Battery Applications. *Membranes (Basel).* **2**, 275–306 (2012).

101. Luo, T., Abdu, S. & Wessling, M. Selectivity of ion exchange membranes : A review. **555**, 429–454 (2018).

102. Xu, Z. *et al.* A zeolite ion exchange membrane for redox flow batteries. *Chem. Commun.* **50**, 2416–2419 (2014).

103. Teng, X. *et al.* Solution casting Nafion/polytetrafluoroethylene membrane for vanadium redox flow battery application. *Electrochim. Acta* **88**, 725–734 (2013).

104. Zhu, Y. G. *et al.* Dual redox catalysts for oxygen reduction and evolution reactions: Towards a redox flow Li-O2 battery. *Chem. Commun.* **51**, 9451–9454 (2015).

105. Colli, A. N., Peljo, P. & Girault, H. H. High energy density MnO4-/MnO42- redox couple for alkaline redox flow batteries. *Chem. Commun.* **52**, 14039–14042 (2016).

106. Yu, X. & Manthiram, A. Performance Enhancement and Mechanistic Studies of Room-Temperature Sodium-Sulfur Batteries with a Carbon-Coated Functional Nafion Separator and a Na2S/Activated Carbon Nanofiber Cathode. *Chem. Mater.* **28**, 896–905 (2016).

107. Hu, M. *et al.* Revealing the Critical Factor in Metal Sulfide Anode Performance in

Sodium-Ion Batteries: An Investigation of Polysulfide Shuttling Issues. *Small Methods* **4**, 1–8 (2020).

108. Bauer, I., Kohl, M., Althues, H. & Kaskel, S. Shuttle suppression in room temperature sodium-sulfur batteries using ion selective polymer membranes. *Chem. Commun.* **50**, 3208–3210 (2014).

VITA

Jameson Landon Tyler was born. He wrote a thesis. He graduated. He went on to move to San Diego and started a new a job at Infinity Power.